

AD-A073 224

VARIAN ASSOCIATES INC PALO ALTO CA
1.06-MICRON III-V PHOTOCATHODE DEVELOPMENT. (U)
MAY 79 J. S. FISCHER, P. E. GREGORY, S. B. HYDER

F/G 9/1

UNCLASSIFIED

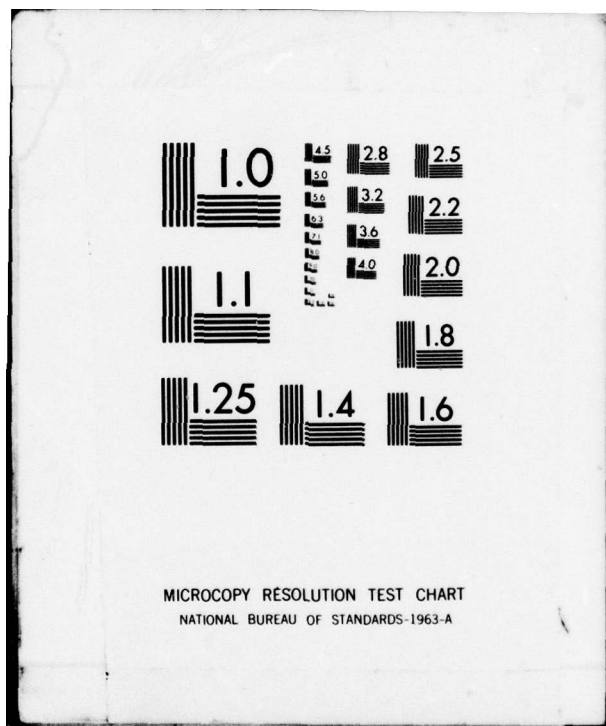
S B HYDER
AFAL-TR-79-1039

F33615-76-C-1351

NL

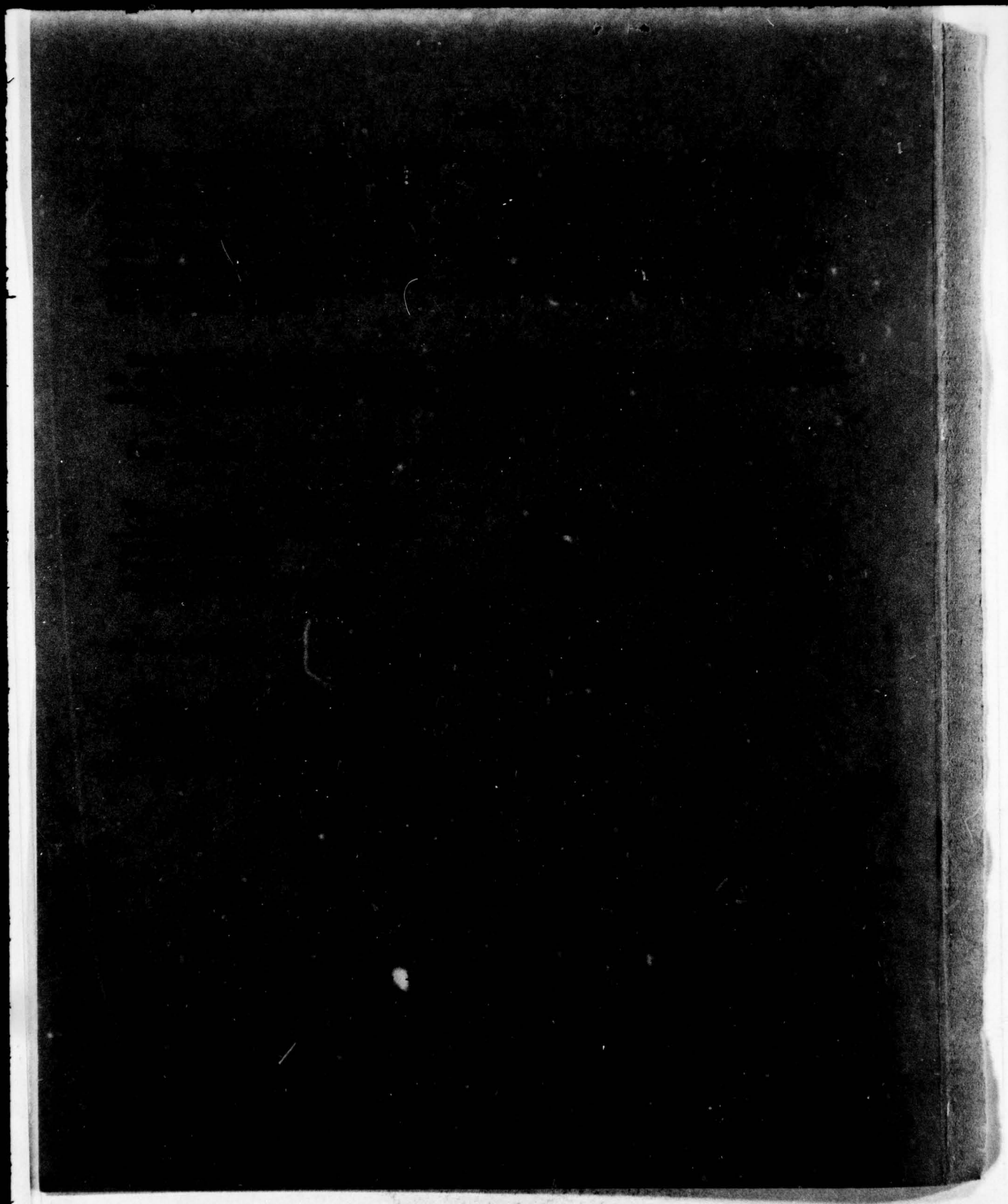
1 OF 2
AD
A073224





DA073224

REVERSED



Unclassified
SECURITY CLASSIFICATION OF THIS PAGE (When Data Entered)

19) REPORT DOCUMENTATION PAGE		READ INSTRUCTIONS BEFORE COMPLETING FORM
1. REPORT NUMBER AFAL-TR-79-1039	2. GOVT ACCESSION NO.	3. RECIPIENT'S CATALOG NUMBER -----
4. TITLE (and Subtitle) 1.06-MICRON III-V PHOTOCATHODE DEVELOPMENT	5. TYPE OF REPORT & PERIOD COVERED Technical Report (Final) (Nov 1976 - Nov 1978)	
7. AUTHOR(s) J. S. Escher, P. E. Gregory, S. B. Hyder R. R. Saxena, T. J. Maloney	6. CONTRACT OR GRANT NUMBER(s) F33615-76-C-1351	
9. PERFORMING ORGANIZATION NAME AND ADDRESS Varian Associates, Inc. 611 Hansen Way Palo Alto, CA 94303	10. PROGRAM ELEMENT, PROJECT, TASK AREA & WORK UNIT NUMBERS Project 2001 Task 200103 Work Unit 20010360	
11. CONTROLLING OFFICE NAME AND ADDRESS Air Force Avionics Laboratory (DHO) AF Wright Aeronautical Laboratories, AFSC Wright-Patterson AFB, Ohio 45433	12. REPORT DATE May 79	
14. MONITORING AGENCY NAME & ADDRESS (if different from Controlling Office) DCASMA San Francisco 1250 Bayhill Drive San Bruno, CA 94066	15. SECURITY CLASS. (of this report) Unclassified	
16. DISTRIBUTION STATEMENT (of this Report) Approved for public release; distribution unlimited. 16 2001 17 03		
17. DISTRIBUTION STATEMENT (of the abstract entered in Block 20, if different from Report) 9 Final rept. Nov 76-Nov 78,		
18. SUPPLEMENTARY NOTES		
19. KEY WORDS (Continue on reverse side if necessary and identify by block number) Transferred-electron photoemission 1.06-micron detector Heterojunctions Schottky barriers III-V Compounds		
20. ABSTRACT (Continue on reverse side if necessary and identify by block number) The design, fabrication, and evaluation of three transferred-electron (field assisted) photocathodes for high performance 1.06-micron detection are reported. The highest yields achieved at 1.06 microns were 2.7% from a InGaAsP direct emitter, 7.03% from an InP/InGaAs/InP hybrid heterojunction photocathode, and 1.05% for an all-VPE InGaP/InGaAs/GaAs heterojunction photocathode.		

DD FORM 1473 EDITION OF 1 NOV 65 IS OBSOLETE

Unclassified

SECURITY CLASSIFICATION OF THIS PAGE (When Data Entered)

364 100

79 08 28 044

PREFACE

The work reported here was supported by the Air Force Avionics Laboratory, Wright-Patterson Air Force Base, Ohio, under contract F33615-76-C-1351. The Monitoring Engineer is Mr. Donald J. Peacock. The program is aimed at the development of III-V high performance bias-assisted photocathodes for 1.06-micron detection.

The work was carried out in the Varian Corporate Research Solid State Laboratory. Contributions to this work were made by J. S. Escher, P. E. Gregory, S. B. Hyder, T. J. Maloney, and R. R. Saxena. The Program Manager is R. L. Bell.

ACCESSION for	
NTIS	White Section <input checked="" type="checkbox"/>
DDC	Buff Section <input type="checkbox"/>
UNANNOUNCED <input type="checkbox"/>	
JUSTIFICATION	
BY	
DISTRIBUTION/AVAILABILITY CODES	
Dist.	AVAIL. and/or SPECIAL
A	

TABLE OF CONTENTS

Section No.	Page No.
1. INTRODUCTION	1
2. THE TRANSFERRED-ELECTRON PHOTOCATHODE	6
2.1 Previous Work on the TE Cathode	6
2.2 Proposed TE Cathode Designs for High 1.06-Micron Detection	18
3. INVESTIGATION	31
3.1 LPE Growth of InGaAsP Direct Emitter TE Cathode	31
3.2 LPE-VPE Growth of the Hybrid Hetero- junction p-InP/p-InGaAsP Cathode	35
3.3 Growth of p-InGaP Emitter Cathodes	37
3.3.1 LPE Growth of InGaP	37
3.3.2 VPE Growth of the InGaP/InGaAs/GaAs Cathode	41
3.4 Model Calculations of the p-InGaP/p-InGaAs Heterojunction Cathode	72
3.4.1 Conduction Band Configuration	72
3.4.2 Monte Carlo Simulation of the InGaP Emitter	82
3.5 Direct Emitter Photoemission Results from p-InGaAsP	87
3.6 Hybrid Heterojunction Photoemission Results from p-InP/p-InGaAs	106
3.7 Photoemission Studies of InGaP/InGaAs/GaAs Cathodes	119
3.7.1 InGaP Emitter-Only Cathodes	119
3.7.2 Complete InGaP/InGaAs/GaAs Cathodes ..	124
4. CONCLUSIONS AND RECOMMENDATIONS	137
REFERENCES	139

LIST OF ILLUSTRATIONS

<u>Fig. No.</u>	<u>Page No.</u>
1. Energy band diagram of a p-InP TE emitter cathode	7
2. Reflection-mode quantum yield from the first successful p-InP TE cathode	10
3. Calculated bandgap and lattice constant for the InGaAsP quaternary system	12
4. Energy band diagram of the quaternary emitter TE photocathode under bias conditions	13
5. Approximate band edge energies, relative to the valence band maximum, vs composition for the InGaAsP alloy system lattice-matched to InP	14
6. Reflection-mode quantum yield from one of the first InGaAsP direct emitter TE cathodes	15
7. Heterojunction InP/InGaAsP TE photocathode energy band diagram	17
8. Experimental reflection-mode quantum yield from the first successful hybrid heterojunction photocathode	19
9. Experimental heterojunction transfer efficiency vs applied bias from a hybrid heterojunction cathode	20
10. Schematic energy band diagram for the InGaP/InGaAs/ GaAs heterojunction TE 1.06-micron photocathode ...	24
11. Bandgap (Γ) vs composition for InGaAs	25
12. Lattice constant vs composition for InGaAs	26
13. Lattice constant vs composition for InGaP	27
14. Approximate band edge energies vs composition for InGaP	28
15. Internal yield plot to determine Schottky barrier height of Ag/InGaP	30
16. Surface escape probability vs bandgap for GaAsP alloy NEA photocathodes	32
17. Photoluminescence spectra from a p-InGaAsP direct emitter cathode at 77°K	34

LIST OF ILLUSTRATIONS (Cont.)

18. Schematic diagram of the $\text{PCl}_3\text{-H}_2\text{-In}$ VPE system and approximate temperature profile	36
19. Spectrosil slider boat holder and plate used to cover the substrate prior to growth	38
20A. Surface micrograph of a 0.4-micron thick InGaP layer grown by LPE	40
20B. Surface micrograph of a 4.0-micron thick InGaP layer grown from the same melt as that used in Fig. 19a	40
21. Schematic diagram of the VPE InGaP-InGaAs system	44
22. Photograph of the VPE InGaP-InGaAs reactor system	45
23. Photograph of the VPE InGaP-InGaAs reactor system showing the growth tube and position of the slider boat	46
24. Photograph of the slider boat and cap with two substrate wafers in place	47
25. Photoluminescence spectrum from InGaP/InGaAs/GaAs sample #2-18 taken at 77°K.....	51
26. Photomicrograph of the surface of InGaP/InGaAs/GaAs sample #2-18, 212X	52
27. Photoluminescence spectrum from InGaP/GaAs sample #3-2 taken at 77°K	53
28. Ga(HCl) flow program used for InGaAs grading	56
29. Photomicrograph of the surface of InGaAs/GaAs sample #SRI-32, magnification 291X	57
30. Photoluminescence spectrum of InGaAs/GaAs sample #SR4-10	59
31. HCl(In) flow needed for growth of InGaP lattice-matched to an InGaAs layer of a given bandgap	60
32. Measured relationship between InGaP bandgap and InGaAs bandgap (both at 77°K) for InGaP/InGaAs/GaAs samples	62

LIST OF ILLUSTRATIONS (Cont.)

33	Photomicrograph of the surface of InGaP/InGaAs/GaAs sample #SR3-28, magnification 291X	64
34	Photomicrograph of the surface of InGaP/GaAs sample #SR3-12, magnification 291X	65
35	Photomicrograph of the surface of InGaP/InGaAs/GaAs sample #SR5-18, magnification 110X	66
36	Cleaved section of sample #SR2-12, magnification 1402X	67
37	Photoluminescence spectrum for InGaP/InGaAs/GaAs sample #SR2-9	68
38	InGaP p-type doping level vs Zn source temperature and versus Zn ionization energy determined from photoluminescence measurements	70
39	Auger sputter depth profile through a InGaP/InGaAs heterojunction	71
40	Calculated conduction band profile for an InGaP/InGaAs heterojunction TE cathode	76
41	Calculated conduction band profile for an InGaP/InGaAs heterojunction TE cathode	77
42	Calculated conduction band profile for an InGaP/InGaAs heterojunction TE cathode	78
43	Calculated conduction band profile for an InGaP/InGaAs heterojunction TE cathode	79
44	Calculated conduction band profile for an InGaP/InGaAs heterojunction TE cathode	80
45	Calculated conduction band profile for an InGaP/InGaAs heterojunction TE cathode	81
46	Average electron energy in conduction bands of InGaP emitter as a function of InGaP doping, as calculated from Monte Carlo Simulation	85
47	InGaP band spacings and profile assumed for the Monte Carlo simulation	86
48	Percent of electrons in each conduction band as a function of InGaP doping, calculated from the Monte Carlo simulation	88

LIST OF ILLUSTRATIONS (Cont.)

49	Reflection-mode quantum yield from a direct emitter p-InGaAsP/InP TE cathode	92
50	Reflection-mode quantum yield at 1.06 microns vs applied bias from a p-InGaAsP direct emitter cathode	93
51	Dark current emission vs applied bias from a p-InGaAsP direct emitter cathode at 300°K	94
52	Reflection-mode quantum yield at 1.06 microns and dark current density vs applied bias from a p-InGaAsP direct emitter	95
53	Transmission-mode quantum yield from a p-InGaAsP direct emitter cathode	97
54	Reflection-mode (R) and transmission-mode (T) yield at 1.06 microns vs applied bias from a p-InGaAsP direct emitter cathode	99
55	Reflection-mode quantum yield, Cs-only, from a p-InGaAsP direct emitter cathode	100
56	Reflection-mode quantum yield, Cs+0 activation, from a p-InGaAsP direct emitter cathode	101
57	Reflection-mode yield at 1.06 microns vs applied bias from a p-InGaAsP direct emitter cathode	102
58	Dark current emission from a direct emitter cathode at 300°K	103
59	Spatial photoemission scan at 1.06 microns across the face of a p-InGaAsP direct emitter cathode	104
60	Spatial photoemission scan across the face of a p-InP TE photocathode	105
61	Reflection mode quantum yield from InP/InGaAs hybrid cathode #8-17	107
62	Reflection-mode quantum yield at 1.06 microns, and emitted dark current, as a function of bias for InP/InGaAs hybrid cathode #8-17	109

LIST OF ILLUSTRATIONS (Cont'd.)

63 Depletion layer width, W , vs applied reverse bias, V_{bias} , for a Ag-InP Schottky-barrier contact at various acceptor doping concentrations, N_A 110

64 Reflection-mode quantum yield from a p-InP/p-InGaAsP hybrid heterojunction TE cathode 111

65 Cleaved section of a hybrid heterojunction cathode #2218 112

66 Reflection-mode yield at 1.40 and 1.17 eV photon energy vs applied bias from a hybrid heterojunction cathode 114

67 Heterojunction transfer efficiency vs applied bias from a hybrid heterojunction cathode 115

68 Dark current emission vs applied bias from a hybrid heterojunction cathode at 300°K 116

69 Auger spectrum from the surface of an Ag/InP cathode showing In on the Ag film surface 117

70 Auger depth profile through a Ag/InP interface 118

71 In/Ag Auger peak height ratio vs photoelectric threshold for 3000, 1000, and 160 Å Ag films on InP 120

72 Fowler photoemission plot for Cs-only and Cs+O activations on a hybrid heterojunction cathode (Ag/InP surface) 121

73 Reflection-mode quantum yield from a p-InGaP/GaAs cathode for Cs+O activation 123

74 Reflection-mode quantum yield from a p-InGaP/InGaAs/GaAs direct emitter cathode for Cs+O activation 125

75 Reflection-mode yield for InGaP/InGaAs/GaAs cathode #6-9B, Cs+O activation 126

76 Reflection-mode yield for InGaP/InGaAs/GaAs cathode #SR3-13, Cs+O activation 128

77 Reflection-mode yield at $h\nu$ = 1.8 and 1.17 eV as a function of bias for InGaP/InGaAs/GaAs cathode #SR3-13 129

LIST OF ILLUSTRATIONS (Cont.)

78	Reflection-mode yield for InGaP/InGaAs/GaAs cathode #SR3-28, measured with a 20X70 mil ² light spot, Cs+O activation	131
79	Reflection-mode yield for InGaP/InGaAs/GaAs cathode #SR3-28, measured with a 12 -mil diameter light spot	132
80	Reflection-mode yield at $h\nu = 1.8$ and 1.17 eV as a function of bias for InGaP/InGaAs/GaAs cathode #SR3-28	133
81	Reflection-mode yield for InGaP/InGaAs/GaAs cathode #SR6-15	135
82	Reflection-mode yield for InGaP/InGaAs/GaAs cathode #SR4-24, Cs+O activation	136

SUMMARY

It is the general purpose of this work to significantly improve the state-of-the-art in 1.06-micron photocathode devices for use in active laser communications and imaging systems. The overall goal of the program is to develop a high sensitivity III-V semiconductor 1.06-micron photocathode utilizing field-assisted, transferred-electron (TE) photoemission. The cathode structure should be capable of 20% quantum efficiency, large active area, and sealed-off tube operation.

The most sensitive 1.06-micron photocathodes available today are the negative electron affinity (NEA) III-V semiconductor cathodes. Yields of 0.5 to 3.0% at 1.06 microns are commercially available in a photomultiplier tube from Varian Associates, Inc. Achieving a high quantum efficiency from a single-crystal III-V photoemitter is largely a question of electron surface escape probability since the processes of photon absorption and electron diffusion to the surface can be quite efficient. Work function and surface barrier effects at the vacuum-semiconductor interface limit the successful transport of photoexcited electrons into vacuum. In order to overcome the surface barrier effects, various externally-biased cathodes have been studied over the years. A number of p-n junction, MOS, field-emission, and heterojunction bias-assisted photocathodes have been proposed and experimentally studied but none has shown reasonably efficient photoemission combined with low dark current emission to be of practical interest.

In 1974 however, Bell, James, and Moon of this laboratory demonstrated a bias-assisted p-InP cathode using for the first time the mechanism of TE photoemission. TE

photoemission is based on the fact that for certain III-V semiconductors such as InP, InGaAsP alloys, and GaAs, electrons can be promoted to the upper conduction band valleys with reasonable efficiency by applying modest electric fields. Photogenerated electrons which successfully transfer to the upper valleys have a good probability of being emitted over the work function and surface energy barriers into vacuum. Encouraged by this initial result, work at Varian on TE photocathodes has progressed steadily over the past four years with a major emphasis being made on both 1-2 micron passive night vision detectors and this work on high performance 1.06-micron detectors.

Three TE photocathode designs were studied for high efficiency 1.06-micron detection. The first of these is a p-InGaAsP direct emitter cathode in which the processes of photogeneration and electron emission are confined (as in a NEA cathode) to a single active layer. This is the simplest of designs and from a materials standpoint the most straightforward and highly developed. Vacuum photoemission experiments from direct emitter cathodes have demonstrated 1.06-micron yields up to 2.7% under full bias conditions. This represents a factor of 10 to 20 improvement over a conventional S-1 cathode and is comparable to a good NEA cathode. The second approach is that of a hybrid p-InP/ p-InGaAsP TE heterojunction cathode. The heterojunction cathode separates the functions of photoelectron generation (p-InGaAsP) and electron emission (p-InP) into distinct layers. In principle, the heterojunction approach should achieve a higher efficiency device since each function can in principle be separately optimized. 7.3% reflection-mode yield at 1.06 microns was achieved from a hybrid heterojunction cathode.

The third cathode design, which offers the highest potential 1.06-micron sensitivity, is a p-InGaP/p-InGaAs

heterojunction TE cathode. The electron emitting layer (p-InGaP) has a higher bandgap than that of p-InP, 1.7 eV vs 1.35 eV. Therefore it is anticipated (based on experimental NEA work) that the surface escape probability from a p-InGaP emitter would be superior to that of p-InP, and hence offer improved performance over that of either the p-InGaAsP direct emitter cathode or the p-InP/ p-InGaAsP heterojunction cathode. An all vapor phase epitaxy system was built to grow the InGaP/InGaAs/GaAs cathode. Details of the InGaP/InGaAs growth are discussed, as well as photoemission results from this cathode. 1.05% reflection-mode yield at 1.06 microns was achieved from an InGaP/InGaAs/GaAs cathode.

Excellent progress was achieved during the course of this contract towards reaching the program goals. A moderate amount of additional effort on the InP/InGaAs/InP hybrid cathode in the areas of InP optimization and continued improvement of vacuum processing should permit 10% yield at 1.06 microns to be achieved.

Development of the InGaP/InGaAs/GaAs cathode to its full potential would require more materials development, especially in achieving better control over the InGaP growth. Better reproducibility of InGaP parameters from run to run is needed to optimize the InGaP/InGaAs/GaAs cathode.

1. INTRODUCTION

It is the general purpose of this work to significantly improve the state-of-the-art in 1.06-micron photoemission devices for use in active laser imaging and communications systems. The overall goal of the program is to develop high sensitivity III-V semiconductor 1.06-micron photocathodes utilizing field-assisted, TE photoemission. The cathode structure should be capable of 20% quantum efficiency, large active area, and sealed-off tube operation.

In order to put the present field-assisted photocathode program in better perspective, it is worthwhile to briefly review some of the prior field-assisted work. Previous field-assisted photocathode work will be reviewed in this section; the following section discusses the three photocathode designs, based on the TE effect, which form the basis of the work described in this report.

As is well known, work function and surface barrier effects at the interface with the activating layer¹ make it necessary to consider biasing photocathodes in order to achieve useful photoemission beyond about 1.1-micron wavelength. In order to overcome the surface barrier effects, various externally-biased cathodes have been studied over the past 18 years beginning with the work of Simon and Spicer at RCA.^{2,3} Historically, the bulk of the field-assisted photocathode work up to 1968 had been on reverse-biased p-n junction devices activated with Cs or Cs and oxygen to reduce the work function at the surface. The external quantum efficiencies achieved into vacuum however were limited to $<10^{-4}$ (electrons/incident photon) in all cases.⁴⁻⁶ With the advent of the negative electron affinity (NEA) cathode development in the late 1960's,⁷ there was relatively little work done on externally-biased cathodes.

However it soon became clear that the limit to high yield (>0.10% quantum efficiency) NEA photoemission was around 1.1 micron.

Several field-assisted projects were initiated under ARPA support in the early 1970's aimed at the 1-2 micron range. A passive night vision device taking advantage of the strong air-glow radiation beyond 1 micron is the primary application of the 1-2 micron program, although other applications would certainly emerge if such a device could be demonstrated. Some of these approaches involved the reverse-biased p-n junction for either area or edge emission utilizing the improved device and vacuum technology of the day. Groups at RCA⁸ and UCLA⁹ pursued this approach most recently. Difficulties with junction breakdown during vacuum heat cleaning and fabrication of ultrathin plane parallel junctions were the most serious problems. Approximately 10^{-4} quantum efficiency at 1.06 microns into vacuum was achieved at UCLA from a silicon device. Another approach has been the reverse-biased Schottky-barrier device based on the work of White and Logan.¹⁰ A thin metal film is evaporated onto a p-type semiconductor and reverse-biased. Experimental yields from these devices have been limited to less than 10^{-4} quantum efficiency.¹¹⁻¹³ A slight modification of the Schottky-barrier approach is an MOS structure reported by Foss at CBS Laboratories.¹⁴ 10^{-3} quantum efficiency at 1.06 microns was achieved into vacuum from an Al-SiO₂-Si device activated with Cs and oxygen. However, the dark current from the MOS device under bias conditions was on the order of 10^{-5} A/cm²-- much too high for practical applications.

A similar approach to the MOS cathode is the tunnel emitter. This work, first carried out at the University of Minnesota, then at RCA Laboratories, and more recently at the Night Vision Laboratory, Ft. Belvoir, VA, is based on an

ultrathin insulator sandwiched between either two semiconductors or a semiconductor and a thin metal film. Al_2O_3 grown by chemical vapor deposition was the major insulator studied. Field-assisted photoemission has been achieved from a Si- Al_2O_3 -Ag structure activated with Cs and oxygen. High dark current and poor frequency response seem to be the major difficulties with the Si tunnel emitter device. Similar structures fabricated from Ge have not shown photoemission into vacuum.

An entirely new approach to a field-assisted cathode was brought forward in the early 1970's by various groups employing the idea of a double heterojunction structure. The complete cathode consists of a low bandgap photon absorbing layer followed by a high bandgap hole barrier, necessary for external biasing, and an electron emitting layer capable of high efficiency NEA photoemission (e.g. GaAs). Ideally, under reverse-bias conditions, the conduction bands of the device should allow thermalized photo-excited electrons to diffuse and/or drift efficiently from the photon absorbing layer across the hole barrier layer into the electron emitting layer and finally into vacuum. Groups at Carnegie-Mellon University¹⁵ and Rockwell International¹⁶ have pursued this approach most recently. No vacuum photoemission results have come forward to date however. The Carnegie-Mellon cathode was a Ge-Zn-Se-GaAs:Cs-O device. Satisfactory fabrication of the complete structure was not achieved. Efficient electron transfer from the Ge into the ZnSe Hole barrier could not be demonstrated. The cathode structure most extensively investigated by the Rockwell group for 1.06 microns was a GaAsSb-GaAlAs-GaAs structure grown on GaAs. This liquid phase epitaxial grown structure is not a completely lattice-matched system. The composition of the GaAlAs hole barrier was such that the entire lattice mismatch was accommodated at the GaAsSb-GaAlAs interface. Although no vacuum photoemission results have

been obtained, on-the-bench internal photoemission results indicate poor electron transport across the GaAsSb-GaAlAs interface. It would also be expected that junction deterioration problems might be encountered with this or similar devices during the vacuum heat cleaning procedure commonly used to clean the semiconductor-vacuum surface.

Another interesting field-assisted cathode approach is the field emission photocathode based on earlier work on single field point emitters. Arrays of Si-based field emitters have been successfully fabricated by groups at Westinghouse Research Laboratories¹⁷ and at SRI.¹⁸ 7.5% quantum efficiency into vacuum has been achieved at 300°K. The major problems are a room temperature dark current on the order of 10^{-6} A/cm² under bias conditions and a limited MTF. Arrays of Ge-based field emitters, for > 1 micron response, have not been successfully fabricated to date.

The work at Hughes on thin Ag films on Si¹⁹ is particularly relevant to the present program. The initial idea of their "Studies of Silver Interlayer Photocathodes at 1.06 Microns" was to demonstrate improved 1.06-micron semitransparent yield from a thinned Si:Cs-O photocathode through the introduction of a thin Ag interlayer at the Si:Cs-O interface. An enhancement in 1.06-micron semitransparent quantum efficiency of approximately 50% would arise simply from the increased optical reflection of near bandgap radiation back into the Si. Furthermore, it was felt that since the work function of Cs-O activated Ag could be processed to <1.0 eV²⁰ and that electron losses through a thin Ag film should not be a serious loss for low energy electrons²¹ the transport of photogenerated electrons into vacuum should be good. The feeling was that the work function on the Ag film could be made lower than the interface Cs-O barrier height (~ 1.1 to 1.2 eV) found on semiconductor:Cs-O interfaces.²² In principle the device could

operate with an applied reverse bias to the Ag film to give an additional "effective" negative electron affinity between the conduction band in the bulk and the vacuum potential. In practice, the Si:Ag:Cs-O yields were low. Sputter-Auger depth chemical profiling and Rutherford back-scattering of 280 keV He^{++} analysis indicated a significant region of mixed semiconductor-metal. The depth of the intermixing was difficult to measure directly since it was felt that the thinnest films (100-200 Å) may well have microscopic thickness variations on the same order as the film thickness. SEM micrographs at 120,000x supported the thickness variation or surface roughness contention. The net effect of the intermixing was to reduce the surface escape probability either through (1) Ag acting as a compensating impurity leading to a relatively deep bandbending region or (2) increased photo-electron scattering in the mixed region. A final experimental observation made by the Hughes group was that the photo-electric threshold on Si:Ag:Cs-O surfaces was found to be thickness-dependent for films less than about 300 Å thick. The thinnest Ag films were found to have a photoelectric threshold 0.10 to 0.15 eV higher than the thickest films.

Several conclusions can be drawn from the above brief history of field-assisted photocathode work (which has excluded recent work here at Varian). First, significant difficulties have been encountered with junction deterioration during vacuum heat-cleaning procedures. Junctions which are exposed should be passivated such that they can be cycled to around 600°C in vacuum. Second, all heterojunctions that photoexcited electrons cross must be nearly "ideal" heterojunctions--i.e. low recombination interfaces. In practice this means the heterojunction pair must be very closely lattice-matched. The GaAs-GaAlAs combination is the most well-known pair but InGaAsP alloys lattice-matched to

InP are another example. Third, another major difficulty with reverse-biased p-n junction devices, apart from junction breakdown, is the fact that part of the transport is by hot electron transport across an ultrathin n-type region. Efficient electron transfer across such a region (without going to avalanching) is extremely difficult because of the short mean-free path for hot electrons. Internal p-n junctions therefore should not be considered as strong candidates for high efficiency field-assisted cathodes. Finally, the ability to fabricate reasonable large-area devices with good MTF and operate with stability at or near room temperature must be considered.

2. THE TRANSFERRED-ELECTRON PHOTOCATHODE

2.1 Previous Work on the TE Cathode

The work at Varian on field-assisted devices began in 1974 with the successful demonstration of TE photoemission from p-type InP.²³ Figure 1 shows an energy band diagram for bias and no bias conditions for a p-InP TE cathode. Since the active (photon absorbing and electron generating) layer should contain few free electrons in the absence of illumination, it should be a p-type semiconductor. In order to apply a bias voltage, a "hole barrier" is needed. A simple metal/semiconductor Schottky barrier is used. The Schottky barrier to hole flow for metallic contacts on p-InP (~ 0.75 eV) is sufficiently high for a value of hole current low enough to be easily sustained by the biasing circuit. A ≈ 150 Å thick Ag film is evaporated, *in situ*, for this Schottky contact. Transmission of energetic electrons through a thin Ag film can be reasonably efficient. Hot electrons in transit lose energy to phonons, impurities, and electron-electron collisions. In addition, they suffer phonon back-scattering (in our case from the Cs-O layer) and quantum mechanical reflections at the layer interfaces. These

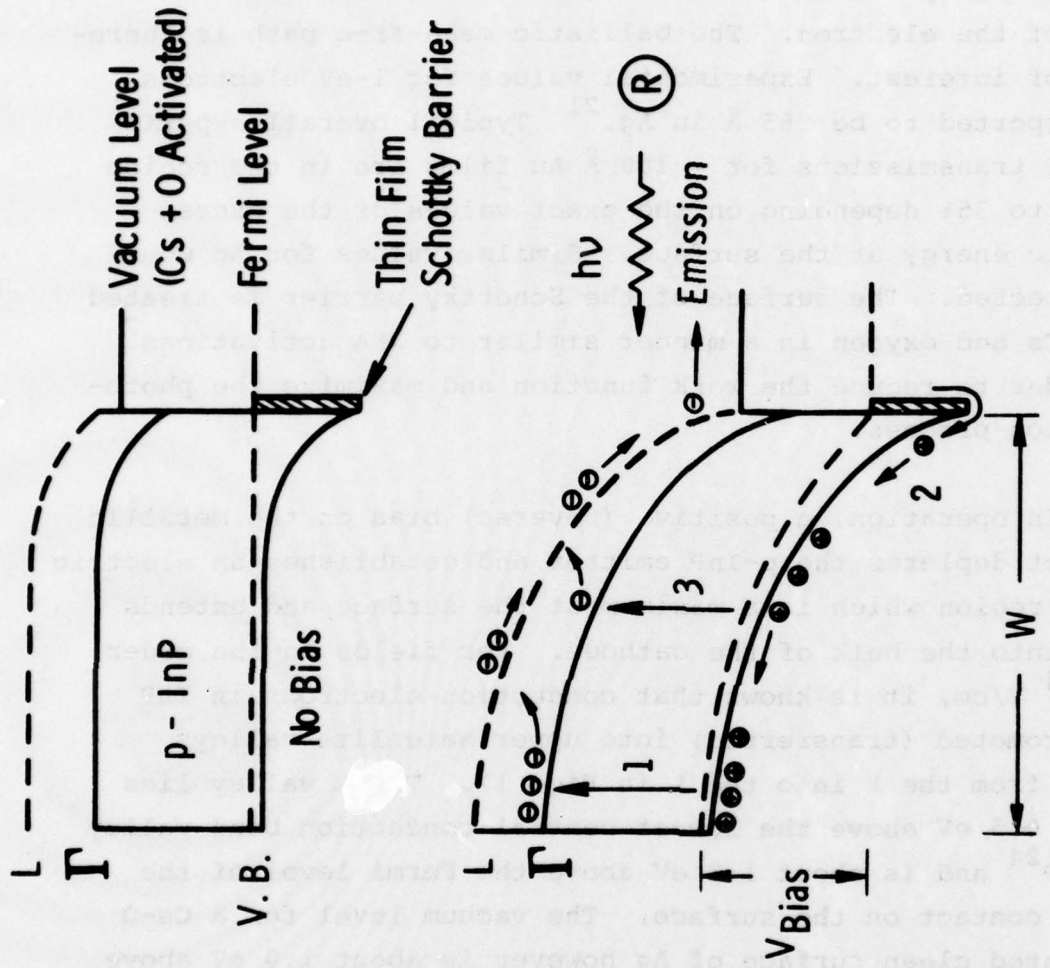


Fig. 1. Energy band diagram of a p-InP TE emitter cathode.

losses can be substantial unless the electrons arrive at the surface with more than 0.1 eV excess energy. A single scattering by any of the mechanisms listed can result in loss of the electron. The ballistic mean-free path is therefore of interest. Experimental values for 1-eV electrons are reported to be 265 Å in Ag.²¹ Typical overall experimental transmissions for ~ 100 Å Au films are in the region of 15 to 35% depending on the exact values of the excess kinetic energy at the surface. Similar values for Ag would be expected. The surface of the Schottky barrier is treated with Cs and oxygen in a manner similar to NEA activations⁷ in order to reduce the work function and maximize the photoemission process.

In operation, a positive (reverse) bias on the metallic contact depletes the p-InP emitter and establishes an electric field region which is a maximum at the surface and extends back into the bulk of the cathode. For fields on the order of 10^4 V/cm, it is known that conduction electrons in InP are promoted (transferred) into upper satellite valleys (e.g. from the Γ into the L in Fig. 1). The L valley lies about 0.5 eV above the lowest central conduction band valley in InP²⁴ and is about 1.5 eV above the Fermi level of the metal contact on the surface. The vacuum level for a Cs-O activated clean surface of Ag however is about 1.0 eV above the Fermi level of the metal.²⁰ Therefore there is an effective NEA condition created at the emitting surface with respect to the upper satellite valleys of Cs-O activated Ag/p-InP under bias conditions. Since promotion to the upper valleys in InP is known from microwave and photoemission work to be an efficient process for fields greater than 10^4 V/cm, this configuration makes for efficient transfer of photogenerated electrons in the Γ valley to the upper valleys where they can be emitted over the surface vacuum barrier (process "1" in Fig. 1).

The first experimental demonstration of TE photoemission is shown in Fig. 2. The yield is for photons incident on the emitting surface (i.e. reflection-mode yield). The no-bias yield is primarily from photoexcited electrons generated in the Cs-O coated Ag Schottky-barrier metal. A Fowler plot (i.e. yield^{1/2} vs photon energy)²⁵ would indicate a work function of about 1.0 eV from the data in Fig. 2. The p-InP cathode is relatively low p-type, $\sim 10^{15}/\text{cm}^3$. Therefore even though the p-InP surface is clean and has Cs+O on it, the photoemission from the p-InP surface itself is quite low. If the p-InP had been doped to $10^{17}/\text{cm}^3$ or higher, then the zero bias yield from the p-InP surface would be much higher than that from the activated Ag surface. For $10^{18}/\text{cm}^3$ or higher doping p-InP becomes an NEA cathode.²⁶ The reason for the significant difference in photoemission (at zero bias) for p⁻-InP vs p⁺-InP is the difference in depth of the surface space charge region. For effective NEA photoemission, high p-type doping is necessary in order to minimize the space charge distance (i.e. the band-bending distance W in Fig. 1). The thermalized electrons (electrons in the Γ valley) which diffuse toward the surface in an NEA cathode quickly pass through the space charge region (which is only on the order of 100 Å wide) through the Cs-O activation layer and then into vacuum.²² As the doping is decreased, the space charge region becomes longer and longer and most of the thermalized Γ electrons slide downhill and recombine at the emitting surface. Under bias conditions however, initially thermalized electrons which diffuse or drift toward the emitting surface can be transferred into the L valley (and/or heat up in the Γ valley), be transported to the surface, and be emitted into vacuum. Since the photo-generation of electrons is determined by the optical absorption of InP, the threshold for NEA or TE photoemission is essentially the bandgap of InP, 1.35 eV at 300°K. As can be seen in Fig. 2, the field-assisted yield is over four orders of magnitude higher, near threshold, than the no-bias yield.

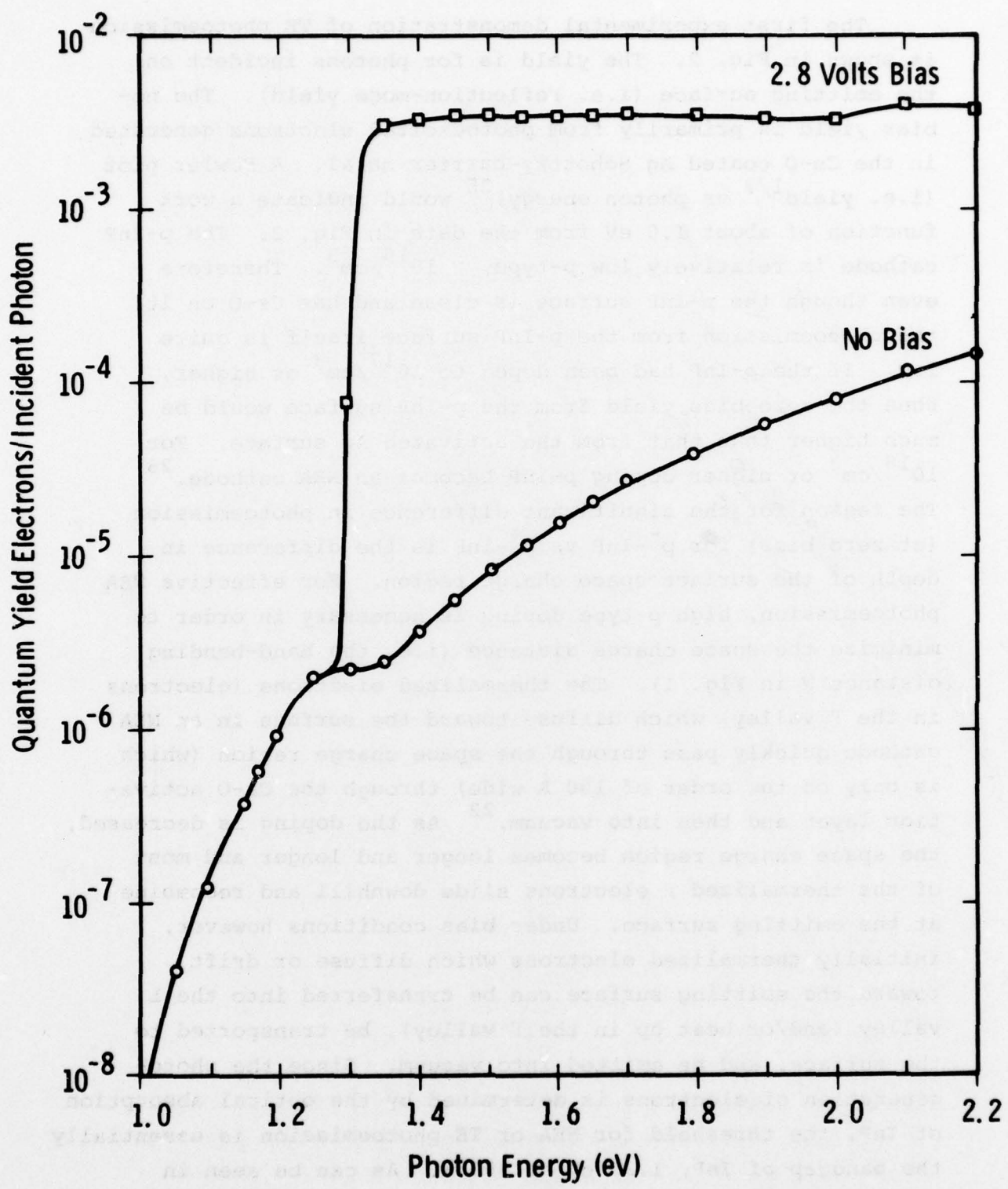


Fig. 2. Reflection-mode quantum yield from the first successful p-InP TE cathode.

The 0.5% quantum efficiency measured from this first cathode has been improved since then to a peak 11.9% quantum efficiency in the reflection mode, at 1.4-eV photon energy, with 20V bias, and 300°K operation from a bulk-grown $2 \times 10^{15}/\text{cm}^3$ p-InP cathode. Typical TE yield from p-InP however is 1 to 3% quantum efficiency at 3-5 V bias. Additional improvement in TE yield should come with refinements in growth, processing, handling, Schottky-barrier fabrication, and activation of the cathode.

The next significant development in TE cathode technology was the demonstration of TE photoemission from the III-V InGaAsP quaternary alloys LPE-grown lattice-matched to InP substrates. Development of the InGaAsP alloys for NEA 1.06-micron cathodes began in early 1972.²⁷ The InGaAsP quaternary system with the InP lattice constant can generate bandgaps spanning the region from 1.35 eV (InP) to 0.75 eV (InGaAs)-- see Fig. 3. References 28 and 29 provide the most recent materials developments and additional references on earlier work.

TE photoemission from p-InGaAsP was first experimentally demonstrated in late 1974. An energy band diagram for this case is shown in Fig. 4. The physics of emission is the same as that for a p-InP emitter, however the Γ to L separation is larger making transfer more difficult than in InP and the L band edge at the surface is closer to the vacuum level, which results in a lower overall surface escape probability (see Fig. 5). For these reasons, one would expect the yield from the lower bandgap p-InGaAsP emitter cathodes to be less than that from InP. Experimental TE photoemission yields from p-InGaAsP emitters have, on the average, been lower than from p-InP. Figure 6 shows TE yield from one of the first p-InGaAsP emitter cathodes, which had a 1.04-eV bandgap at 300°K. The 1.06-micron reflection-mode yield from

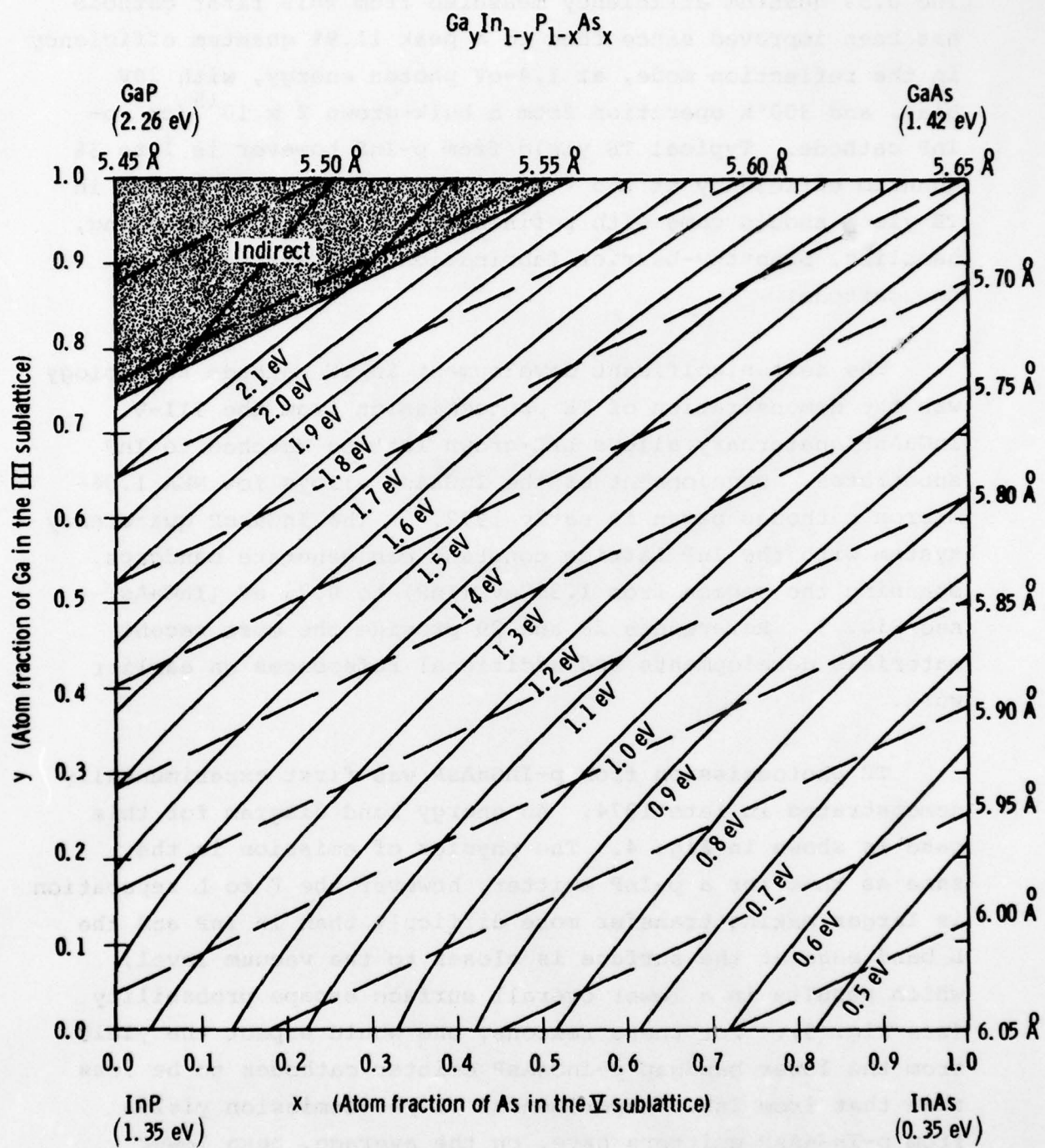


Fig. 3. Calculated bandgap and lattice constant for the InGaAsP quaternary system.

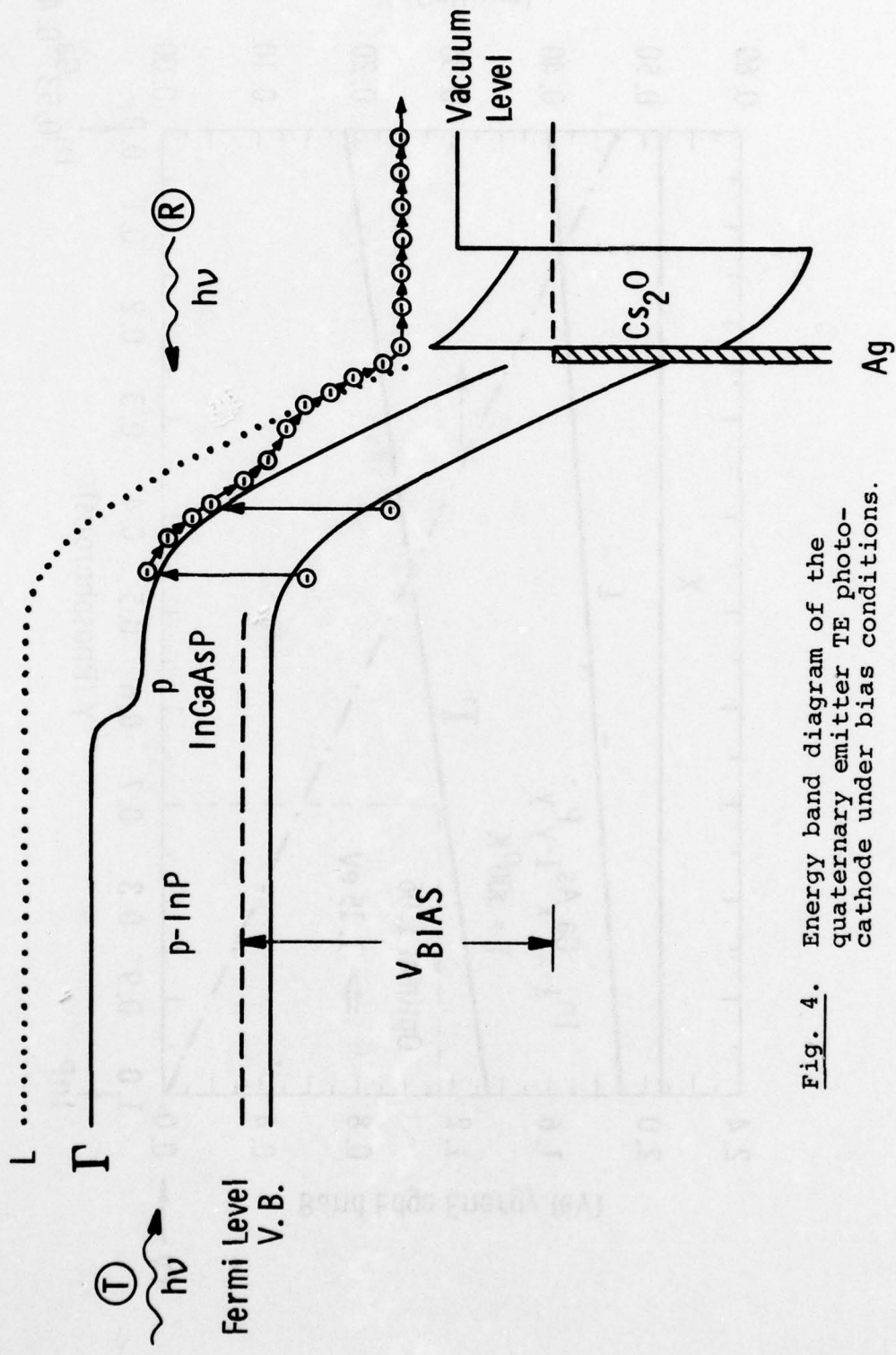


Fig. 4. Energy band diagram of the quaternary emitter TE photocathode under bias conditions.

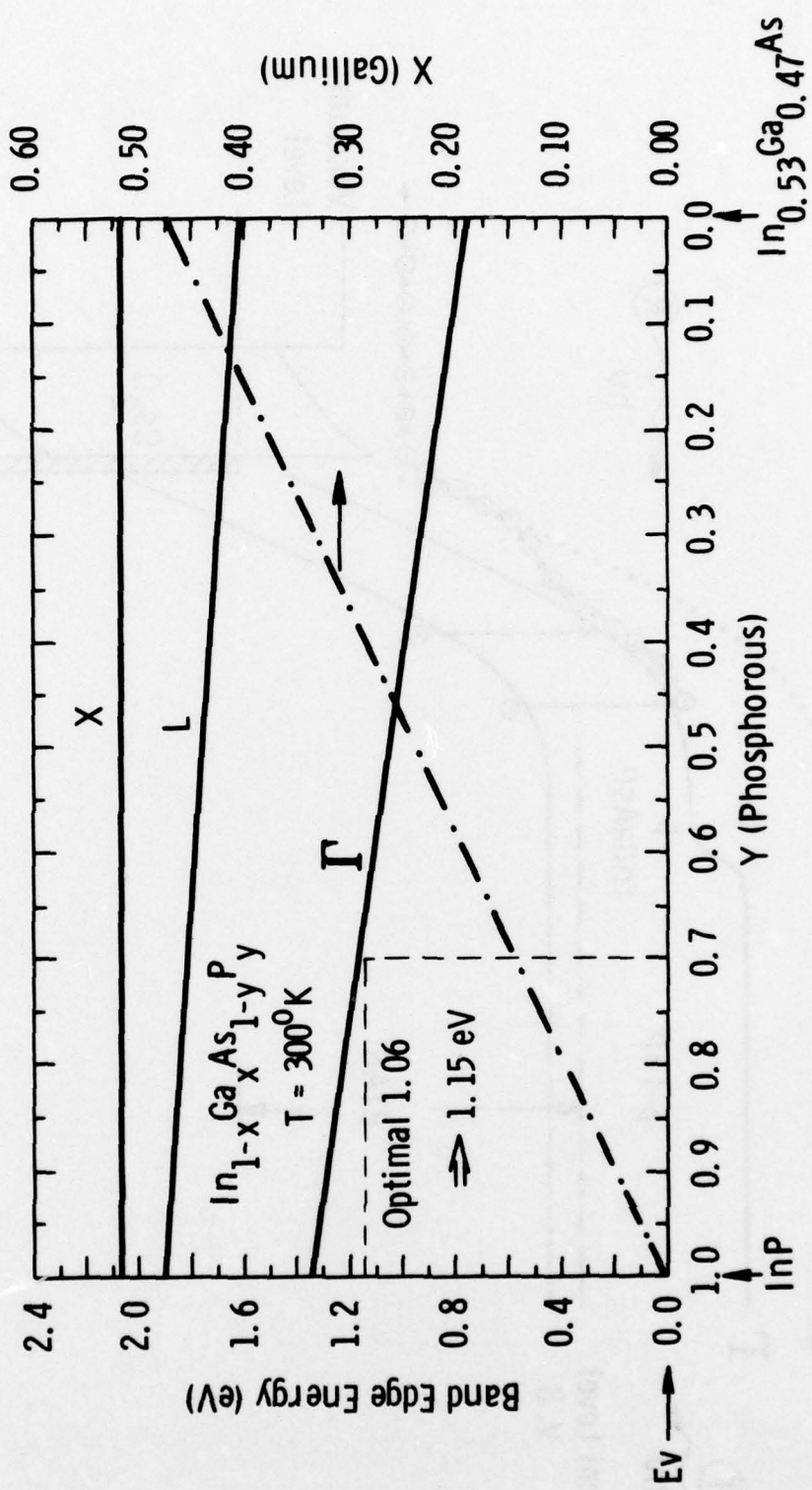


Fig. 5. Approximate band edge energies, relative to the valence band maximum, vs composition for the InGaAsP alloy system lattice-matched to InP.

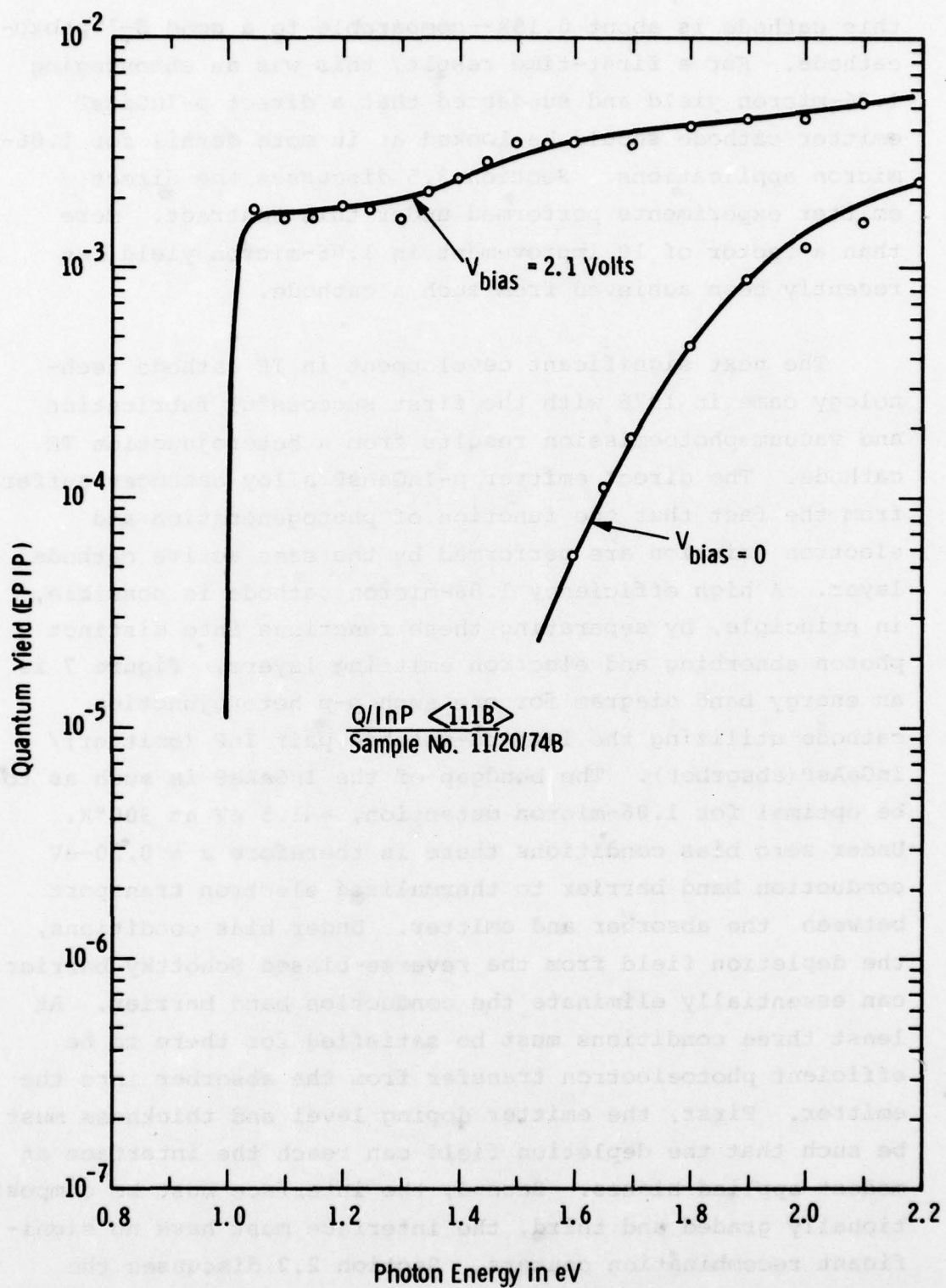


Fig. 6. Reflection-mode quantum yield from one of the first InGaAsP direct emitter TE cathodes.

this cathode is about 0.15%--comparable to a good S-1 photocathode. For a first-time result, this was an encouraging 1.06-micron yield and suggested that a direct p-InGaAsP emitter cathode should be looked at in more detail for 1.06-micron applications. Section 3.5 discusses the direct emitter experiments performed under this contract. More than a factor of 10 improvement in 1.06-micron yield has recently been achieved from such a cathode.

The next significant development in TE cathode technology came in 1975 with the first successful fabrication and vacuum photoemission results from a heterojunction TE cathode. The direct emitter p-InGaAsP alloy cathodes suffer from the fact that the function of photogeneration and electron emission are performed by the same active cathode layer. A high efficiency 1.06-micron cathode is possible, in principle, by separating these functions into distinct photon absorbing and electron emitting layers. Figure 7 is an energy band diagram for one such p-p heterojunction cathode utilizing the lattice-matched pair InP (emitter)/InGaAsP (absorber). The bandgap of the InGaAsP is such as to be optimal for 1.06-micron detection, \approx 1.5 eV at 300°K. Under zero bias conditions there is therefore a \approx 0.20-eV conduction band barrier to thermalized electron transport between the absorber and emitter. Under bias conditions, the depletion field from the reverse-biased Schottky barrier can essentially eliminate the conduction band barrier. At least three conditions must be satisfied for there to be efficient photoelectron transfer from the absorber into the emitter. First, the emitter doping level and thickness must be such that the depletion field can reach the interface at modest applied biases. Second, the interface must be compositionally graded and third, the interface must have no significant recombination centers. Section 2.2 discusses the first two points in some detail.

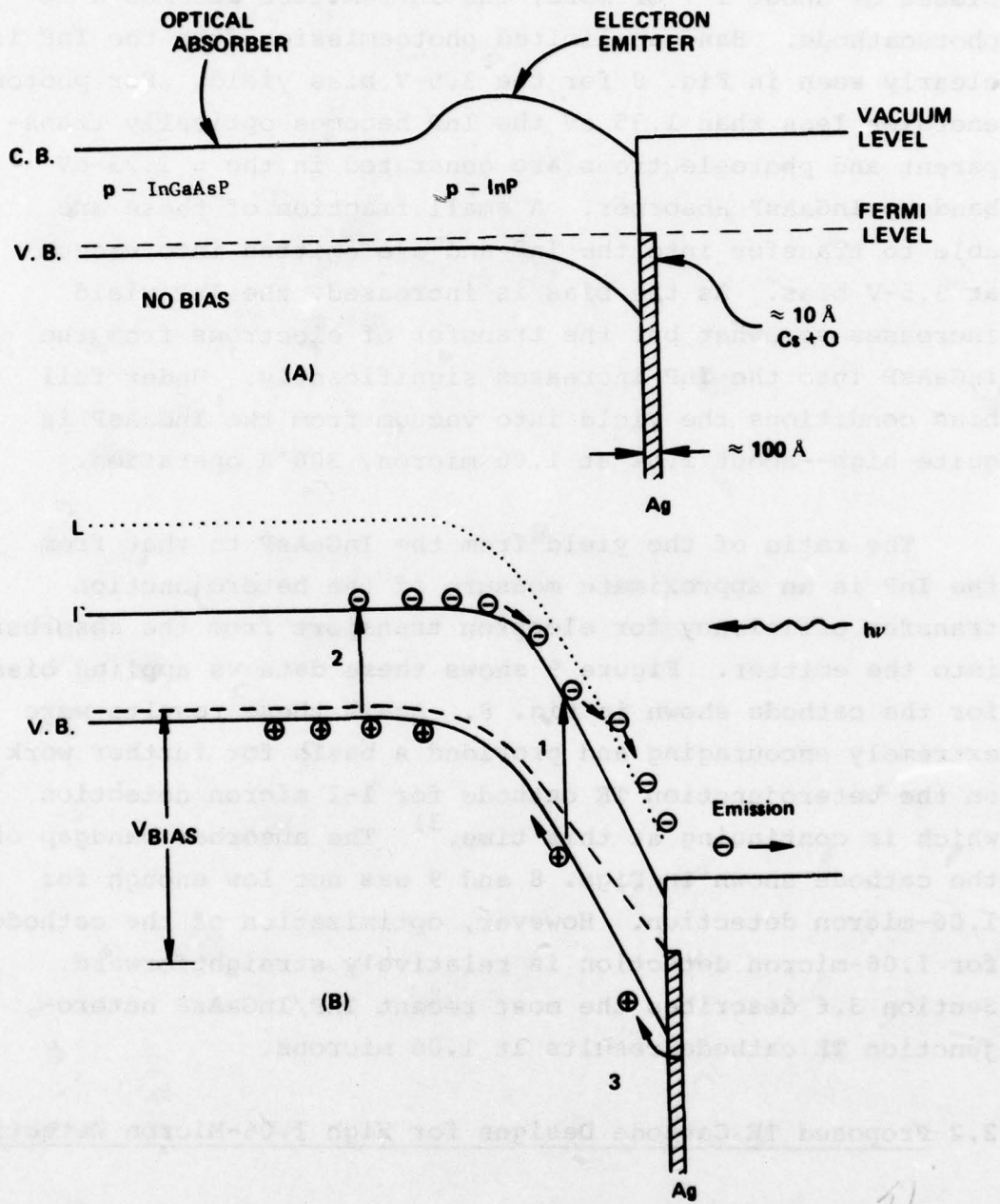


Fig. 7. Heterojunction InP/InGaAsP TE photocathode energy band diagram.

Figure 8 shows the first experimental demonstration of a heterojunction TE cathode.³⁰ The zero bias yield is again primarily from the Cs-O activated Ag/InP surface. For biases of about 1 V or more, the InP emitter becomes a TE photocathode. Bandgap-limited photoemission from the InP is clearly seen in Fig. 8 for the 3.5-V bias yield. For photon energies less than 1.35 eV the InP becomes optically transparent and photoelectrons are generated in the \approx 1.23-eV bandgap InGaAsP absorber. A small fraction of these are able to transfer into the InP and are emitted into vacuum at 3.5-V bias. As the bias is increased, the InP yield increases somewhat but the transfer of electrons from the InGaAsP into the InP increases significantly. Under full bias conditions the yield into vacuum from the InGaAsP is quite high--about 2.0% at 1.00 micron, 300°K operation.

The ratio of the yield from the InGaAsP to that from the InP is an approximate measure of the heterojunction transfer efficiency for electron transport from the absorber into the emitter. Figure 9 shows these data vs applied bias for the cathode shown in Fig. 8. Again these results were extremely encouraging and provided a basis for further work on the heterojunction TE cathode for 1-2 micron detection which is continuing at this time.³¹ The absorber bandgap of the cathode shown in Figs. 8 and 9 was not low enough for 1.06-micron detection. However, optimization of the cathode for 1.06-micron detection is relatively straightforward. Section 3.6 describes the most recent InP/InGaAsP heterojunction TE cathode results at 1.06 microns.

2.2 Proposed TE Cathode Designs for High 1.06-Micron Detection

Three TE cathode designs which are viable candidates for achieving the program goals were investigated under this contract. All three cathodes have demonstrated 1.06-micron

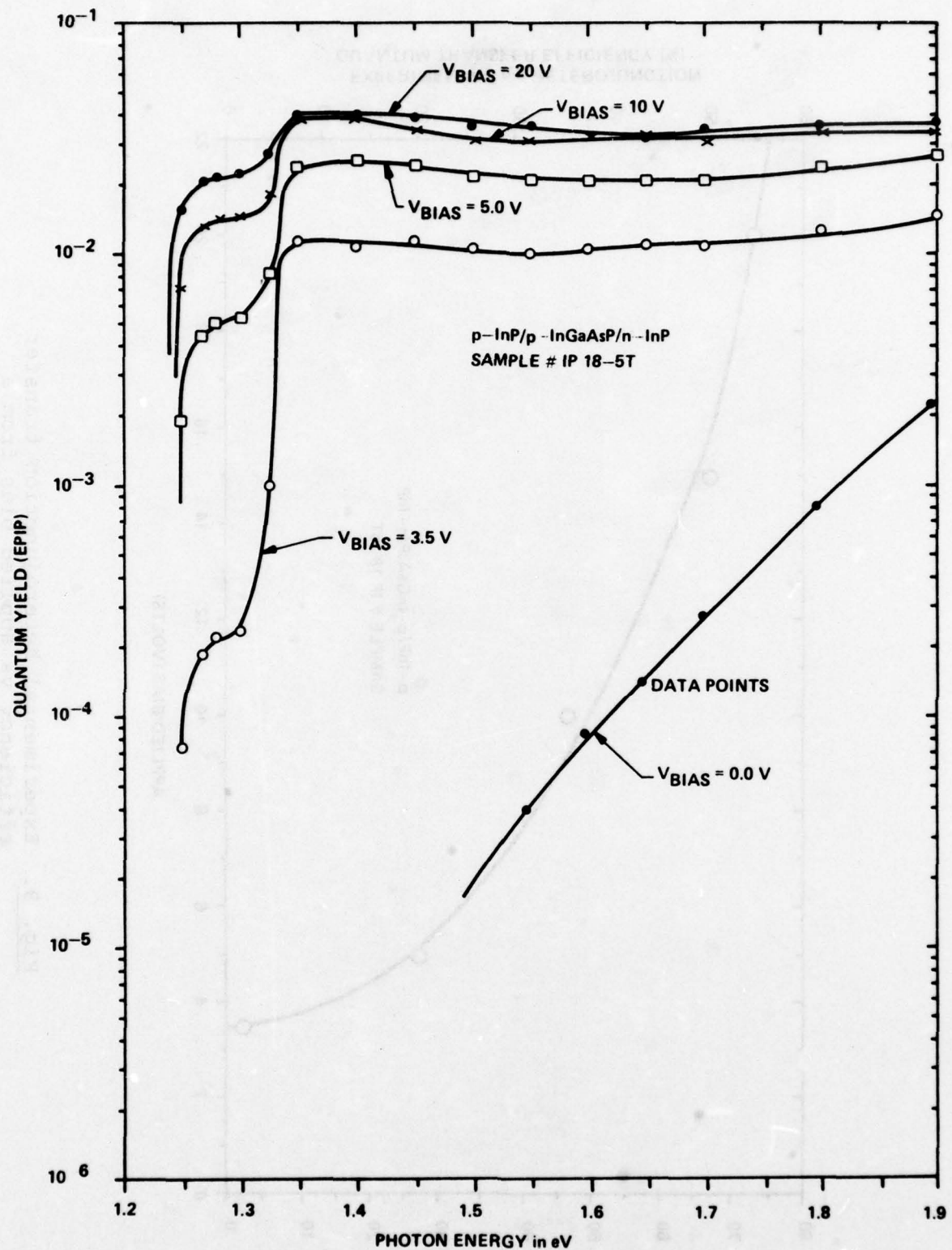


Fig. 8. Experimental reflection-mode quantum yield from the first successful hybrid heterojunction photocathode.

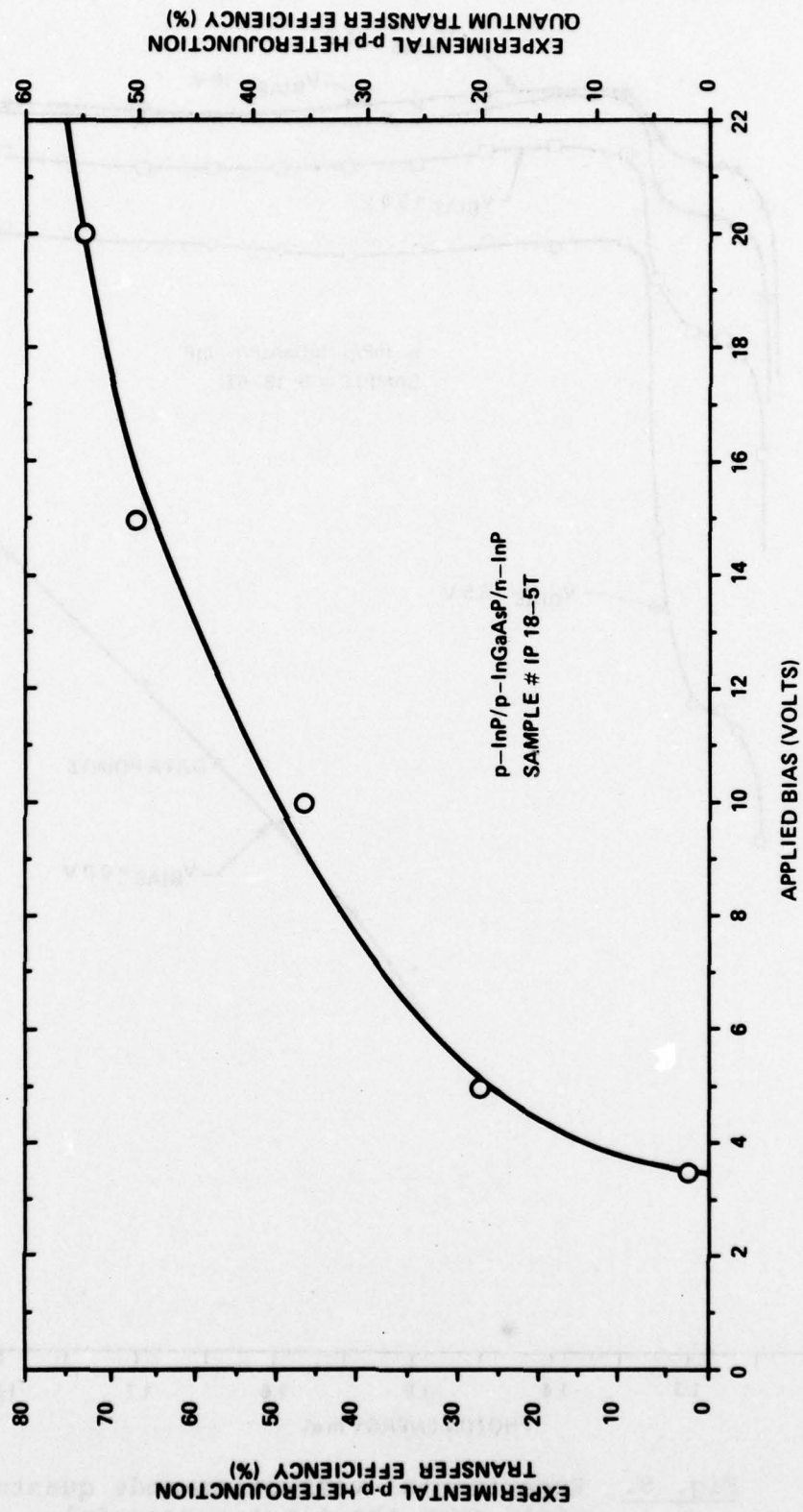


Fig. 9. Experimental heterojunction transfer efficiency vs applied bias from a hybrid heterojunction cathode.

detector feasibility. The first two designs are the direct p-InGaAsP emitter cathode and the heterojunction p-InP/p-InGaAsP cathodes discussed briefly above. The third design is a heterojunction TE cathode employing a wide bandgap p-InGaP emitter lattice-matched to a narrow bandgap p-InGaAs optical absorber. The direct emitter cathode and the InP/InGaAsP cathode have been developed especially for 1.06-micron detection under this program. A number of cathodes of each type has been fabricated and successfully vacuum tested to date. Current photoemission results and further details on the operation of each cathode can be found in Secs. 3.5 and 3.6. The remainder of this section is devoted to a detailed description of the InGaP/ InGaAs heterojunction TE cathode. It is this third cathode design which is felt to offer the highest potential 1.06-micron sensitivity and is the cathode (InGaP, in particular) which received the most attention from a materials standpoint under this contract.

Of the several requirements of the present photocathode development program, the principal difficulty lies with achieving a 20% quantum efficiency at 1.06 microns. At the present time there are two photocathodes commercially available with 1.06-micron sensitivity. The first is the standard S-1 photoemitter. Typical quantum efficiencies from an S-1 are in the range of 0.05 to 0.20% at 1.06 microns with 1.2% at 1.06 having been achieved using the multiple internal reflection effect.³² The second is a (cooled) NEA p⁺-InGaAsP cathode with a quantum efficiency of 0.5 to 3.0% at 1.06 microns.³³ In the laboratory, the highest performance NEA cathode has been a 9.0% result in the reflection mode at 300°K. This represents, approximately, a 90% probability of absorbing a 1.06 photon, 50% probability of successful electron diffusion to the emitting surface, and a 20% probability of escape into vacuum over

the interfacial barrier between the semiconductor and the Cs-O activator layer. The basic processes of optical absorption of the incoming photon and generation of an electron-hole pair are very efficient processes. The main losses occur in the transport of the photogenerated electron to the surface, and in the emission of this electron into vacuum. For the semitransparent mode of operation (light incident on the opposite side of the cathode from that which electrons are emitted), the probability that a photogenerated electron will reach the surface can be even greater than the 50% figure for a reflection-mode cathode. The net conclusion is that the problem of achieving very high quantum efficiency from a III-V photoemitter is largely a question of electron escape probability.

The highest TE escape probability observed to date from a p-InP cathode is 18% with 3-10% being more typical. Therefore one might expect a heterojunction p-InP/p-InGaAsP TE cathode to be capable of approximately 1-10% quantum efficiency at 1.06 microns. A direct p-InGaAsP emitter cathode would be expected to perform below that of an ideal InP/InGaAsP heterojunction cathode--primarily because of the lower surface escape probability from a p-InGaAsP emitter (1.15 eV) relative to a p-InP emitter (1.35 eV). A higher TE escape probability than that from p-InP would be anticipated if a larger bandgap emitter, such as p-InGaP, were used, thereby promoting the photoelectrons higher in energy at the surface relative to the vacuum level. A similar idea has recently been experimentally demonstrated in the case of NEA GaAsP alloy cathodes.³⁵ The third TE cathode design for achieving high 1.06-micron yield is based on a p-InGaP/p-InGaAs heterojunction cathode. The effectiveness of the TE emitter layer is increased by substituting InGaP of a specific composition for an InP emitter previously discussed. InGaP

has a greater bandgap at the gamma point and the upper band edges are higher in InGaP than in InP, thereby increasing the electron escape probability into vacuum.

Figure 10 is an energy band diagram for a possible InGaP/InGaAs cathode for no bias and biased operation. The InGaAs is the optical absorbing layer; the requirement for 1.06-micron response dictates that it have a 1.15 eV or lower bandgap at 300°K. Figure 11 indicates that the InGaAs composition should be approximately 16% In--i.e. $In_{.16}Ga_{.84}As$. InGaAs layers are grown routinely in this and other laboratories by vapor phase epitaxy on GaAs substrates.^{26,37} The InGaAs-GaAs (substrate) interface is latticed mismatched; however this is not an active part of the photocathode and careful compositional grading procedures have been worked out for this system. The InGaP/InGaAs (emitter-absorber) interface is lattice matched to reduce the number of potential recombination centers. Figures 12 and 13 show that the proper InGaP composition to lattice match to $In_{.16}Ga_{.84}As$ ($a_0 = 5.71 \text{ \AA}$) is approximately 63% In, i.e. $In_{.63}Ga_{.37}P$. (An $In_{.49}Ga_{.51}P$ composition is approximately correct for growing lattice -matched to GaAs substrates.) Figure 14 shows the approximate band edge energies (relative to the valence band maximum) vs InGaP composition. Note that for the $In_{.63}Ga_{.37}P$ emitter proposed, the gamma minimum is at approximately 1.7 eV and the L and X minima are at approximately 2.15 eV. Two important points can be made. First, the energies of the L and X minima are approximately 0.25 eV higher than that in InP. Therefore photoexcited electrons which are able to transfer into these valleys should have a higher probability of escape into vacuum than from InP. Second, the $E_L - E_T$ separation is about 0.15 eV less for $In_{.63}Ga_{.37}P$ than it is for InP. This would suggest that InGaP should have a higher population of electrons in the upper valleys than InP under the same internal field conditions. (Assuming that InP and InGaP have similar phonon

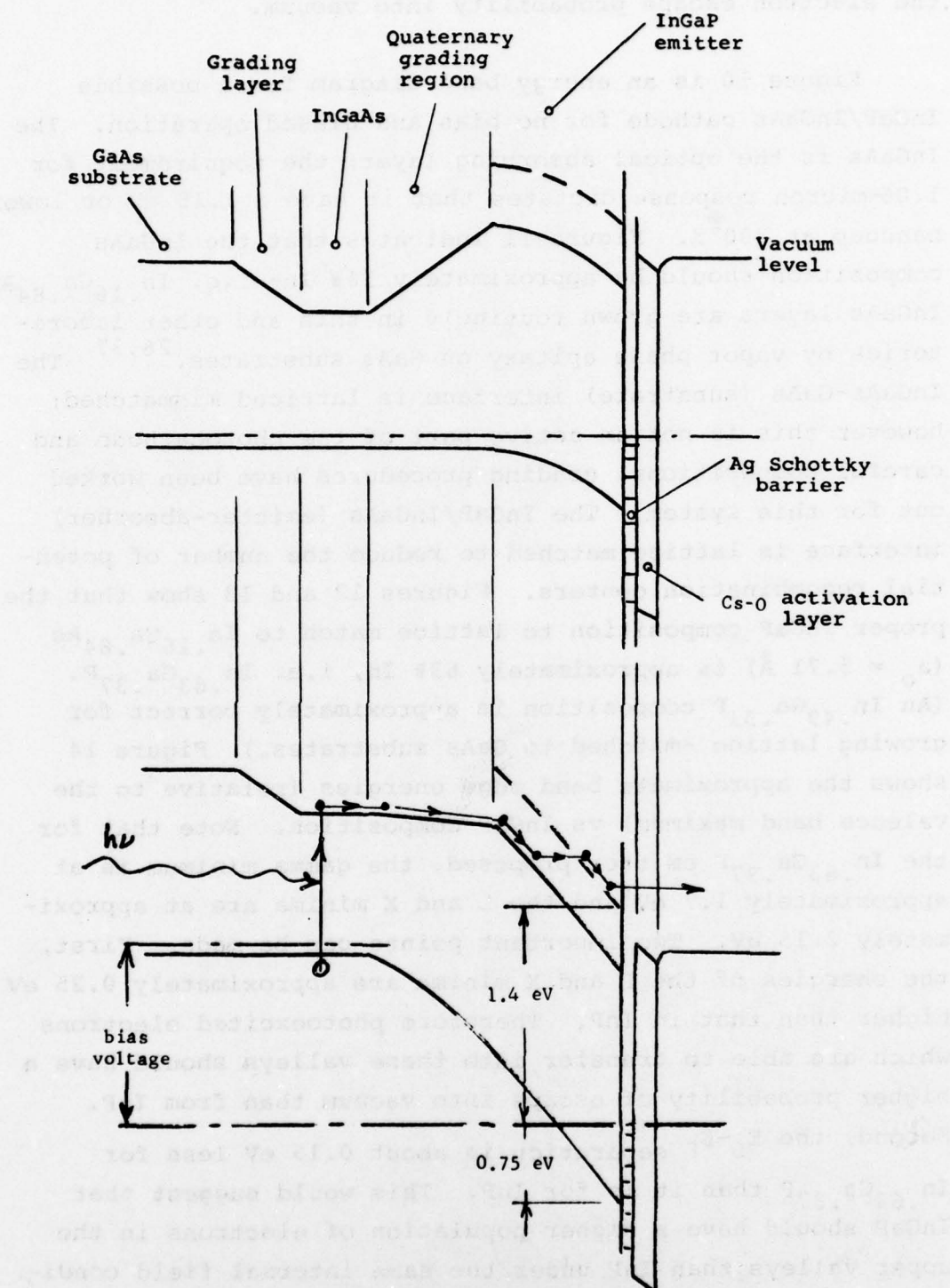


Fig. 10. Schematic energy band diagram for the InGaP/InGaAs/GaAs heterojunction TE 1.06-micron photocathode.

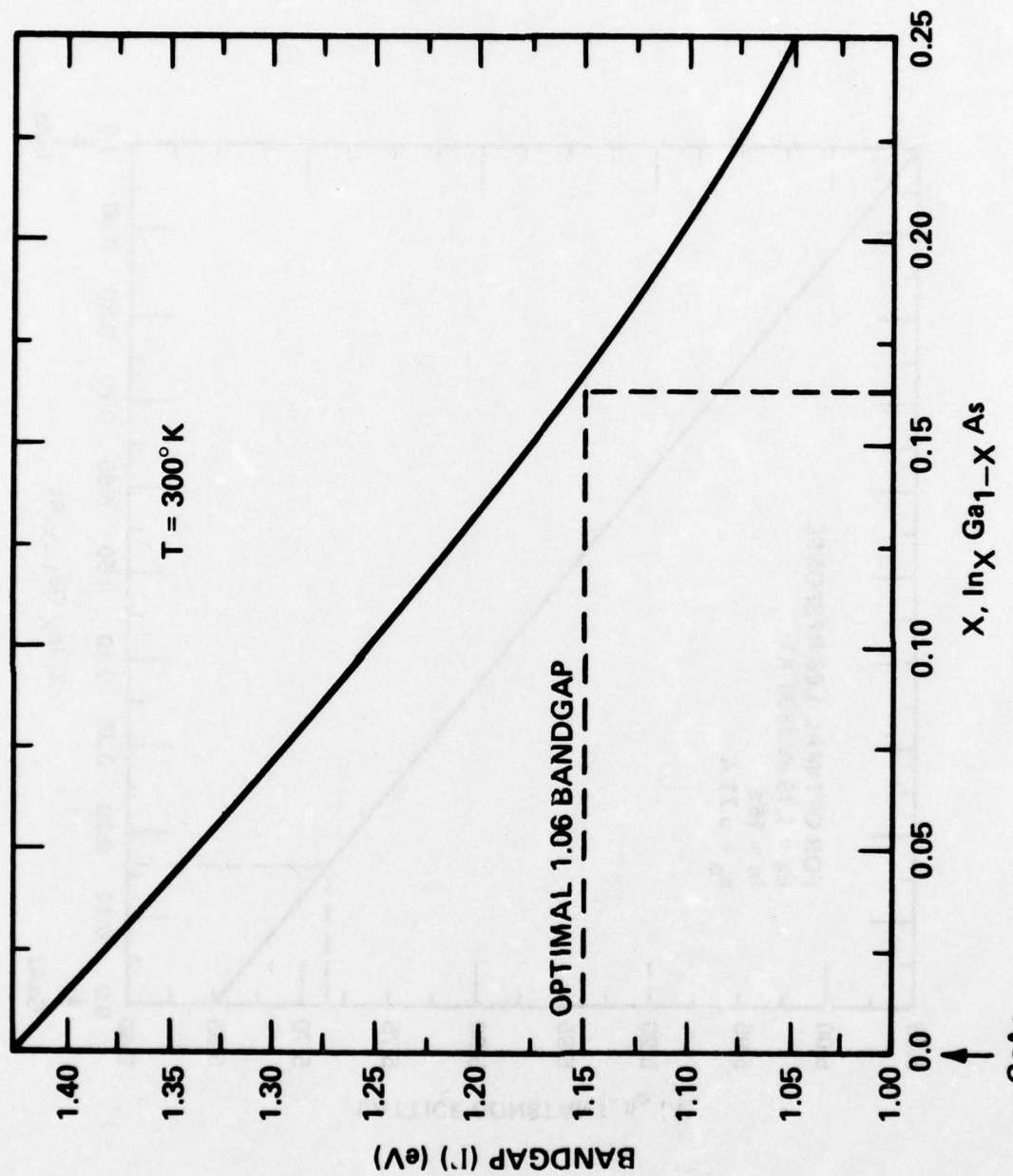


Fig. 11. Bandgap (Γ) vs composition for
 InGaAs.

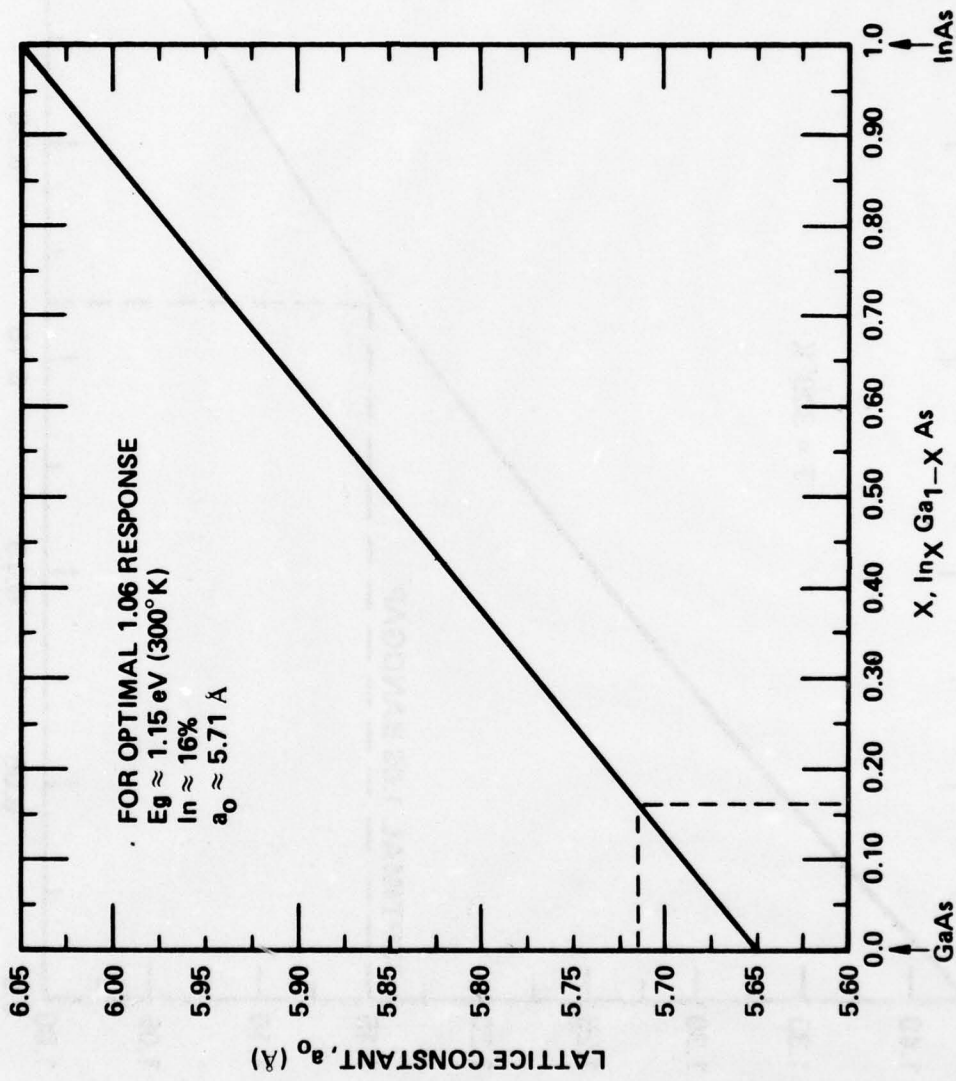


Fig. 12. Lattice constant vs composition for InGaAs.

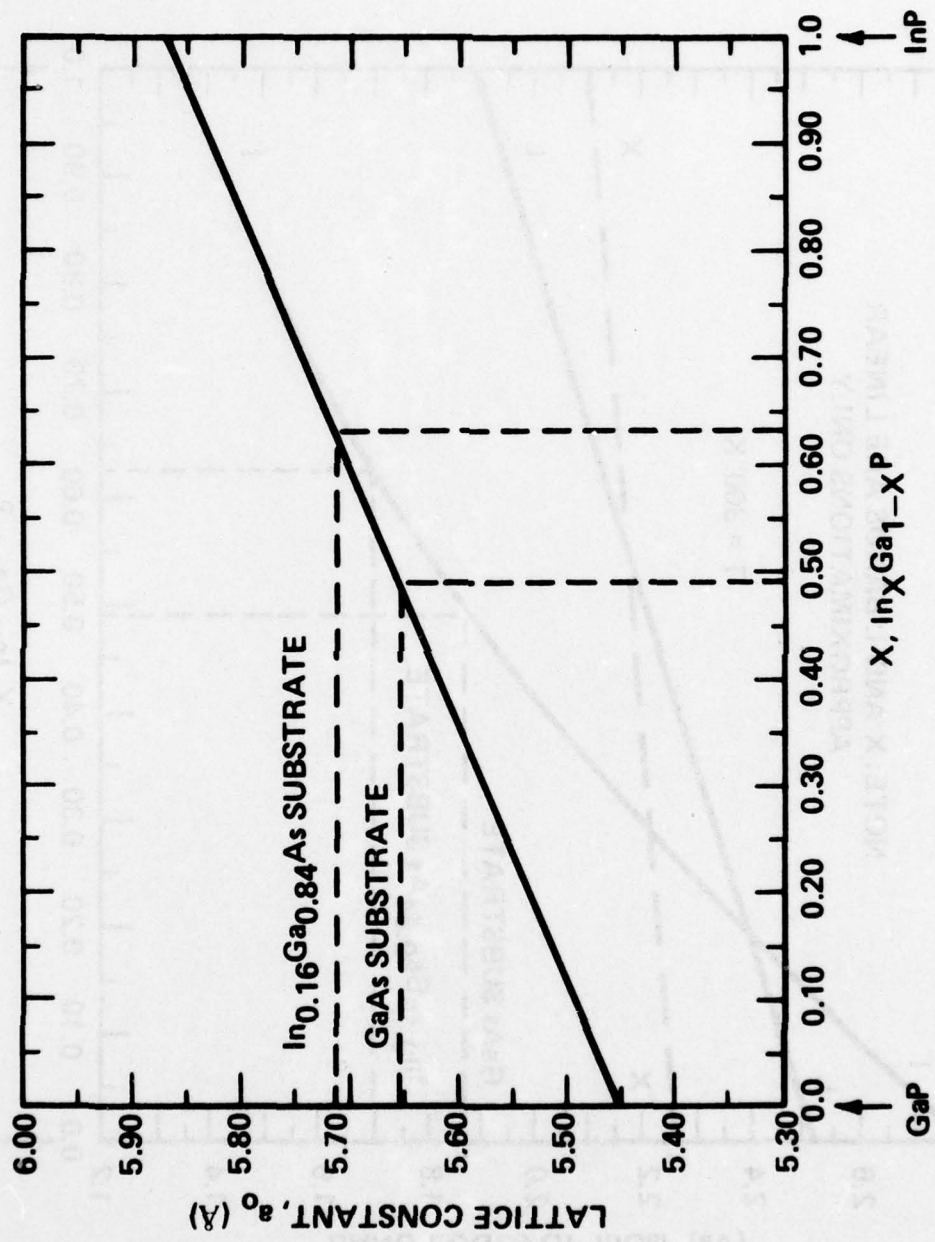


Fig. 13. Lattice constant vs composition for InGaP.

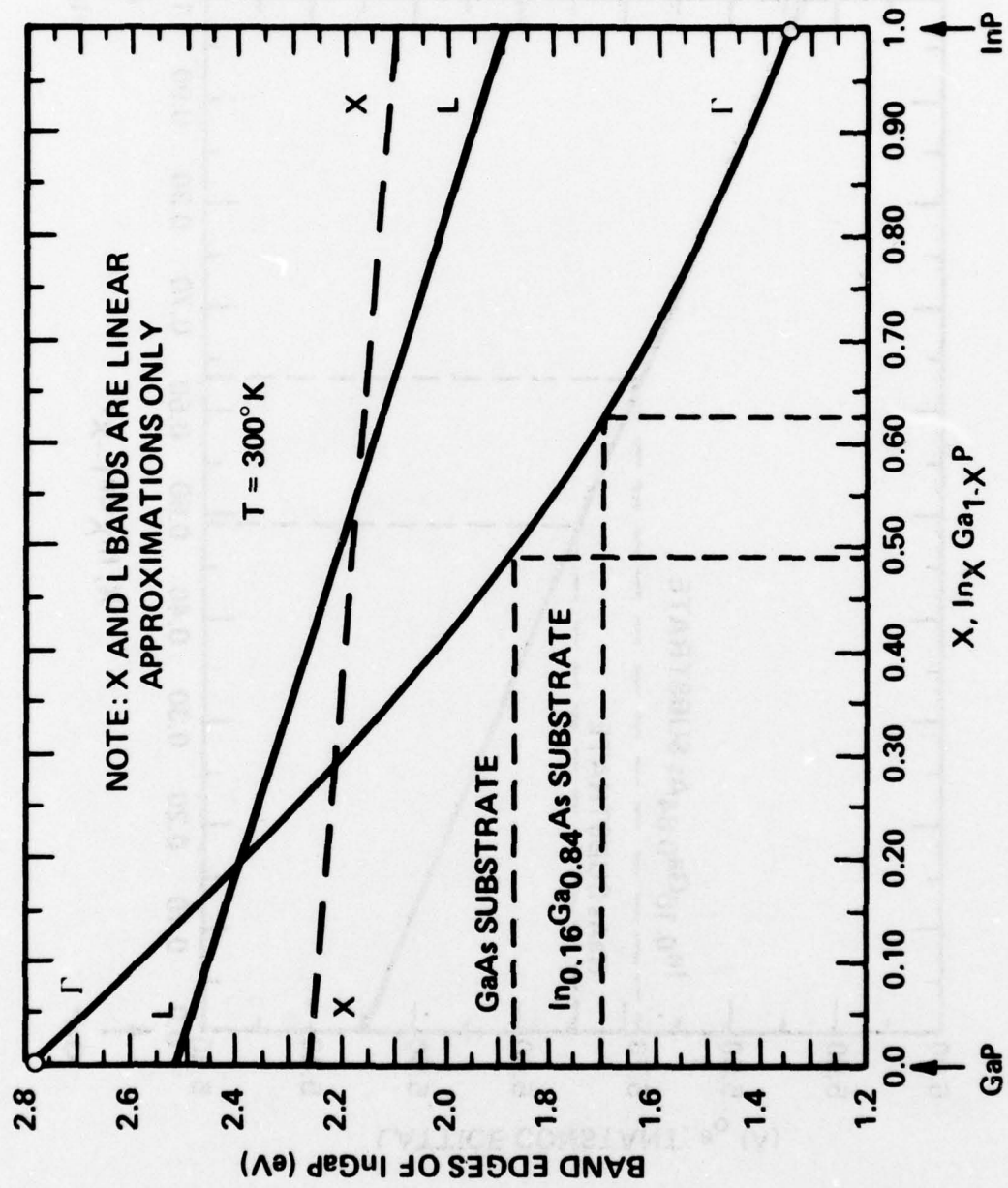


Fig. 14. Approximate band edge energies vs composition for $In_x Ga_{1-x} P$.

scattering processes, etc.) A deliberately grown InGaAsP quaternary grading region shown in Fig. 10 between the InGaAs and the InGaP is not necessary. Recent experience with both VPE-LPE and LPE-LPE InP/InGaAsP heterojunctions (not deliberately graded during growth), as well as with the VPE InGaP/InGaAs cathode, has demonstrated that deliberate grading is not necessary for good heterojunction transfer efficiency. Further discussion of this point can be found in Sec. 3.4.

We have measured the Schottky-barrier height for Au/n-InGaP to be 0.95 eV using the internal photoemission technique. The yield plot is shown in Fig. 15. The bandgap for this sample was determined to be 1.75 eV from photoluminescence, so the p-type Schottky-barrier height would be expected to be $1.75 - .95 = .80$ eV. This value is in good agreement with the value of ~ 0.75 eV that one would expect for the p-type Schottky-barrier height for all compositions of InGaP. McCaldin et al³⁸ have shown that the p-type Schottky-barrier height depends only on the anion species (P in the case of InGaP) and not on the cation. Mead³⁹ has given the p-type Schottky-barrier height as about 0.75 eV for both InP and GaP, and the InP value has been confirmed by measurements in this laboratory. The value of ~ 0.75 eV is an entirely adequate barrier height to reduce the injection into the InGaP emitter from the Schottky barrier to low values for bias voltages in the 3 to 10 volt range at room temperature.

It is difficult to predict the exact improvement in TE surface escape probability of a 1.7-eV InGaP emitter over that of InP emitter. However, work done in this laboratory on NEA GaAsP alloy cathodes gives some indication.³⁵ Figure 16 shows the NEA surface escape probability vs GaAsP bandgap. The upper mass valleys of the InGaP emitter are estimated to be approximately 0.25 eV higher than those of

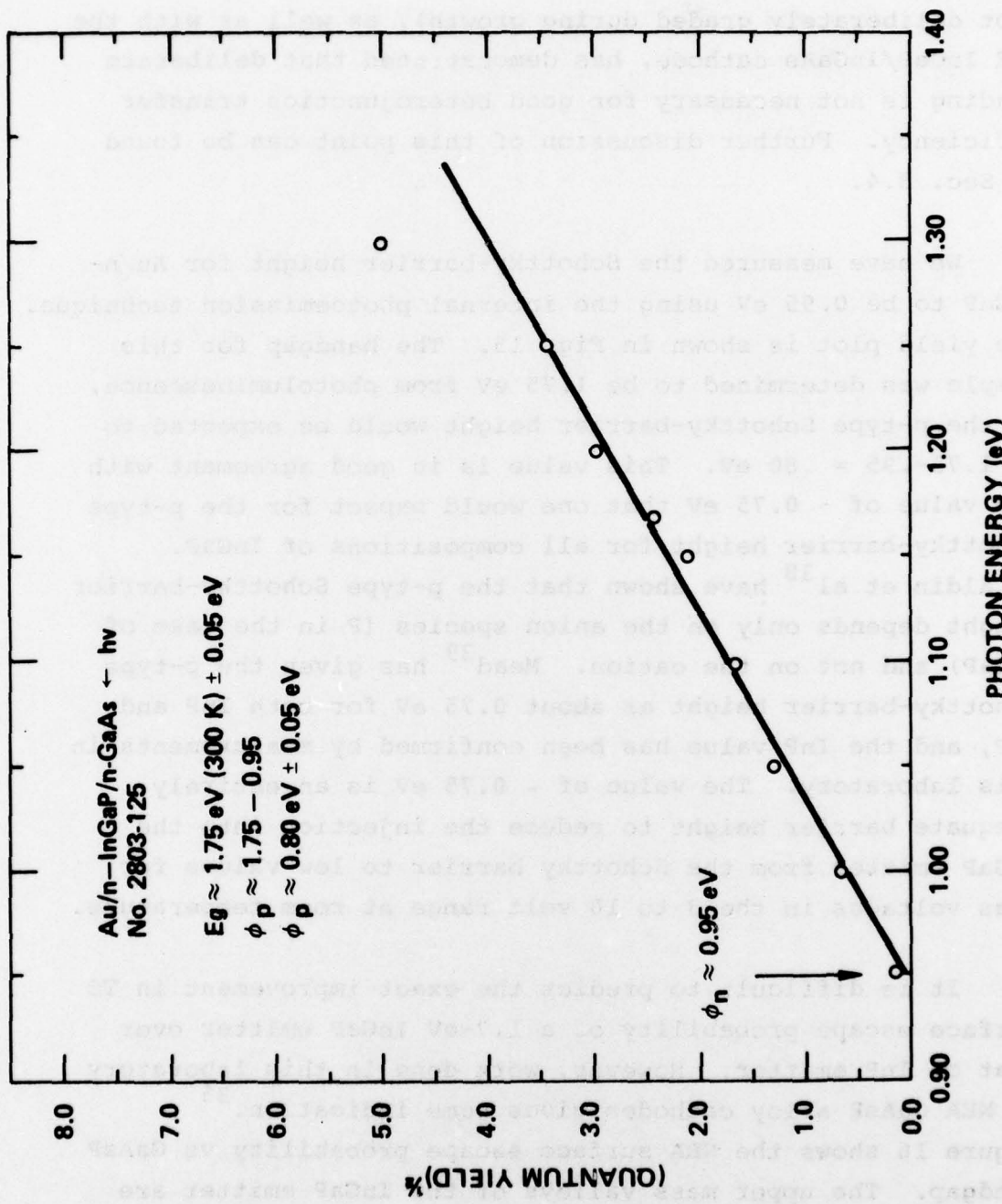


Fig. 15. Internal yield plot to determine Schottky barrier height of Ag/InGaP.

InP. Therefore if the behavior of escape probability vs bandgap shown in Fig. 16 is approximately valid, one would expect a factor of two improvement in escape probability. The actual improvement could be even better however because of a potentially higher population of photoexcited electrons in the upper mass valleys of InGaP relative to InP. Therefore the InGaP/ InGaAs design offers the highest potential 1.06-micron yield of the three cathode designs proposed. It seems reasonable to postulate that a TE surface escape probability from an InGaP emitter of 30-50% can ultimately be achieved. The photon absorption process in the InGaAs and transfer of the photoelectrons into the InGaP emitter can, in principle, be very efficient, with a 75% probability feasible. Thus the final quantum efficiency for the InGaP/ InGaAs heterojunction cathode should lie in the 20 to 30% range.

3. INVESTIGATION

3.1 LPE Growth of InGaAsP Direct Emitter TE Cathodes

The direct emitter TE cathode is the simplest of the three cathode designs in that it involves only a single epitaxial growth. The processes of photogeneration (optical absorption) and electron emission are carried out in the single grown layer. For direct bandgap III-V alloys, optimal 1.06-micron detection is achieved for a $1.15 \text{ eV} \pm 0.02 \text{ eV}$ bandgap (300°K). A slightly higher bandgap alloy would not have sufficient optical absorption at 1.06 microns and a lower bandgap would have a lower surface escape probability and Schottky-barrier height. Early TE photoemission results from p-InGaAsP cathodes, e.g. Fig. 6, indicated that a direct emitter cathode may be capable of $> 1\%$ quantum efficiency at 1.06 microns with only modest development.

an equilibrium state is attained with \dot{N}_1 constant, and below the binding energy of \dot{N}_1 only an evanescent wave is emitted and no bound electrons.

When the binding energy of \dot{N}_1 is increased and the emission current density of direct current electrons is increased, the ratio of direct current electrons to emitted electrons corresponds to the ratio of total binding energy to the binding energy of \dot{N}_1 .

For the \dot{N}_1 electron current density, the ratio of

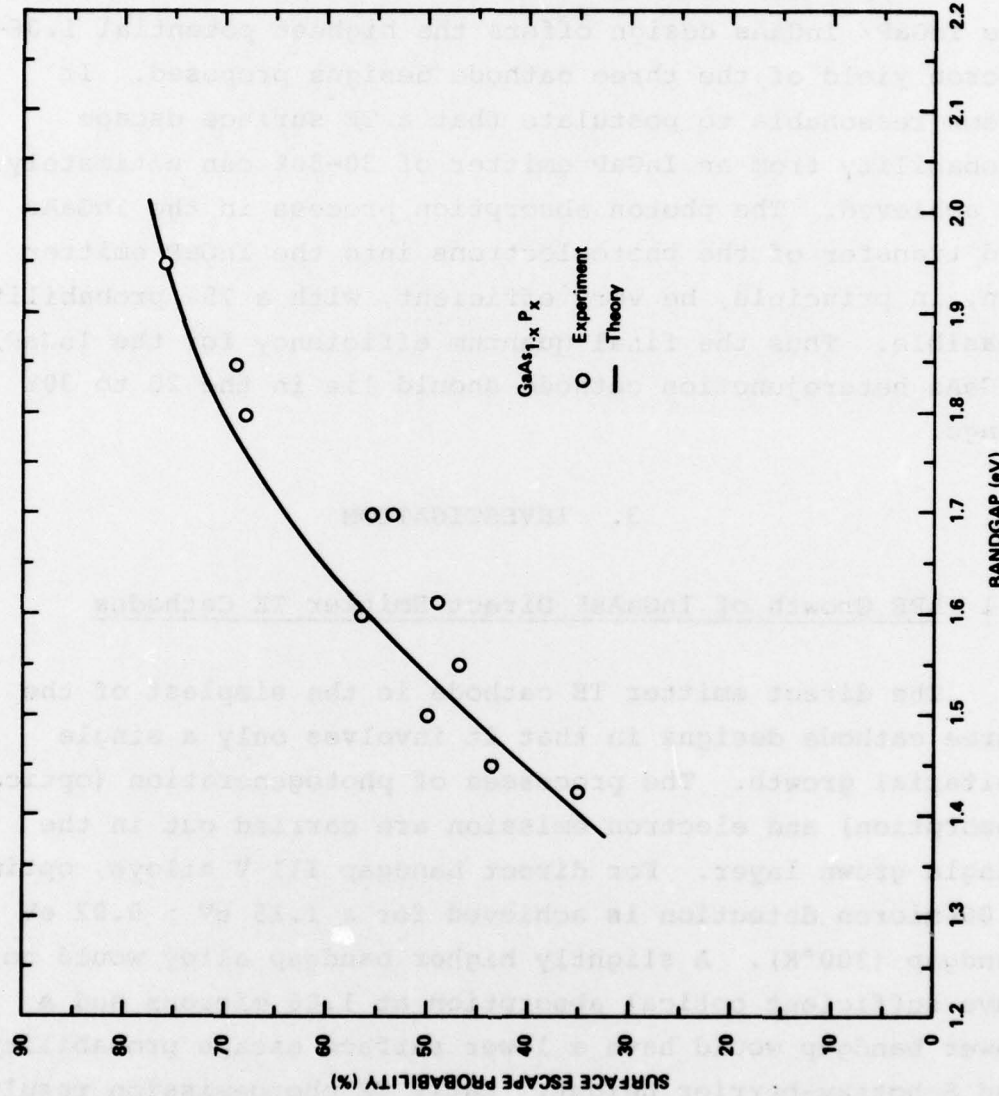


Fig. 16. Surface escape probability vs bandgap for GaAsP alloy NEA photocathodes.

Details on the LPE growth of InGaAsP alloys lattice-matched to InP substrates can be found in the literature and will not be repeated here. See Refs. 28 and 29, for example. Initially, growth of InGaAsP alloys was restricted to (111)-oriented InP substrates. However, more recent work has established the melt compositions and growth temperatures for high quality quaternary growth on (100)-InP substrates. There are some differences in the distribution coefficient of Ga for example, depending on (111) or (100) growth. The distribution coefficients of Ga, As, and P during growth have been measured and their temperature dependence fit to a simple model.⁴¹

The growth of InGaAsP for a direct emitter TE cathode is similar to that previously developed in this laboratory for NEA InGaAsP cathodes. The biggest difference is that lightly p-type InGaAsP layers are required instead of high p-type. The reason for this doping requirement is twofold. First, the Schottky-barrier leakage on p⁺-InGaAsP would be very high due to tunneling and little external bias could be applied to the cathode. Second, the depletion width or space charge region is extremely narrow (on the order of 100 Å) for p⁺-InGaAsP. Even if an external bias of several volts could be applied, the depth of the high field region would not be sufficient for there to be efficient TE photo-emission. 1000 Å or more of the high field region are needed for efficient electron transfer. This implies that a p-type doping of 10^{15} - 10^{16} /cm³ is needed. With proper care and melt preparation, LPE InGaAsP can be grown with a background level of $N_D - N_A = 1 \times 10^{15}$ /cm³ at 300°K. Therefore p-type layers in the proper range of doping can be achieved.

Figure 17 shows a typical photoluminescence (PL) spectra from a lightly doped p-InGaAsP direct emitter TE cathode. P-type doping is achieved with Zn added to the melt. The

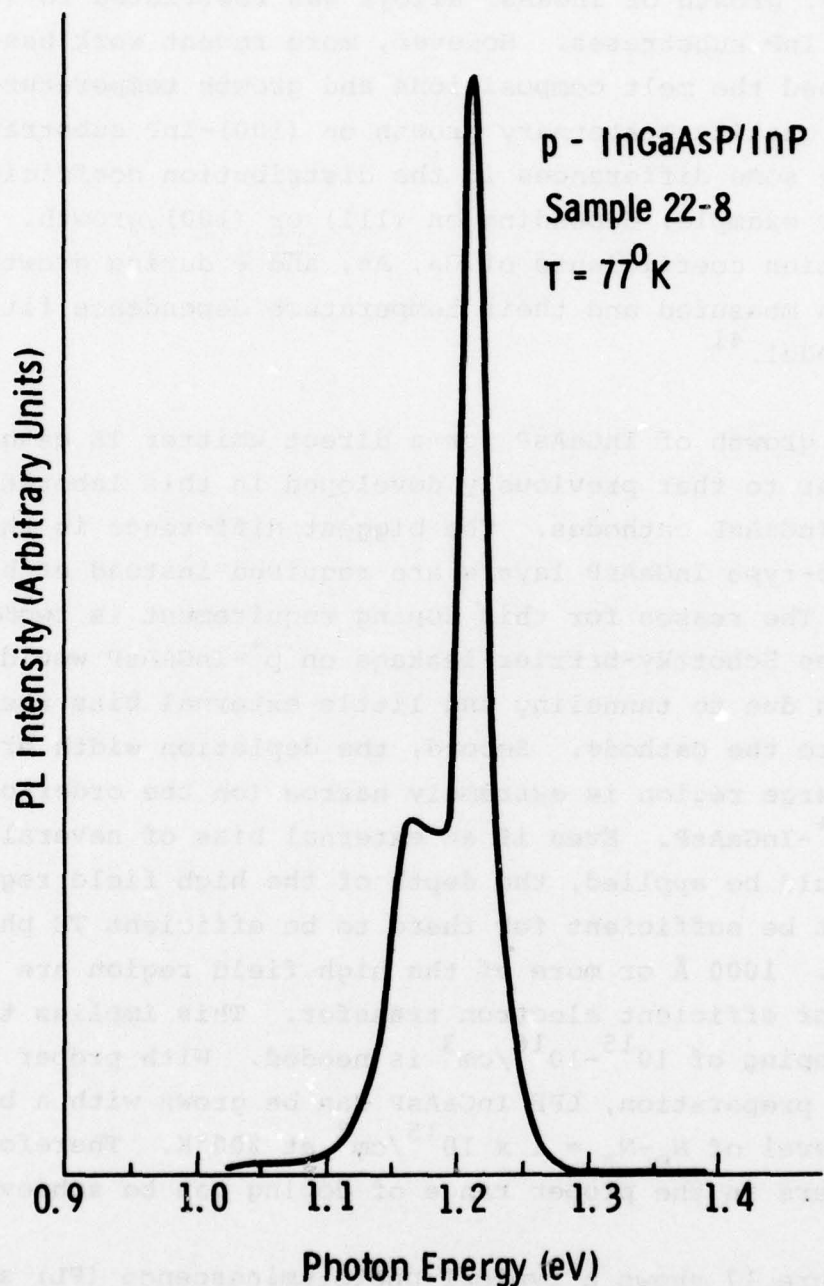


Fig. 17. Photoluminescence spectra from a p-InGaAsP direct emitter cathode at 77°K.

primary peak at 1.21 eV is near bandgap radiation⁴² and the smaller intensity side peak at lower photon energy is associated with the Zn acceptor level. Van dew Pauw measurements on the sample shown in Fig. 17 showed $N_A - N_D = 4 \times 10^{15} / \text{cm}^3$ and a mobility of $360 \text{ cm}^2 / \text{Vsec}$ at 300°K and a mobility of $630 \text{ cm}^2 / \text{Vsec}$ at 77°K . Photoemission results from direct emitter cathodes are presented in Sec. 3.5.

3.2 LPE-VPE Growth of the Hybrid Heterojunction

p-InP/p-InGaAsP Cathode

Growth of InP/InGaAsP heterojunction TE photocathodes was accomplished using a hybrid LPE and VPE technique. This hybrid growth procedure was adopted because of the need to grow low-doped active InP emitter layers, which is possible by VPE growth on (100)-oriented InP substrates. The 1.15 eV InGaAsP absorber layer doped p-type to 10^{16} cm^{-3} is grown by LPE on (100)-InP substrates. The InP emitter layer is then grown on the InGaAsP by VPE and Zn-doped to low 10^{15} cm^{-3} . The PCl_3 -In-H₂ system used for VPE growth of InP is shown schematically in Fig. 18. A high purity Spectrosil boat with 6-9's pure In is placed in a Spectrosil reactor which is heated by a two-zone furnace lined with sodium-filled heat pipes. The indium source is initially saturated with P by passing PCl_3 over the source at 750°C with purified hydrogen as a carrier gas. A H₂ dilution line and a H₂ bypass line also enters the reactor allowing adjustments to the PCl_3 mole fraction over the source and over the substrate respectively. Substrate etch conditions are obtained by diverting the PCl_3/HCl flow ahead of the source through the etch line. A zinc furnace attached to the reactor provided the p-type doping. InP is deposited on the InGaAsP/InP wafer kept at 650°C in the region of the temperature profile where the temperature variation is less than 0.5°C

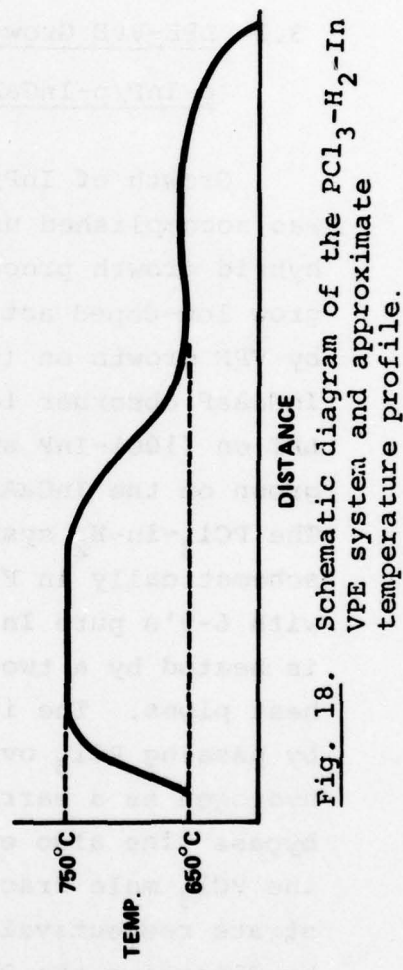
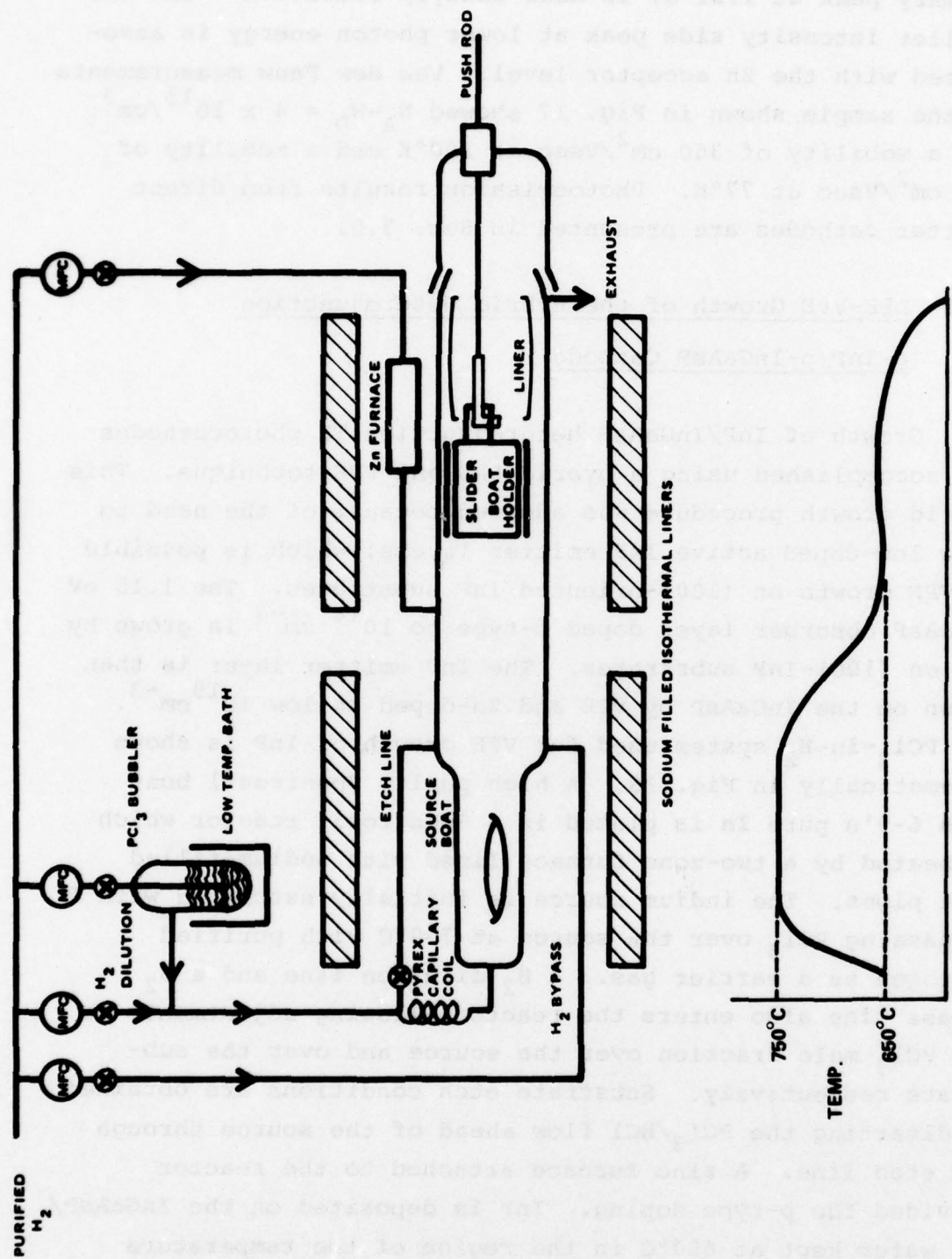


Fig. 18. Schematic diagram of the $\text{PCl}_3\text{-H}_2\text{-In}$ VPE system and approximate temperature profile.

per inch. The temperature profile at the In source is essentially flat, which eliminates source instability and yields low background doping levels.

To avoid excessive etching of the InGaAsP absorber layer (which is typically 2-4 microns thick) during source resaturation, the substrates are enclosed in the recess of a specially designed Spectrosil slider boat holder shown in Fig. 19. The polished, flat, slider plate covering the substrates is actuated by a push rod allowing controlled etch and subsequent growth while the substrates are held at 650°C throughout the growth process. A PCl_3 flow of 2070 moles/min is used over the source yielding growth rates of the order of 0.2 micron/min.

3.3 Growth of p-InGaP Emitter Cathodes

Growth of epitaxial InGaP layers has been achieved by both LPE⁴³ and VPE⁴⁴ techniques in this and other laboratories. A new VPE InGaP-InGaAs reactor was constructed to grow the InGaP/InGaAs cathodes studied under this contract. VPE homoepitaxy of InP/InP was first achieved, then VPE InGaP/GaAs, and then the growth of the complete VPE InGaP/VPE InGaAs/GaAs cathode structure was achieved.

During the initial construction phase of the VPE reactor a modest effort was made to grow LPE InGaP for the purpose of quickly demonstrating TE photoemission from InGaP. The LPE experiments are described first, followed by the VPE InGaP experiments.

3.3.1 LPE Growth of InGaP

InGaP was grown at 800°C by LPE from an In-rich melt. A Ga/In ratio of 0.014 in the melt was found to give specu-

Si source Si and Si silicon encapsulated with glass and
the substrate must be maintained below 400°C to prevent
silicon diffusion and prevent incorporation of silicon

into the substrate and to prevent extension of the
silicon source (which increases the viscosity of the source, and
thus increases the chance of contamination of the source).

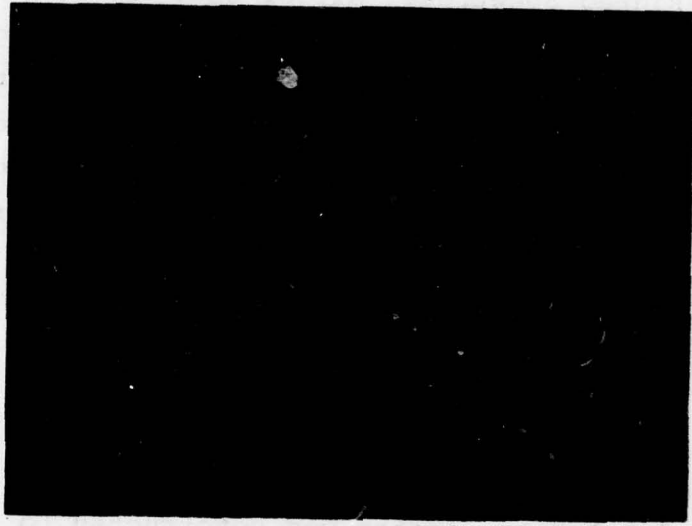


Fig. 19. Spectrosil slider boat holder and plate used to cover the substrate prior to growth.

larly reflective, near lattice-matched growth surfaces on (111)B GaAs substrates. The In-Ga melt was saturated about 10°C above growth temperature with PH₃. After homogenizing, the melt was cooled down to 800°C at a cooling rate of 0.04°C/min. The melt was then pushed over the substrate and cooled further. Melt wipe-off was invariably good. Although the melt was resaturated before each growth to compensate for the loss of P, good growths were difficult to reproduce. The surface quality was found to deteriorate and the density of growth hillocks increased sharply with two to three growths from the same melt. Low doping levels and better surface quality were observed when the epilayers were less than 0.5 micron thick. Thicker layers showed high doping levels and deterioration in surface quality. Use of graphite boats lined with pyrolytic boron nitride did not significantly improve the background doping level. Figure 20(a) shows the surface micrography of a 0.4 micron thick InGaP epilayer grown on (111)B GaAs that showed a background doping level of $0.4 \times 10^{16} \text{ cm}^{-3}$, whereas Fig. 20 (b) is the micrograph of a 4-micron thick layer grown from the same melt which showed a doping level of $2.5 \times 10^{17} \text{ cm}^{-3}$. The change in doping level and surface quality indicates a change in the melt composition during the growth which leads to lattice mismatch and strain with a consequent increase in carrier concentration. Several LPE InGaP/GaAs samples were vacuum tested for TE photoemission with negative results. In all cases the effective acceptor density was quite high, resulting in extremely leaky Schottky barriers and relatively high zero bias yields from the p-InGaP surface.

From this point of view, VPE--although more complicated--has the advantage of yielding fixed compositions, the capability of varying the composition at which to lattice-match a substrate, and the ability to grade for composition. Background doping levels in VPE material are dictated, in principle, by the purity of the sources of the gases used.

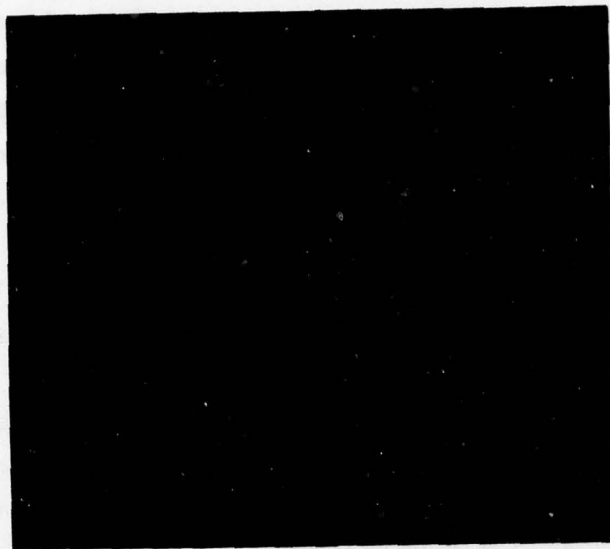


Fig. 20A. Surface micrograph of a 0.4-micron thick InGaP layer grown by LPE.



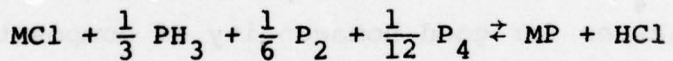
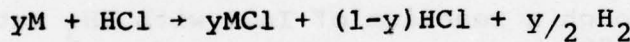
Fig. 20B. Surface micrograph of a 4.0-micron thick InGaP layer grown from the same melt as that used in Fig. 20A.

3.3.2 VPE Growth of the InGaP/InGaAs/GaAs Cathode

The main emphasis in the VPE growth of InGaP/InGaAs heterojunctions has been on establishing the growth conditions for InGaP layers lattice matched to InGaAs. Although InGaP/InGaAs heterojunction devices have been reported in the literature, the growth conditions have not been discussed.^{45,46,47} The growth conditions for InGaAs graded on GaAs substrate have been established at Varian and are used in the heterojunction growth.³⁷ The growth of InGaP lattice matched to GaAs has been reported extensively and forms the basis for the heterojunction growth conditions established in this study.^{46, 48-50} A brief literature survey of the previous work on the VPE growth of InGaP is given first. This is followed by descriptions of the experimental set-up, early difficulties, and the procedures established. The growth parameters and the characterization of the grown layers are discussed in the next section.

Previous Work

The basic equations governing the growth of InGaP can be written as follows:



where M represents either of the In and Ga metals and P_2 , P_4 are products formed by the decomposition of PH_3 at high temperatures.⁴⁸

The growth of InGaP ternary alloys is complicated by the need for precise control of a number of parameters. Due to the large difference in their free energy of formation, the GaP component is much more readily deposited than InP.⁴⁸

reactor design, furnace profile, etc. Hence for each new reactor system it is necessary to go through an initial stage of experimentation to determine the optimum conditions for the desired growth.

Experimental Set-Up

A schematic diagram of the reactor used for vapor phase epitaxial (VPE) growth of InGaP is shown in Fig. 21 and a picture of the system itself in Fig. 22. (This includes all the modifications to the initial setup to date.) The growth system can be divided into three zones. In the first zone, In and Ga metal sources are placed in two separate chambers and a mixture of HCl and H₂ is passed over each. The HCl reacts with the metal sources to form volatile metal chlorides which are swept downstream. The system has a provision for using either electronic grade HCl/H₂ gas mixture or higher purity HCl from cracking AsCl₃ at high temperatures. Since under typical growth conditions the HCl flow over the Ga source is much smaller than that over the In source, extra H₂ is added to the HCl(Ga) so that equal total flow of gases over both the sources can be maintained. This ensures equal residence time of gases on the sources. A baffle is placed in each of the source chambers to enhance mixing and residence time and to avoid back-diffusion of gases toward the sources.

In the central zone various gases are introduced. By-pass H₂ and HCl for etching the deposits on the reactor walls and the substrate are brought in. For p-type doping, a H₂ stream passing over a heated Zn pellet is used. Electronic grade gas mixtures of 10% PH₃/H₂ and 10% AsH₃/H₂ are also introduced in this zone. All the gas flows are controlled by Tylan mass flow controllers.

In the third zone deposition takes place. A slider boat (Figs. 23 and 24) is used for InGaP growth. This design protects the substrates during equilibration of gases

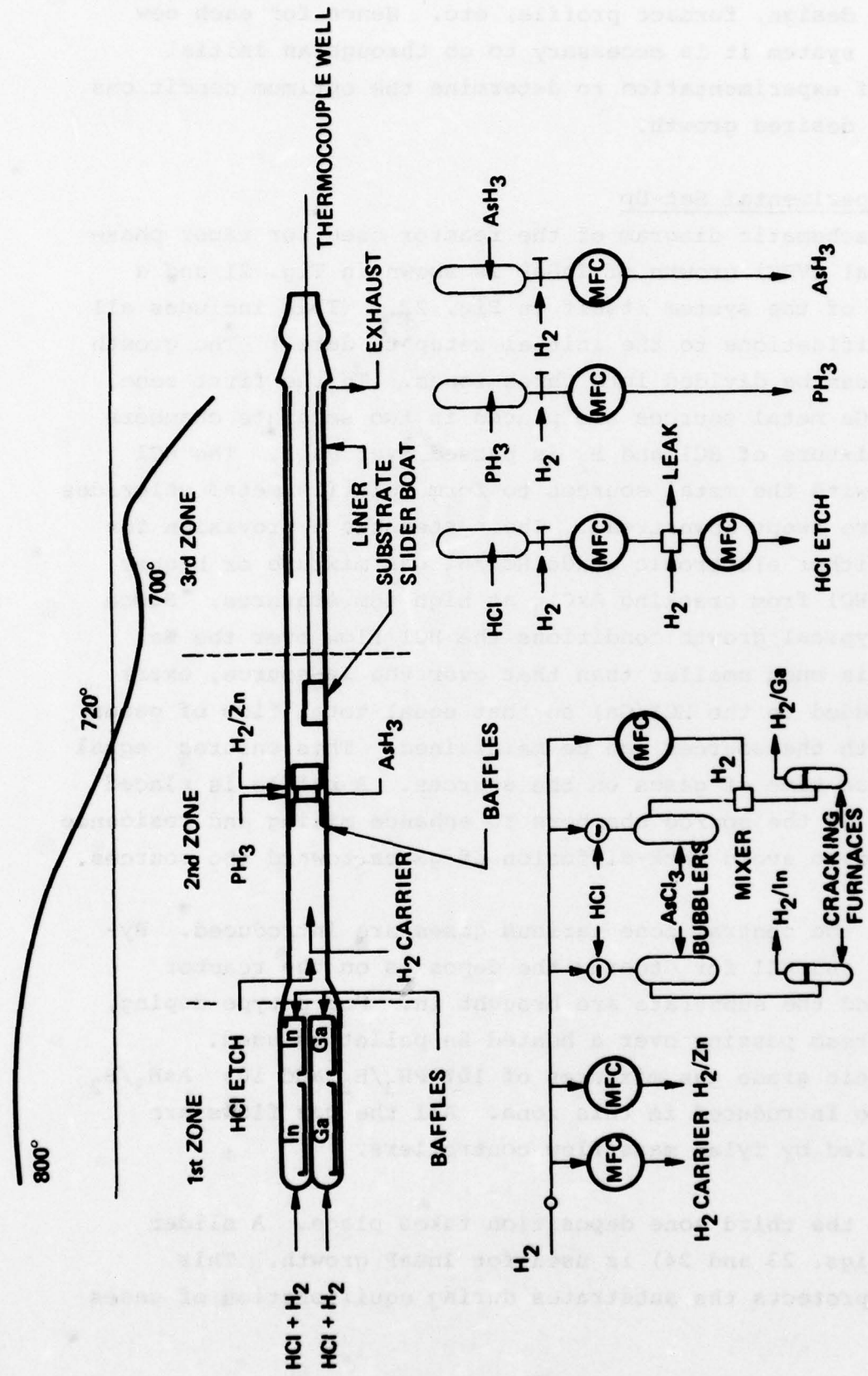


Fig. 21. Schematic diagram of the VPE InGaP-InGaAs system.



Fig. 22. Photograph of the VPE InGaP-InGaAs reactor system.

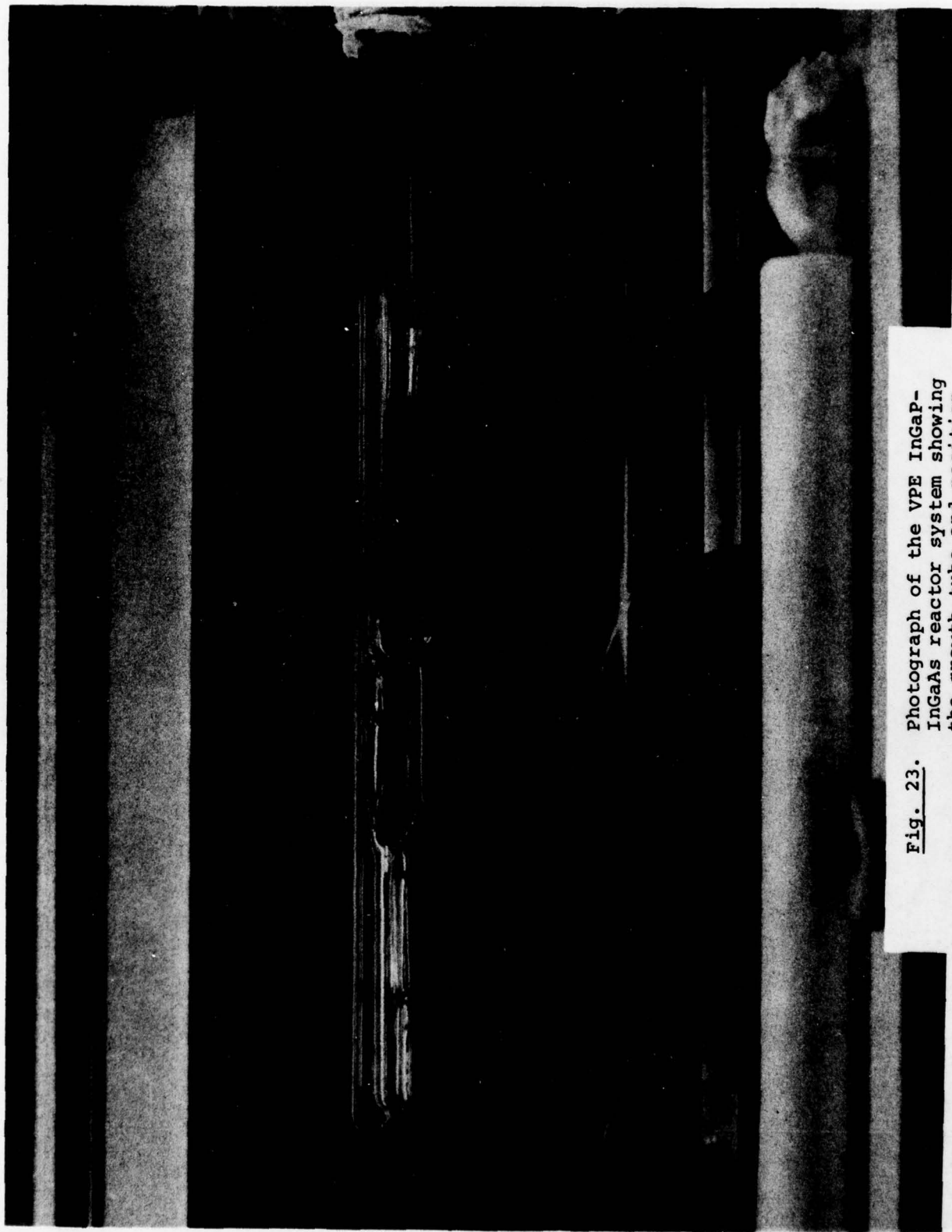


Fig. 23. Photograph of the VPE InGaP-InGaAs reactor system showing the growth tube and position of the slider boat.

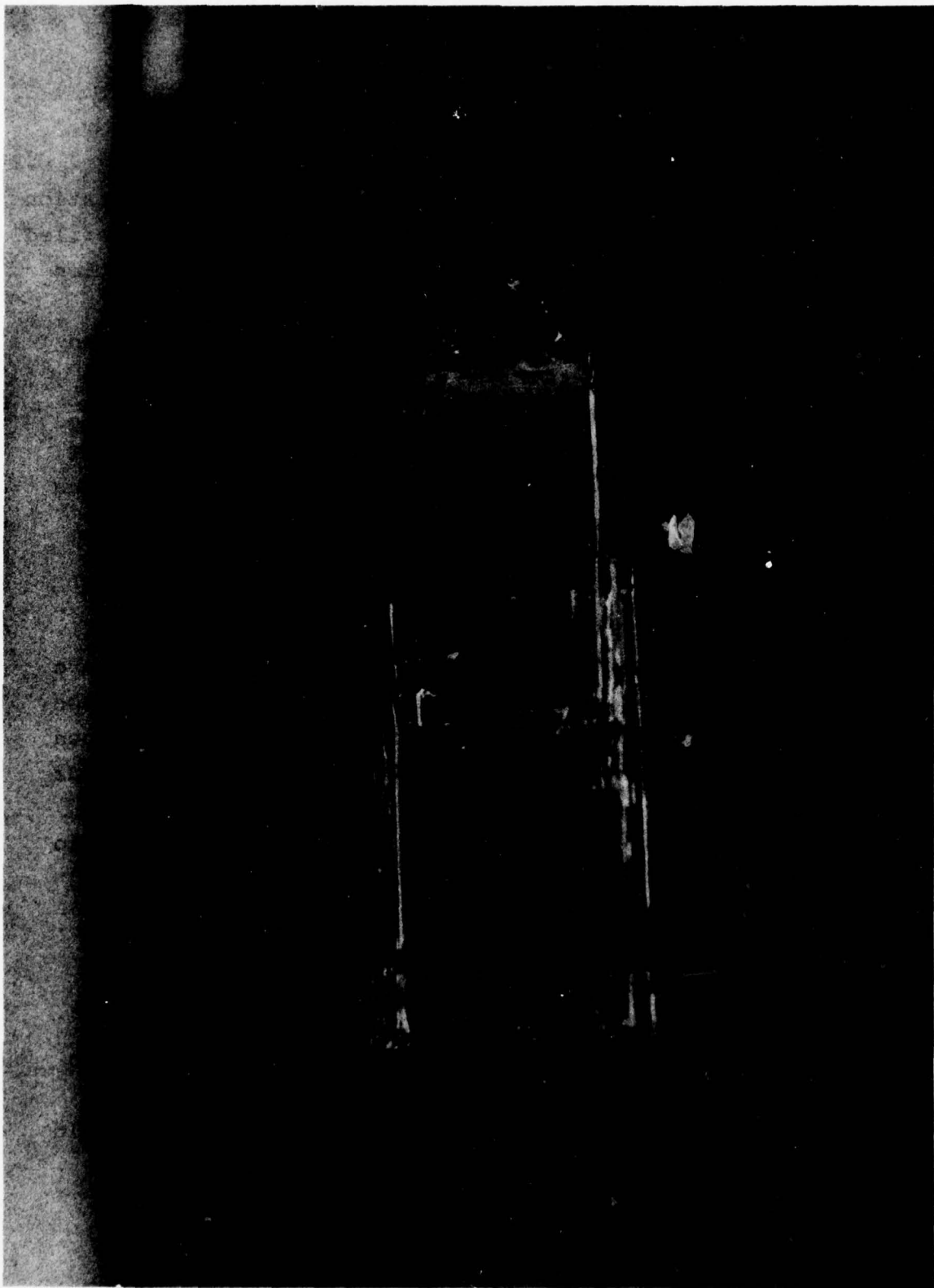


Fig. 24. Photograph of the slider boat and cap with two substrate wafers in place.

until stable growth conditions are reached, allows controlled HCl etching of the substrates, and makes it possible to attain abrupt changes in the grown layers.

Early Difficulties

The reactor assembly was complete and ready for operation by the end of June 1977. The single-zone furnace was profiled to obtain a flat source zone at $\sim 800^{\circ}\text{C}$ and a flat deposition zone at $720\text{--}730^{\circ}\text{C}$. Since a primary requirement was low background doping material, HCl from cracked AsCl_3 was used in the beginning. From the measurement of As deposited in the cracking furnace it was determined that the AsCl_3 cracking efficiency was almost 100%. However, the cracking furnace for AsCl_3 would get clogged with too much As and had to be changed after about five hours of run time. Also, because of the large HCl flow, the In source would deplete quite rapidly and had to be replenished to ensure complete conversion of HCl to MC₁ and maintain reproducible growth. Hence the initial experiments were necessarily slow and were further slowed down due to temperature drifts in the furnace. As mentioned earlier, the composition is strongly influenced by the deposition temperature. Any drift during a run leads to compositional grading of the growth layer. The furnace problems also caused the temperature to vary from one run to another.

Most of the effort initially concentrated upon making design changes to incorporate desired features into the system. The position of the dilution H_2 line was changed and the baffle system was modified to prevent backdiffusion of PH_3 to the source. Prevention of PH_3 contamination of the sources was desirable because, while the In source could be easily baked out and most dissolved gases removed, the

Ga source, once contaminated, had to be changed because of P saturation. A Ga/H₂ mixer was installed to ensure equal residence time of gases on the sources.

The first objective was to establish conditions for growth of InGaP lattice-matched to GaAs (which occurs for about 50% InP)⁵¹ and then go on to VPE growth of InGaAs/GaAs and InGaP/InGaAs/GaAs. The initial experiments confirmed the ease with which GaP deposits compared to InP. In spite of judicious choice of parameters based upon careful literature survey,^{44,48,49,50} the first layers grown were too high in GaP content. The surface appearance was also poor, the growth nonuniform, and a slight orange appearance indicated a high GaP content. After incorporating the changes mentioned above both the visual appearance and photoluminescence of the InGaP growth improved. Apart from continuing furnace problems it was now possible to effect changes in the grown layer by changing parameters.

To establish appropriate conditions for growing InGaP lattice-matched to GaAs, two experimental approaches were used. First, the ratio of In(HCl)/Ga(HCl) was changed and, second, the PH₃ flow compared to MCl was changed. Excess PH₃ compared to MCl tended to produce a poor quality surface. Although the growth rate did increase with PH₃ flow as expected,⁵⁰ the composition was still too high in GaP content. For good surface quality (e.g. fewer hillocks, specularly reflective, uniform area coverage, etc) it was decided to grow InGaP under conditions of PH₃ \leq MCl. By changing the In(HCl)/GA(HCl) ratio with fixed Ga(HCl) and PH₃ flows modest success was achieved toward this end. Since the use of HCl from cracking AsCl₃ was limiting the total number of growth runs before having to clean the system, commercial electronic grade HCl was used as the HCl source.

It was found beneficial to have a gentle temperature gradient from the PH_3 entry point to the substrate position to reduce excessive wall deposits. Too high a gradient slows down the growth rate and affects the composition by nonuniform depletion of the gas stream. The total bypass H_2 flow was also increased to reduce wall deposits and obtain maximum deposits at the substrate position.

With these changes to optimize conditions for InGaP growth lattice-matched to GaAs, reasonably good growth of nearly lattice-matched InGaP to GaAs was achieved.

To more quickly establish the feasibility of the proposed InGaP/InGaAs heterojunction photocathode, InGaP growth on already available InGaAs (grown in another VPE reactor) was successfully pursued. The PL spectrum and surface micrograph for InGaP/InGaAs sample #2-18 are shown in Figs. 25 and 26, respectively. The PL spectrum is sharp with clearly resolved side bands^{51,53} and the surface shows the characteristic cross-hatch pattern.

The furnace instabilities were found to be due to a manufacturing defect in the furnace itself. An improved three-zone furnace was then purchased for the InGaP system. After installation of the new furnace, some time was spent in adjusting shunts and set-points to obtain the desired temperature profile. InGaP layers lattice-matched to GaAs were grown with the new furnace. The PL spectrum from sample #3-2 is shown in Fig. 27. The spectrum has two clearly resolved side bands.^{51,53} The surface was shiny but with a few hillocks.

Procedures

The temperature profile of the 3-zone furnace is shown in the reactor schematic diagram. All the results discussed below were obtained with this profile.

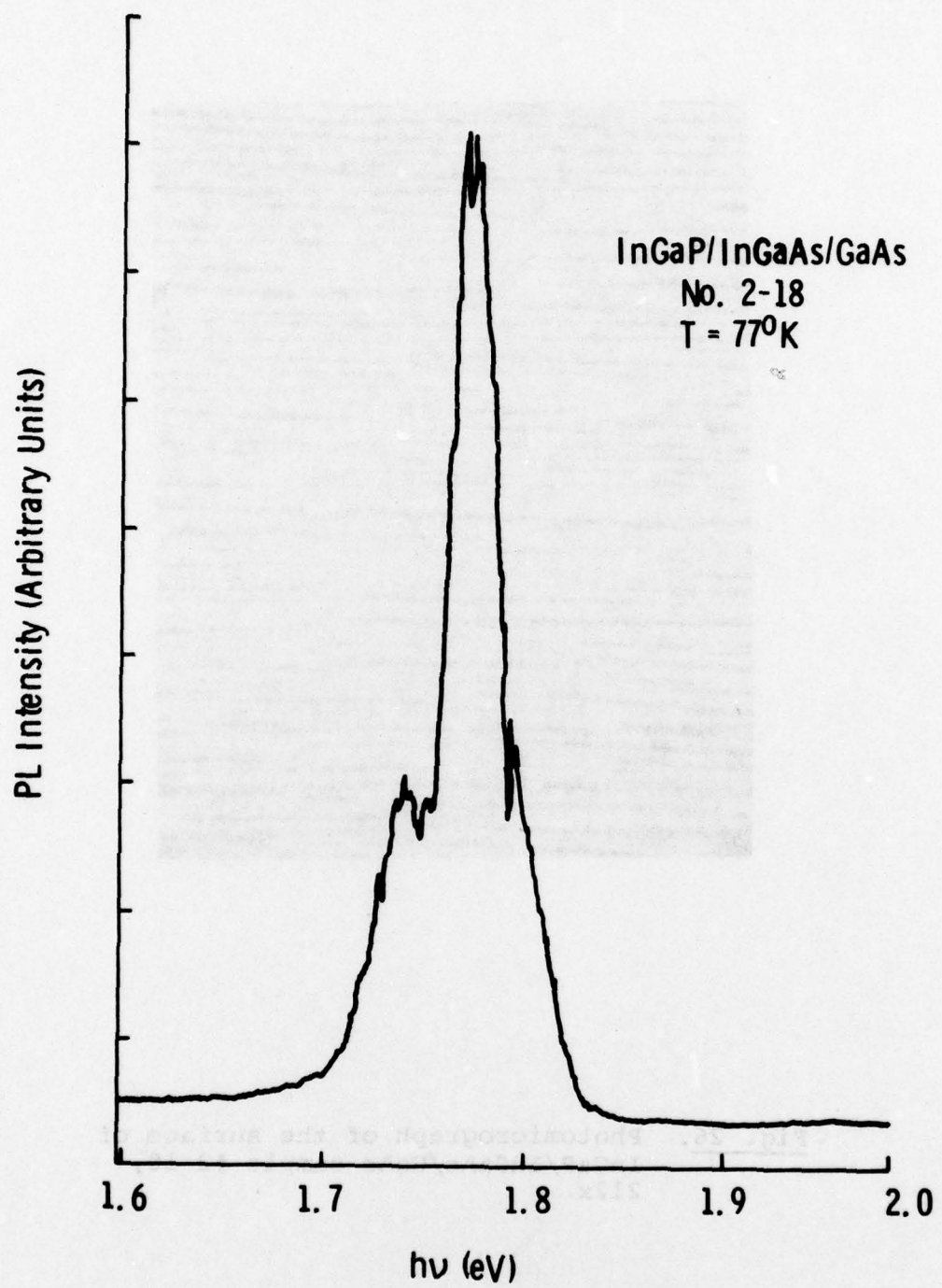


Fig. 25. Photoluminescence spectrum from InGaP/InGaAs/GaAs sample #2-18 taken at 77 K.

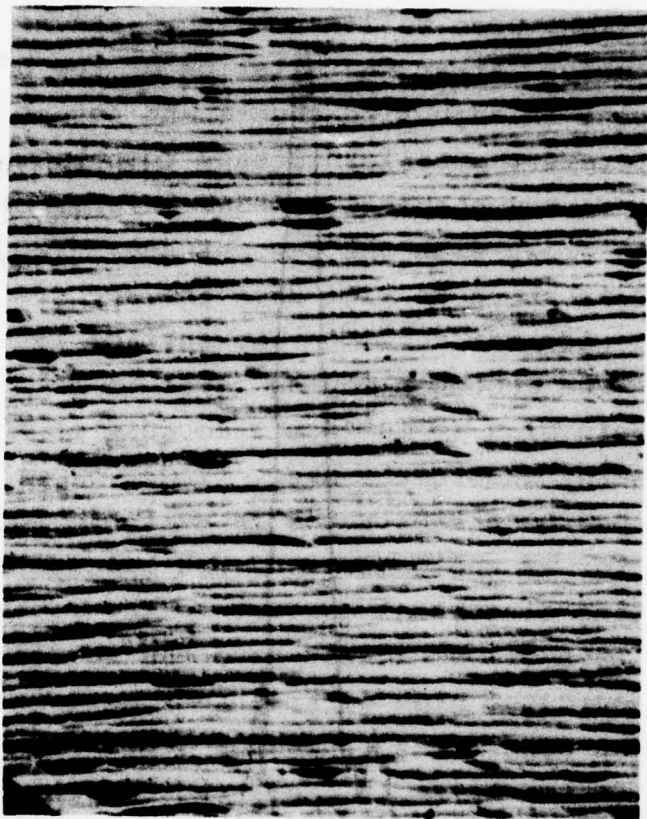


Fig. 26. Photomicrograph of the surface of
InGaP/InGaAs/GaAs sample #2-18,
212x.

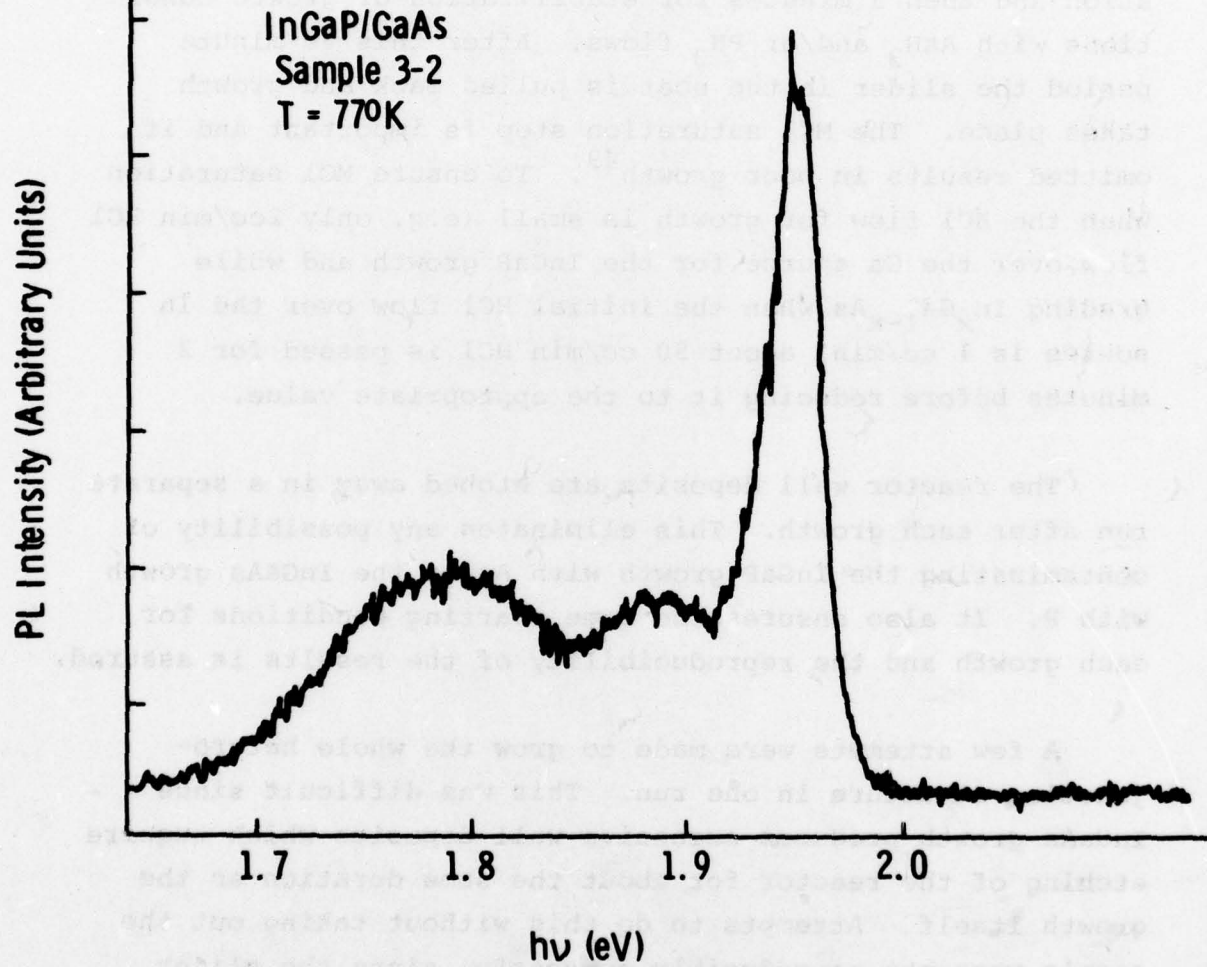


Fig. 27. Photoluminescence spectrum from InGaP/GaAs sample #3-2 taken at 77°K.

The optimum position for growth was experimentally determined to be about 8 cm. downstream from the PH_3 and AsH_3 entry position as shown in Fig. 21. Thus, the growth takes place at 720°C on a temperature slope of $5^\circ\text{C}/\text{cm}$. The bypass H_2 flow is adjusted to obtain maximum deposits at the substrate position.

A typical growth experiment consists of 15 minutes of thermal equilibration, followed by 10 minutes of MCl saturation and then 5 minutes for stabilization of growth conditions with AsH_3 and/or PH_3 flows. After this 30-minute period the slider in the boat is pulled back and growth takes place. The MCl saturation step is important and if omitted results in poor growth⁴⁹. To ensure MCl saturation when the HCl flow for growth is small (e.g. only 2cc/min HCl flow over the Ga source for the InGaP growth and while grading $\text{In}_x\text{Ga}_{1-x}\text{As}$ when the initial HCl flow over the In source is 1 cc/min) about 50 cc/min HCl is passed for 2 minutes before reducing it to the appropriate value.

The reactor wall deposits are etched away in a separate run after each growth. This eliminates any possibility of contaminating the InGaP growth with As or the InGaAs growth with P . It also ensures the same starting conditions for each growth and the reproducibility of the results is assured.

A few attempts were made to grow the whole heterojunction structure in one run. This was difficult since InGaAs growth produces excessive wall deposits which require etching of the reactor for about the same duration as the growth itself. Attempts to do this without taking out the sample were not reproducibly successful since the slider boat is not completely leak free and some uncontrolled etching does take place causing poor InGaP growth. Hence it was decided to grow InGaAs and InGaP layers in separate runs.

To prepare the GaAs substrate for InGaAs growth, the first step is pad polishing with $\text{Br}_2\text{-CH}_3\text{OH}$ solution. Just before putting in the reactor the polished substrates are ultrasonically solvent cleaned (TCE, ACE, Alconox) and a 4:1:1 etch ($\text{H}_2\text{O}:\text{H}_2\text{SO}_4:\text{H}_2\text{O}_2$) is used followed by an isopropyl alcohol rinse. For InGaP growth the graded InGaAs layers are pad polished using very light $\text{Br}_2\text{-CH}_3\text{OH}$ solution and then solvent cleaned before putting in the reactor. No 4:1:1 etch is used since it could remove too much of the grown layer.

The grown layers were characterized using X-ray diffraction for lattice constant determination, 77°K photoluminescence (PL) measurements and vacuum photoemission studies. The composition values determined from these techniques are in reasonable agreement with each other. The background doping of the reactor was found to be $1 \times 10^{15} \text{ cm}^{-3}$ for InGaP layers grown on GaAs:Cr.

$\text{In}_x\text{Ga}_{1-x}\text{As}$ Growth: For $\text{In}_x\text{Ga}_{1-x}\text{As}$ growth on GaAs equal flows of AsH_3 and total MCl (50 cc/min) are used. Under typical growth conditions a thin layer of GaAs is grown first, followed by a graded region and finally a constant composition layer of desired thickness. Step grading is used in our experiments since it results in reduced overall dislocation density.⁴⁶ A digital Data Trak programmer Model 6610 is used to change the HCl flows over the sources in a specified manner for step grading. The step grading program is based upon $\text{In}_x\text{Ga}_{1-x}\text{As}$ growth parameters experimentally established at this lab and published data.^{36,37,54} The grading rate is about 5 mole %/cm. The Ga flows used are shown in Fig. 28. The In flows are kept at 50-Ga flow.

The $\text{In}_x\text{Ga}_{1-x}\text{As}$ layers are shiny in appearance with a fine crosshatch pattern as shown in Fig. 29. This arises

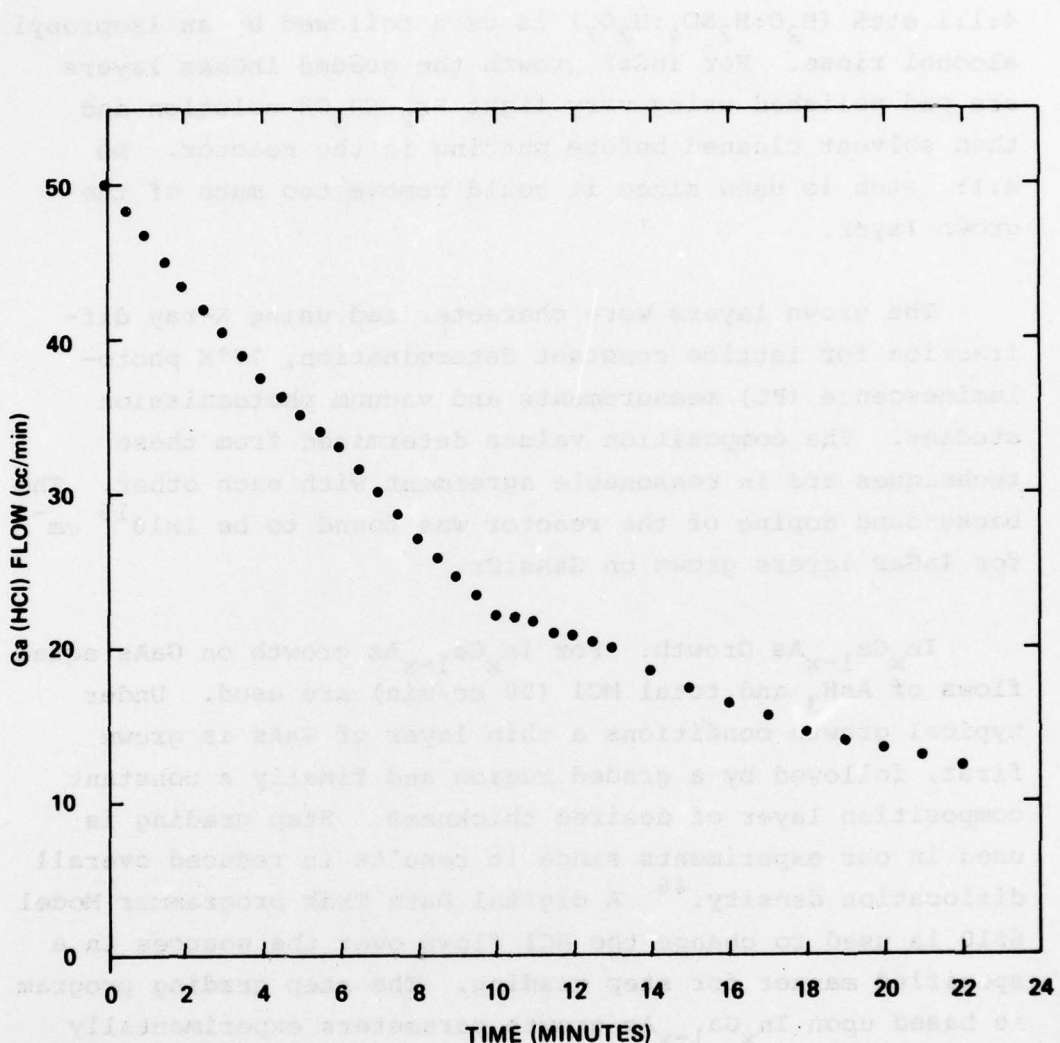


Fig. 28. Ga(HCl) flow program used for InGaAs grading.



Figure 29. Photomicrograph of the surface of InGaAs/GaAs sample #SR 1-32, magnification 291X.

from the dislocation network generated in the graded region.³⁶ Sharp PL spectra are obtained from these layers (see Fig. 30). Van der Pauw measurements on $In_{.16}Ga_{.84}As$ grown on Cr-GaAs gave mobility values of $944 \text{ cm}^2/\text{V-sec}$ at 77°K and $146 \text{ cm}^2/\text{V-sec}$ at 300°K . The corresponding doping levels were $1.9 \cdot 10^{16} \text{ cm}^{-3}$ and $7.4 \cdot 10^{16} \text{ cm}^{-3}$. Typical growth rates are $0.15\text{--}0.2 \mu\text{/min.}$

InGaP Growth: To establish appropriate conditions for growing InGaP two experimental approaches were used. First, the ratio of $In(\text{HCl})/\text{Ga}(\text{HCl})$ was changed and second, the PH_3 flow compared to MCl was changed. Since excess PH_3 compared to MCl tended to produce a poor quality surface, it was decided to grow InGaP under conditions of $\text{PH}_3 < \text{MCl}$. This finds support in a study of GaAs grown by the hydride process where improved lifetime and diffusion length of minority carriers is obtained when $\text{ASH}_3 < \text{GaCl}$.⁵⁵

To grow $In_xGa_{1-x}P$ layers lattice matched to $In_xGa_{1-x}As$ substrates the HCl flow over the In source is adjusted. The HCl flow over the Ga source and the PH_3 flow are kept fixed at 2 cc/min and 50 cc/min respectively.

Since 77°K photoluminescence is routinely used to characterize the grown layers, a relationship between the $In(\text{HCl})$ flow needed to grow lattice-matched InGaP layers and the InGaAs substrate bandgap at 77°K has been established and is shown in Fig. 31. Although the same program was always used for growing InGaAs, the variation in the InGaAs compositions grown (hence the range of bandgaps in Fig. 31) is due to minor changes in the system from run to run. For example, the Ga and In source surface area changes as the sources are depleted, and there are small changes in the source and substrate temperature from run to run. Also each time the reactor is taken down for cleaning and reinstalled,

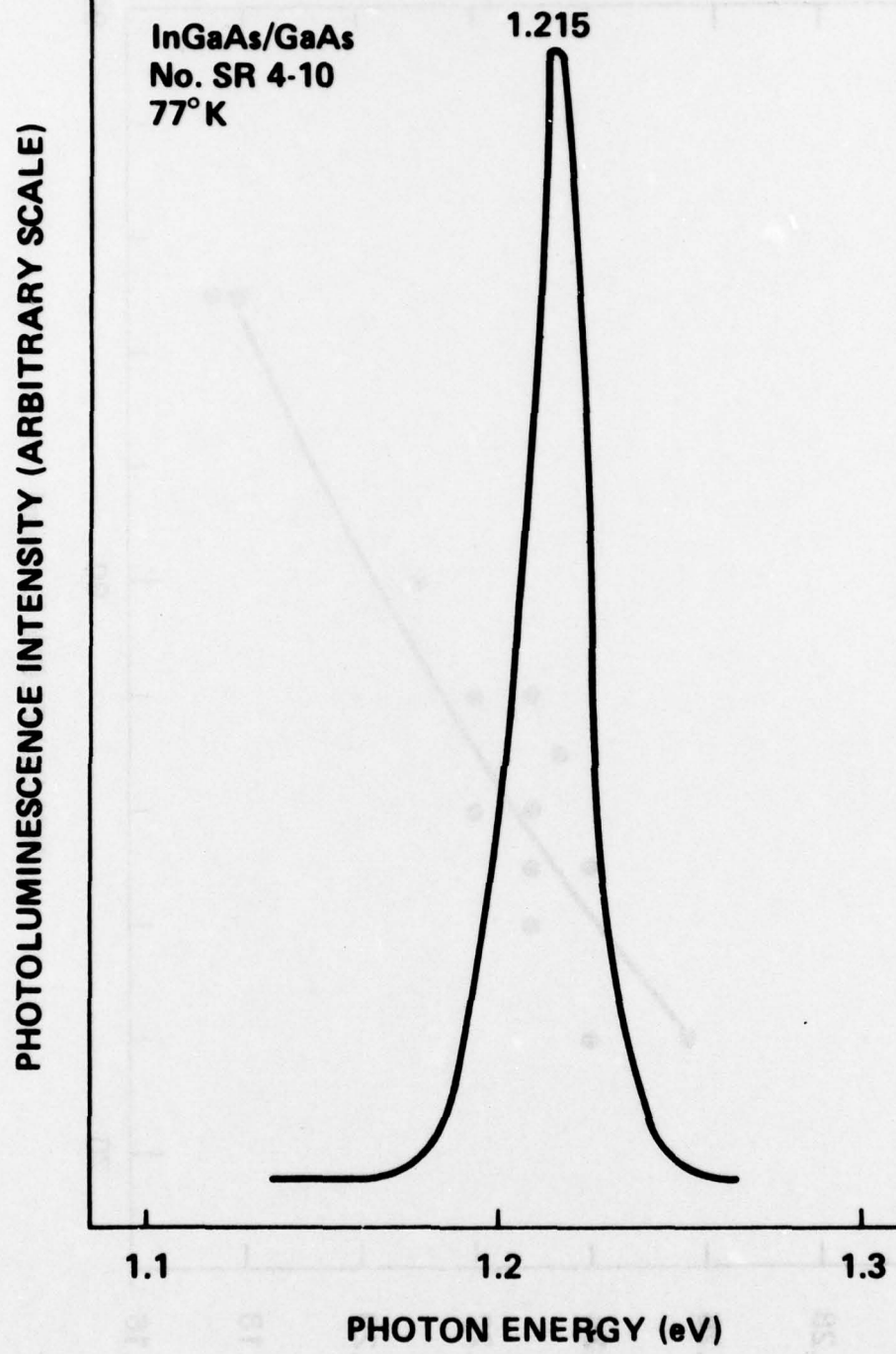


Fig. 30. Photoluminescence spectrum of InGaAs/GaAs sample #SR4-10.

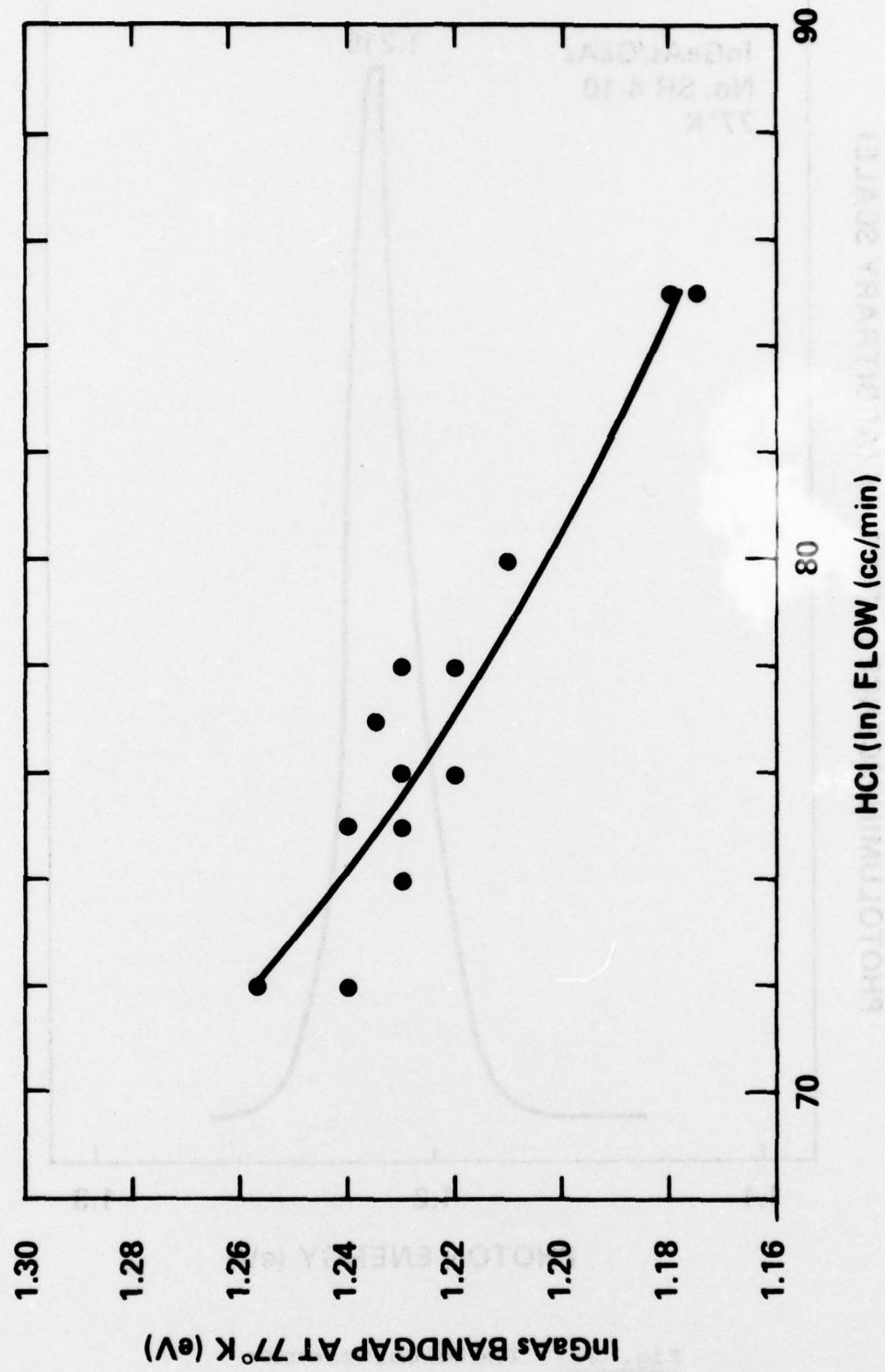


Fig. 31. HCl (In) flow needed for growth of InGaP lattice-matched to an InGaAs layer of a given bandgap.

the positioning is not identical and the temperature profile can be slightly shifted. The scatter in the In(HCl) flows needed to grow lattice-matched InGaP is also caused by the same variation.

The relationship between the InGaAs bandgap at 77°K and that of InGaP is shown in Fig. 32. No attempt has been made to draw the expected relationship since there exists a wide variation in the InGaP bandgap vs composition in the literature.⁴³ These data points are for the best heterojunctions grown. The best growths are characterized by sharp PL spectra, uniform coverage, specularly reflective surface and a good cleavage. For the few samples where X-ray diffraction was performed the layers were found to be lattice matched.

A certain amount of lattice latching has also been observed while growing $In_xGa_{1-x}P$ on $In_xGa_{1-x}As$ substrates. Two substrates of differing Eg at 77°K (1.18 and 1.21 eV) were placed next to each other and lattice-matched growth was obtained on both of them. The In(HCl) flow used was intermediate between the flows needed for lattice-matched growths separately.

It must be emphasized that very critical control of parameters is needed to grow good quality InGaP layers. A 2 cc/min change in the In(HCl) flow can easily ruin the growth. It has been found that when the grown layer is shiny in the middle and dark around the edges the In(HCl) flow needs to be reduced for lattice-matched conditions. When the In(HCl) flow is less than required the growth is patchy and dull in appearance. From Auger studies As has often been seen on the surface of such wafers.

These growth conditions have been established for equal source boats whose exposed surface is 1.5 cm x 10 cm. in

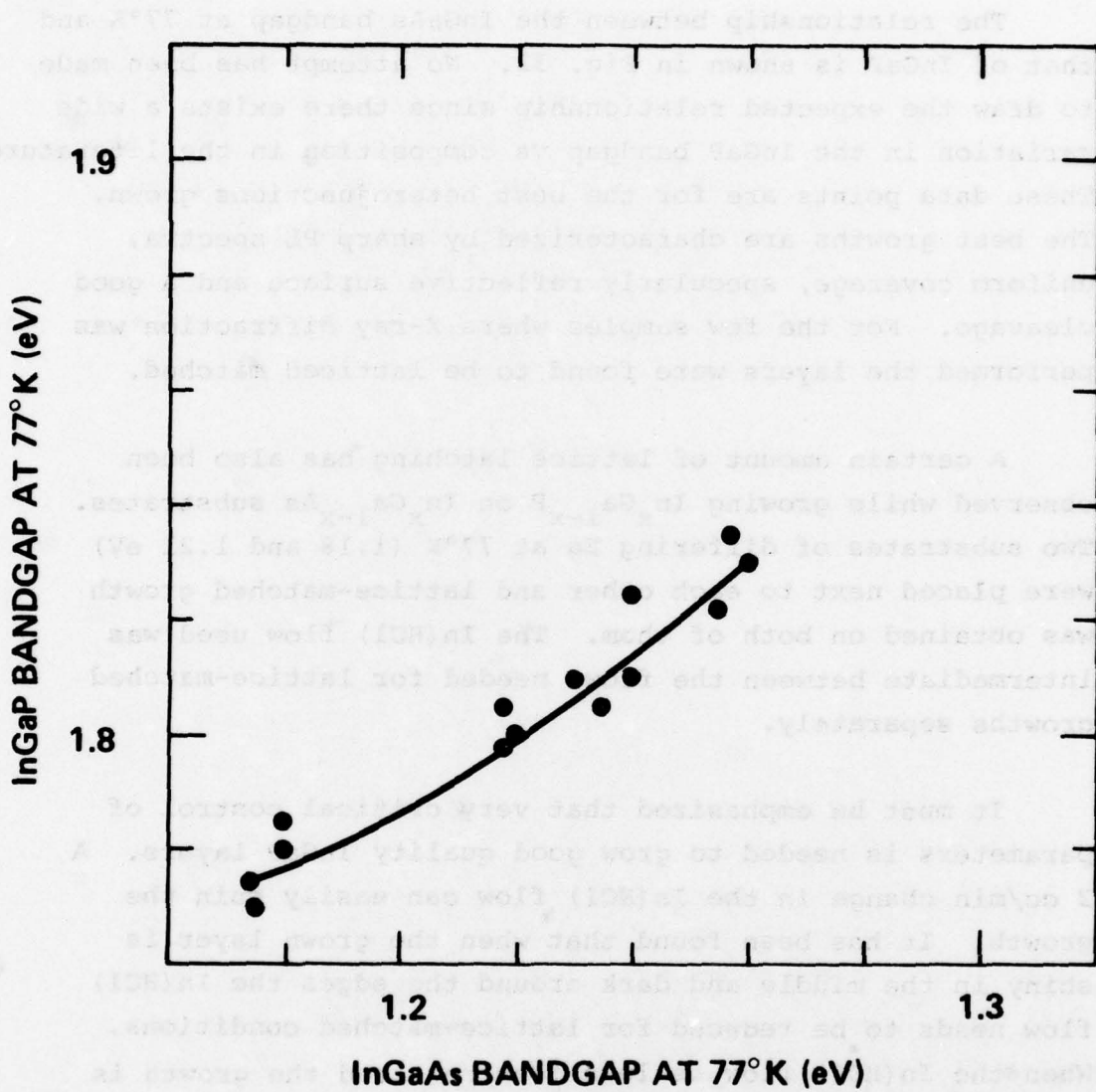


Fig. 32. Measured relationship between InGaP bandgap and InGaAs bandgap (both at 77°K) for InGaP/InGaAs/GaAs samples.

size. For unequal sources these conditions are not appropriate and lattice-matched growth is not obtained. Also for equal sources but with substantially different surface area the conditions would have to be adjusted slightly.

The $\text{In}_x\text{Ga}_{1-x}\text{P}$ layers lattice matched to $\text{In}_x\text{Ga}_{1-x}\text{As}$ substrates are shiny in appearance and the surface has a characteristic cross-hatch pattern as shown in Fig. 33. The asymmetry in the pattern follows from the asymmetry in the zinc blend structure as discussed by Olsen et al.⁵⁶ The surface of the InGaP lattice matched to GaAs has no cross-hatch as shown in Fig. 34. Similar findings have been reported earlier when $\text{In}_x\text{Ga}_{1-x}\text{P}$ graded on GaP was found to have a cross-hatch pattern on the surface while InGaP grown directly on GaAs showed no cross-hatch at all.⁵⁷ Thus, the cross-hatch seen on the $\text{In}_x\text{Ga}_{1-x}\text{P}$ surface when grown on graded $\text{In}_x\text{Ga}_{1-x}\text{As}$ substrate is due to the substrate itself. This is clearly seen in Fig. 35, which shows both the cross-hatch patterns in a wafer where the $\text{In}_x\text{Ga}_{1-x}\text{P}$ did not grow in a few localized regions.

Lattice matched $\text{In}_x\text{Ga}_{1-x}\text{P}/\text{In}_x\text{Ga}_{1-x}\text{As}$ growths are found to cleave easily without cracking and show a sharp interface, whereas mismatched layers are difficult to cleave. Cracking on cleavage of imperfect layers has also been reported earlier.⁴⁷ A cleaved picture of the InGaP/InGaAs/GaAs structure is shown in Fig. 36.

Sharp PL spectra are obtained from lattice-matched $\text{In}_x\text{Ga}_{1-x}\text{P}/\text{In}_x\text{Ga}_{1-x}\text{As}$ layers as shown in Fig. 37; for mismatched layers the PL spectrum is very broad. Sharp PL spectra are also indicative of compositional homogeneity since the half-width is known to increase with compositional inhomogeneity.⁵⁸

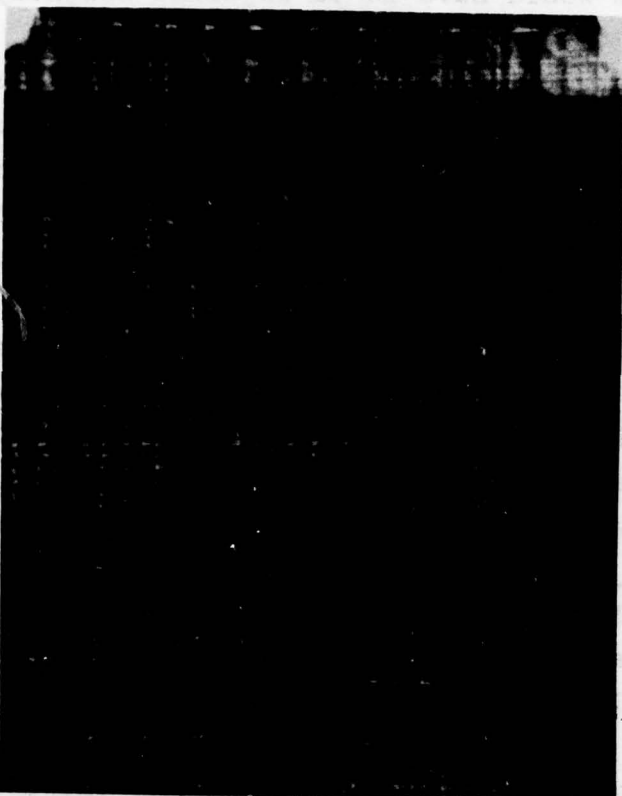


Figure 33. Photomicrograph of the surface of InGaP/InGaAs/GaAs sample #SR 3-28, magnification 291X.



30 position 103 to decompared to 21 sample
31-2 new sample 3331-3332
2000 3333-3334
3335 included in 3336

Figure 34. Photomicrograph of InGaP/GaAs
sample #SR 3-12, magnification 291X.

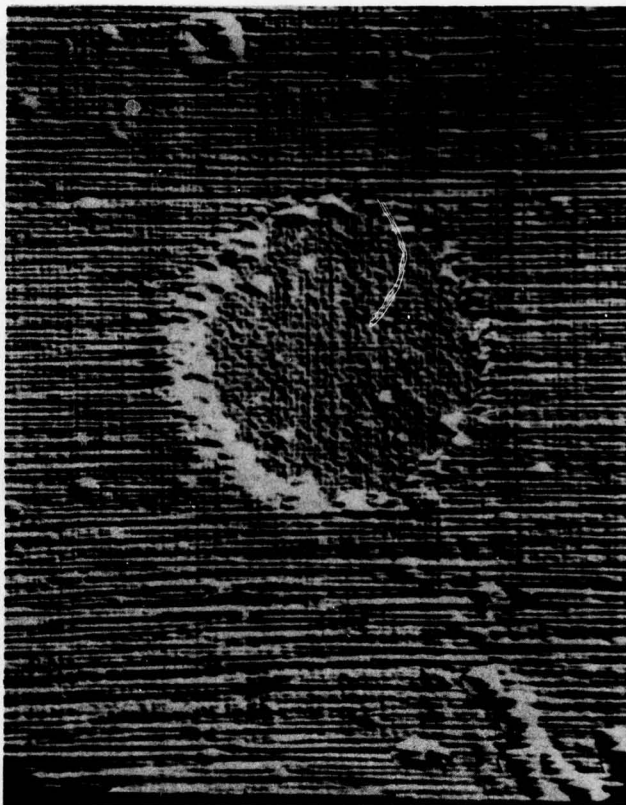


Figure 35. Photomicrograph of the surface of InGaP/InGaAs/GaAs sample #SR 5-18, magnification 110X. InGaP did not grow in circular area.

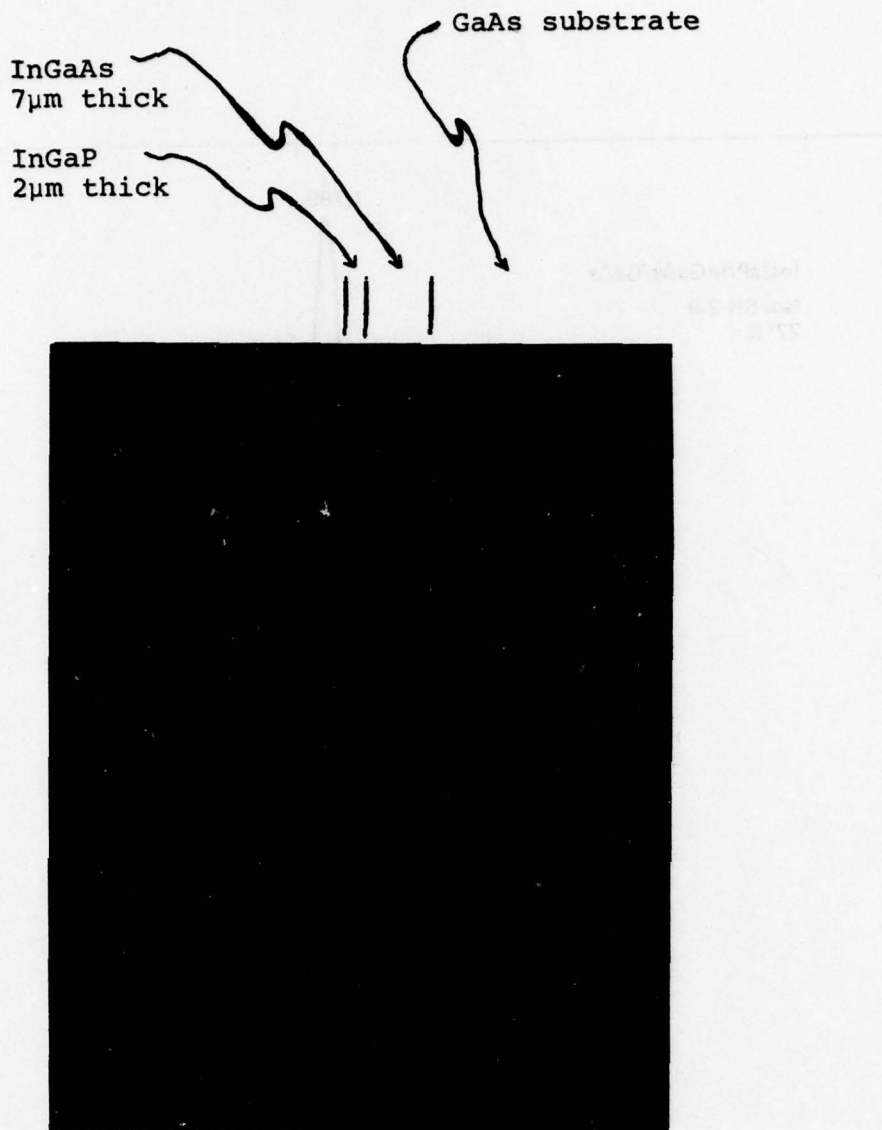


Figure 36. Cleaved section of sample #SR 2-12,
magnification 1402X.

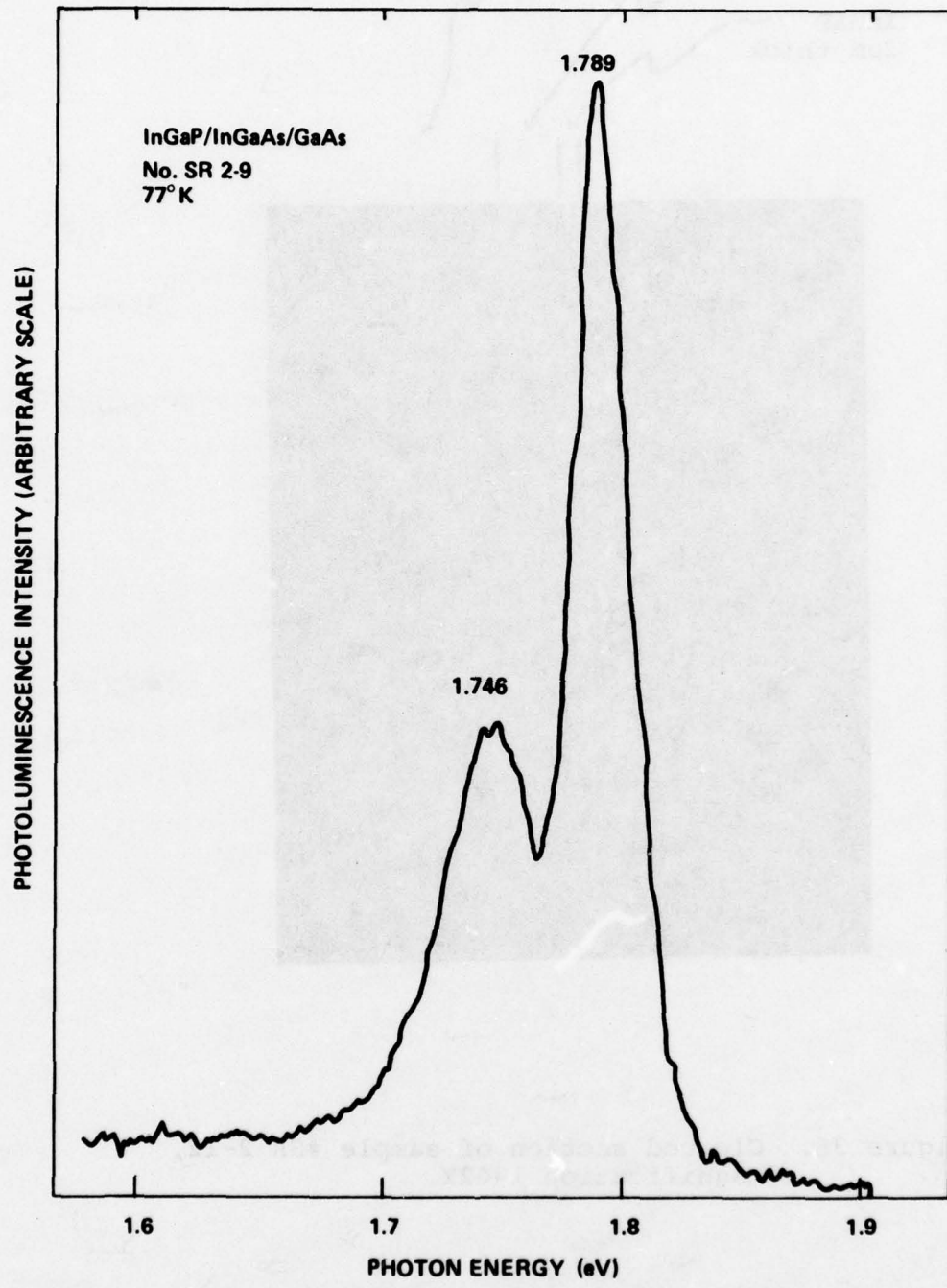


Fig. 37. Photoluminescence spectrum for InGaP/InGaAs/GaAs sample #SR2-9.

To obtain different p-type doping levels the Zn heater temperature is varied while the H_2 flow is kept fixed at 50 cc/min. The doping levels were usually determined by C-V measurements. The doping levels achieved in the $In_xGa_{1-x}P$ layers for various Zn pellet temperatures are shown in Fig. 38. The PL spectra for p-InGaP have a distinct Zn peak and the ionization energy measured is a function of doping itself. This relationship is also shown in Fig. 38. The ionization energy is a slow function of the In_x as well but the doping level effects dominate in Fig. 12 since the data are for $In_xGa_{1-x}P$ layers with $x=0.62 \pm .02$ only.^{50,59}

Van der Pauw measurements of InGaP were somewhat difficult to make due to contacting problems associated with a high-bandgap material. For $In_xGa_{1-x}P$ lattice matched to GaAs, a mobility of $104 \text{ cm}^2/\text{Vsec}$ was measured at room temperature for a carrier concentration of $8.4 \cdot 10^{15} \text{ cm}^{-3}$. Typical growth rate for InGaP is $0.1 \mu/\text{min}$.

With the slider boat arrangement sharp interfaces have been obtained. The sputtered Auger analysis of one sample is shown in Fig. 39. The interface is seen to be only $\sim 100 \text{ \AA}$ thick.

Conclusion: Growth parameters have been established for growing InGaP lattice matched to InGaAs. The problems associated have been discussed in detail. To improve the reproducibility of the results, it would be beneficial to design a source region such that the surface area exposed and the residence time of gases over the sources are kept as nearly constant as possible. For better resolution in controlling the InGaP composition the flows should all be increased, since with 2 cc/min flow over the Ga source even 1 cc/min change in the In(HCl) flow makes a difference. Although we have grown on a temperature slope of $5^\circ\text{C}/\text{cm}$ this causes

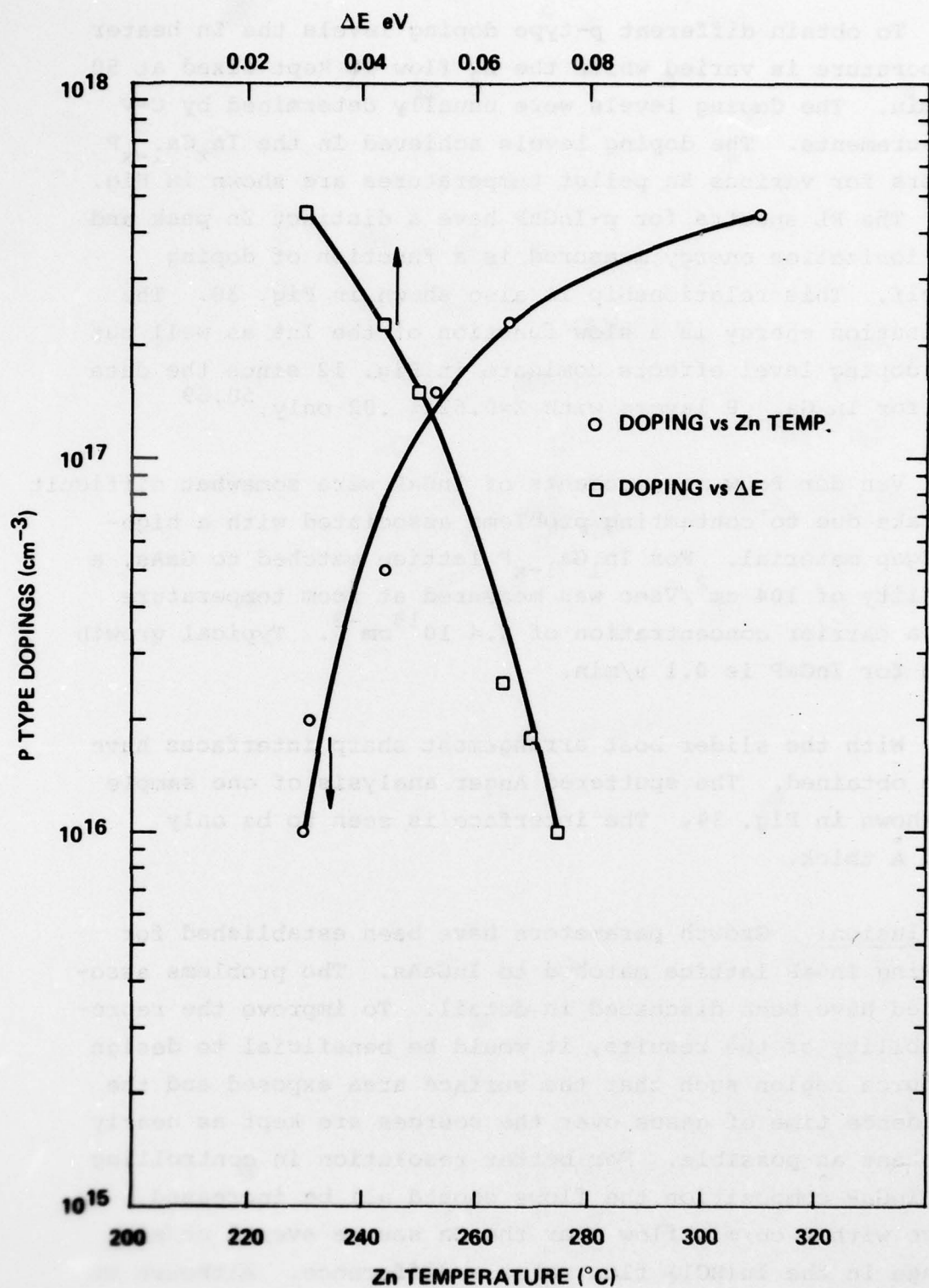


Fig. 38. InGaP p-type doping level vs Zn source temperature and vs Zn ionization energy determined from photoluminescence measurements.

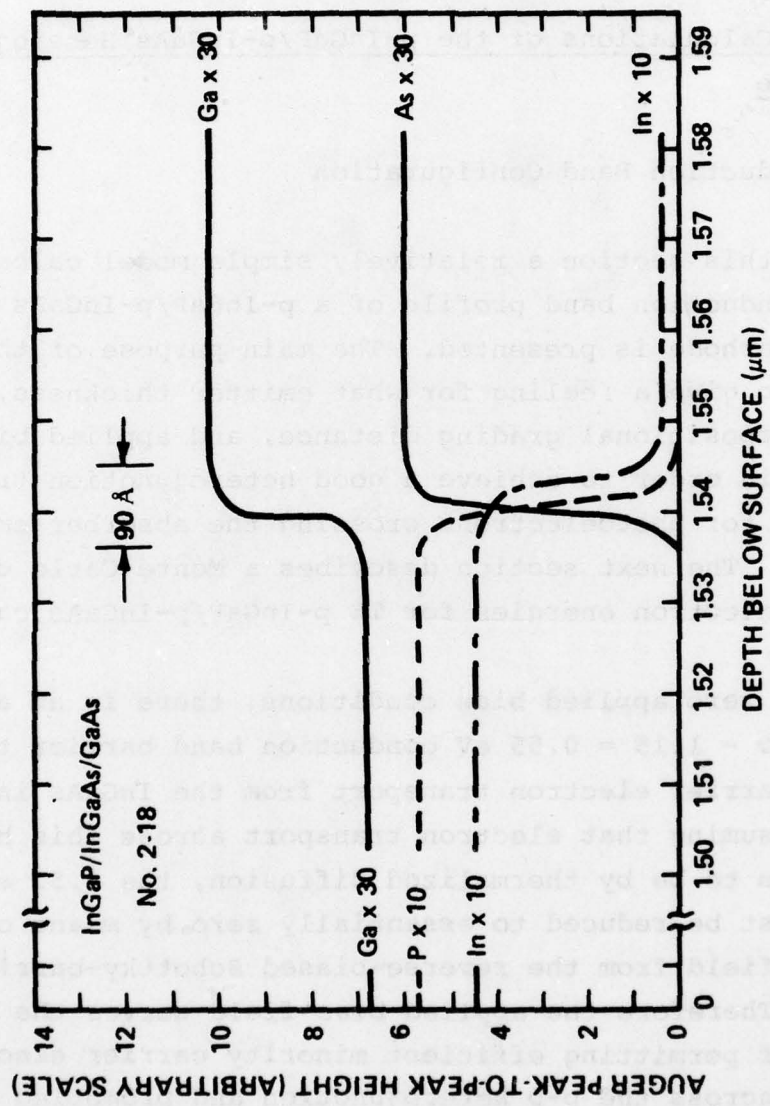


Fig. 39. Auger sputter depth profile through a InGaP/InGaAs heterojunction.

problems in obtaining uniform growth over a large area wafer. Attempts to grow InGaP on 1/2" diameter wafer were not too successful. It would be worthwhile to adjust the temperature profile such that growth could take place on a flat temperature region.

3.4 Model Calculations of the p-InGaP/p-InGaAs Heterojunction Cathode

3.4.1 Conduction Band Configuration

In this section a relatively simple model calculation for the conduction band profile of a p-InGaP/p-InGaAs heterojunction cathode is presented. The main purpose of the model is to give a feeling for what emitter thickness, doping, compositional grading distance, and applied bias are necessary in order to achieve a good heterojunction transfer efficiency for photoelectrons crossing the absorber-emitter interface. The next section describes a Monte Carlo calculation of electron energies for TE p-InGaP/p-InGaAs cathodes.

Under zero applied bias conditions, there is an approximately $1.70 - 1.15 = 0.55$ eV conduction band barrier to minority carrier electron transport from the InGaAs into the InGaP. Assuming that electron transport across this heterojunction is to be by thermalized diffusion, the 0.55 eV barrier must be reduced to essentially zero by means of the depletion field from the reverse-biased Schottky-barrier contact. Therefore the applied bias field serves the dual function of permitting efficient minority carrier electron transport across the p-p heterojunction and promoting efficient electron transfer into the upper valleys within the emitter.

A comment should be made at this point in regard to exactly how to line up the band edges at the interface. By far the most commonly discussed model for how the energy bands at a heterojunction align themselves is that proposed by Anderson⁶¹ in 1962. If ΔE_g , ΔE_c , and ΔE_v represent band-gap, conduction band, and valence band differences between two semiconductors, the Anderson model assumes that $\Delta E_c + \Delta E_v = \Delta E_g$ and $\Delta E_c = \Delta x$, where Δx is the difference in electron affinities of the two semiconductors. An extensive literature has evolved over the years based on this model.^{62,63} For the heterojunction TE cathode, ΔE_c is of importance since, in principle, it represents an additional potential barrier to electron heterojunction transfer. In virtually all practical cases, however, the type of band discontinuity predicted by the Anderson model or any of the other more current models⁶⁴ can be ignored. The reason for this is that under typical VPE or LPE growth conditions, there is a finite region over which the composition is graded. The interface is not an abrupt transition step but rather a compositionally graded region on the order of 1000 Å or more.⁶⁵ The net effect of this grading region is to smooth out the predicted ΔE_c discontinuity at the heterojunction interface. The work of Oldham and Milnes⁶⁶ and Cheung et al.⁶⁷ discusses this point in more detail. The predicted heterojunction discontinuity barriers may only be observable experimentally in extremely abrupt heterojunctions such as those produced by molecular beam epitaxy⁶⁸ or by special LPE or VPE growth techniques.⁶⁹

The first part of the model to be discussed is the grading function, $G(X)$. The grading function is taken to be a simple mathematical function describing the bandgap variation over the heterojunction transition region. The simplest function would be linear grading function of the form $G(X) \sim E_g(L-x)/L$. However, a physically more attrac-

tive function is the hyperbolic tangent which has been employed by others for this purpose.^{66,67} The grading function is then given by

$$G(X) = E_g(\text{InGaAs}) + \left(\frac{\Delta E_g}{2} \right) \left[1 - \tanh \frac{X - T(\text{InGaP}) - L/2}{L} \right]$$

where $T(\text{InGaP})$ is the p-InGaP emitter thickness, L is an effective bandgap grading distance, and X is the distance from the emitter-vacuum interface. Note that L in this case is approximately half the distance over which the bands vary from 10-12% to 90-88% of maximum change, ΔE_g .

To complete the model, a Schottky-barrier surface contact is assumed on the p-InGaP surface, i.e. $X = 0$. The spatial potential variation, $V(X)$, due to an applied bias, V_{bias} , is given by

$$V(X) = \frac{qN_a}{\epsilon} \left(W(V_{\text{bias}}) \cdot X - \frac{1}{2} X^2 \right) - Q_B + V_{\text{bias}}$$

where q is the electronic charge, ϵ the relative dielectric constant of the emitter, Q_B the p-Schottky-barrier height, and N_a the acceptor doping concentration. $W(V_{\text{bias}})$ is the depletion width which is given by⁷⁰

$$W(V_{\text{bias}}) = \left(\frac{2\epsilon}{qN_a} \left(V_{\text{bi}} - V_{\text{bias}} - \frac{K_B T}{q} \right) \right)^{1/2}$$

where K_B is the Boltzmann constant, T the absolute temperature, and V_{bi} is the amount of band bending at the surface. V_{bi} is Q_B minus the Fermi level height, F , above the valence band maximum in the bulk. As the depletion field sweeps back from the emitting surface into the absorber, the initial 0.55 eV conduction band barrier is pulled down. The bands in the InGaAs also begin to be pulled down. The model calculates $V(X)$ in the InGaAs using the same formula as that

shown above but using materials parameters appropriate for InGaAs and an effective Schottky-barrier height based on how much the InGaAs bands are pulled down at the InGaP/ InGaAs interface due to the depletion field from the surface Schottky-barrier contact.

The complete model for the conduction band variation (relative to the bulk Fermi level) vs X is simply $G(X) + V(X)$. Several sample calculations for the p-InGaP/p-InGaAs heterojunction cathode have been performed and are shown in Figs. 40-45. In Figs. 40-43, all cathode parameters are held constant, except the grading length, L , which is raised from 100 Å in Fig. 40 to 2000 Å in Fig. 43. In Figs. 44 and 45, the parameters are the same as in Fig. 43 except that the InGaAs absorber doping is increased from $1 \times 10^{15} \text{ cm}^{-3}$ in Fig. 43, to $1 \times 10^{16} \text{ cm}^{-3}$ in Fig. 44 and $1 \times 10^{17} \text{ cm}^{-3}$ in Fig. 45. It is clear in Figs. 40, 41 and even 42 that thermalized electron transport from the InGaAs into the InGaP would be poor for short grading distances. As the heterojunction grading distance, L , becomes longer and longer the initially rather sharp band discontinuity begins to smooth out and essentially vanishes for the case of Fig. 43 and $V_{\text{bias}} > 3$ volts. Figure 44 indicates that increasing the doping in the InGaAs absorber to $1 \times 10^{16} / \text{cm}^3$ would not cause heterojunction problems, however Fig. 45 shows that $1 \times 10^{17} / \text{cm}^3$ would be a problem. Additional calculations indicate that the emitter should be 0.5 to 1.0 micron thick for an emitter doping of $1-5 \times 10^{15} / \text{cm}^3$. A much thinner emitter is needed if the emitter doping rises much above $1 \times 10^{16} / \text{cm}^3$. A compositional grading distance on the order of 1000 Å or more is essential for thermalized electron transport across the p-p heterojunction.

Another feature of the model is that it takes the derivative of the potential, $V(X)$, thereby generating the

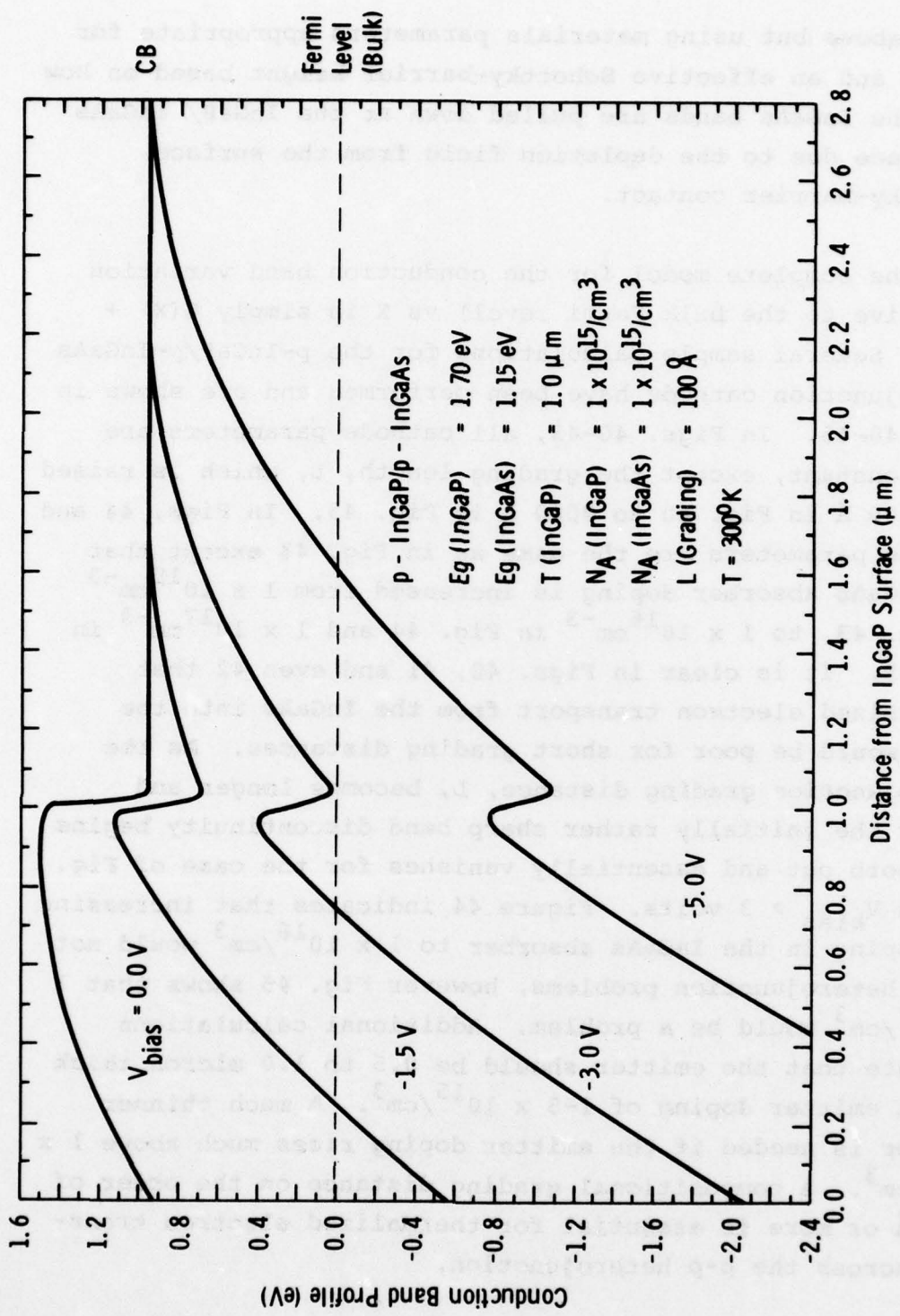


Fig. 40. Calculated conduction band profile for an InGaP/InGaAs heterojunction TE cathode.

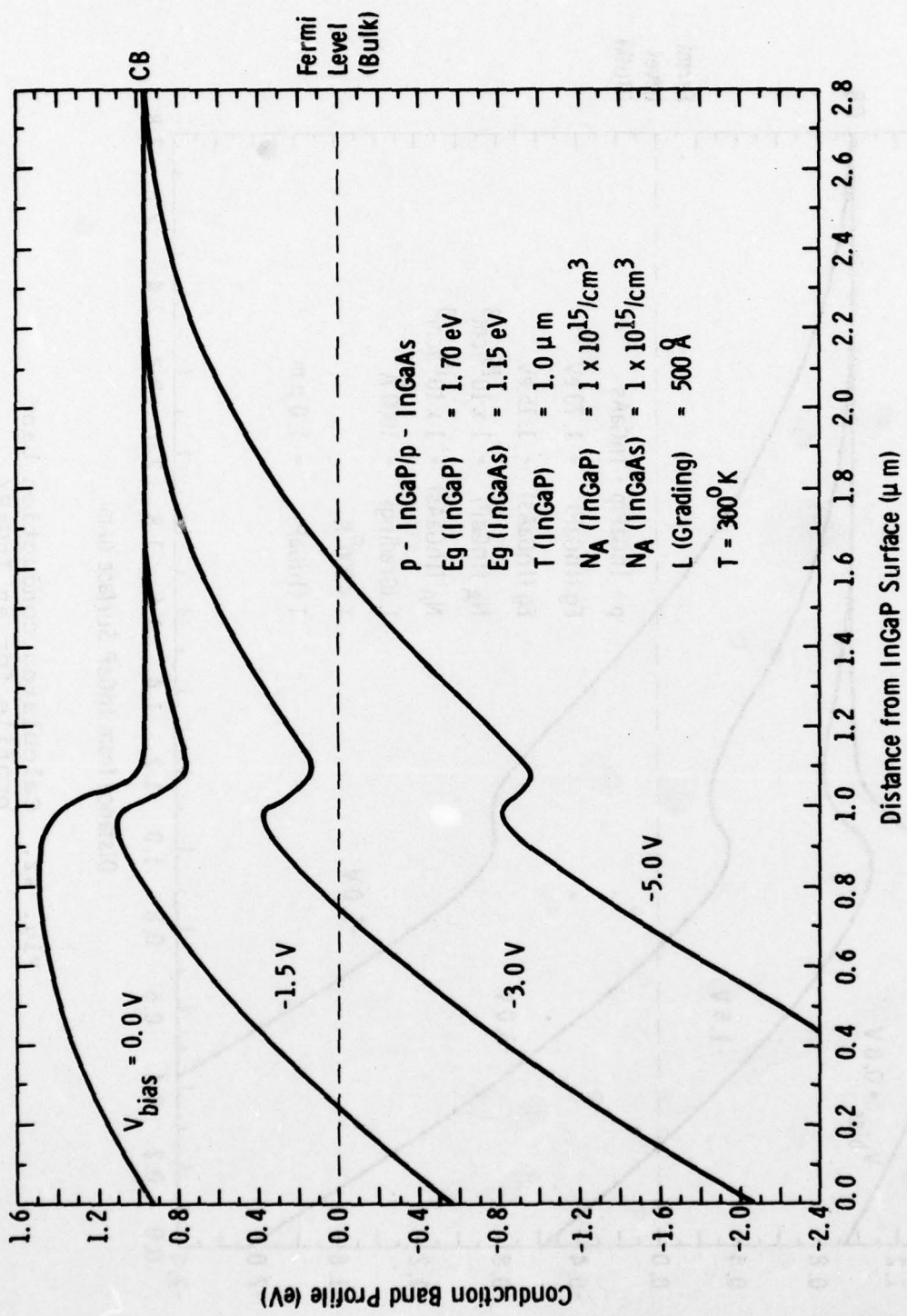


Fig. 41. Calculated conduction band profile for an InGaP/InGaAs heterojunction TE cathode.

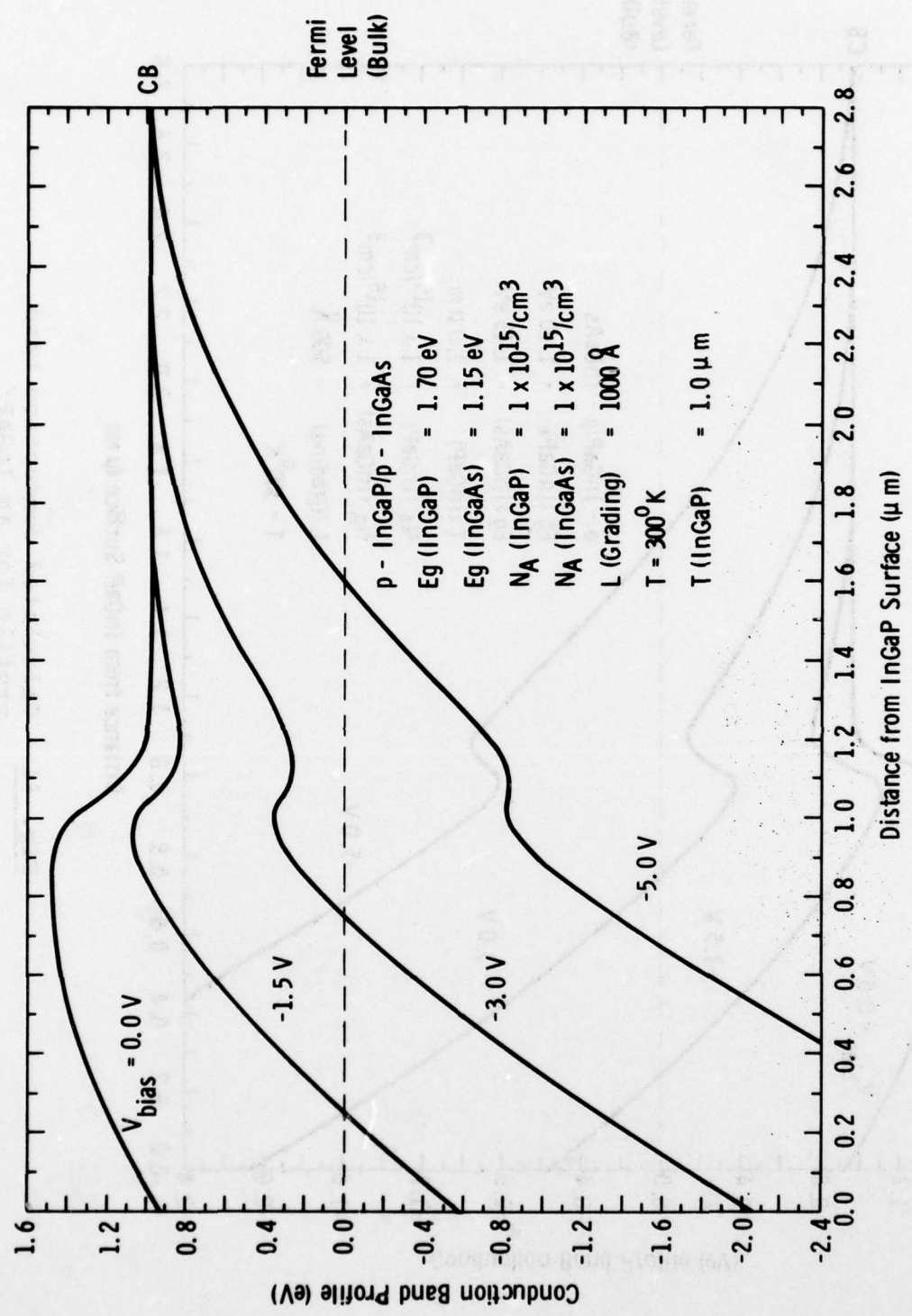


Fig. 42. Calculated conduction band profile for an InGaP/InGaAs heterojunction TE cathode.

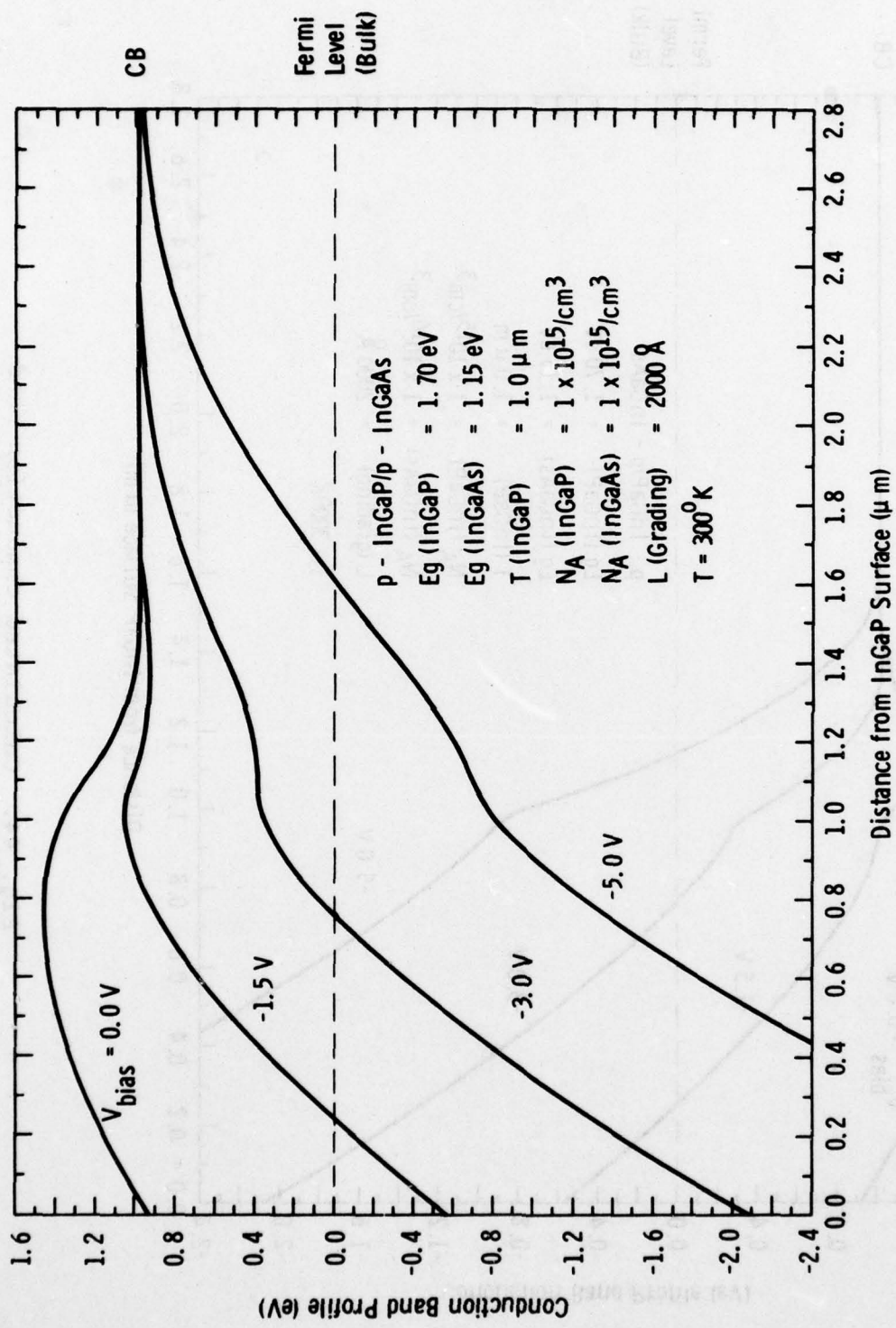


Fig. 43. Calculated conduction band profile for an InGaP/InGaAs heterojunction TE cathode.

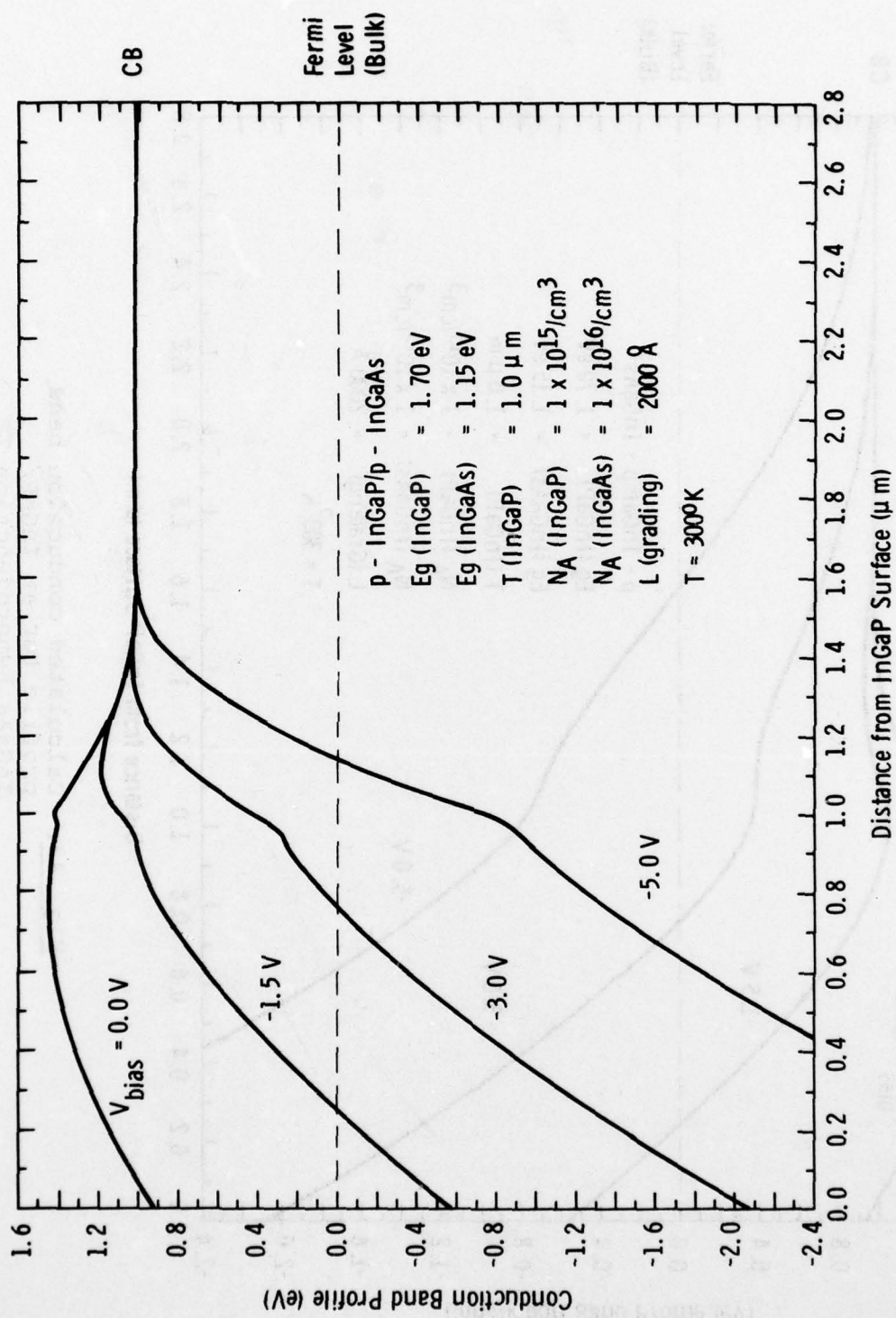


Fig. 44. Calculated conduction band profile for an InGaP/InGaAs heterojunction TE cathode.

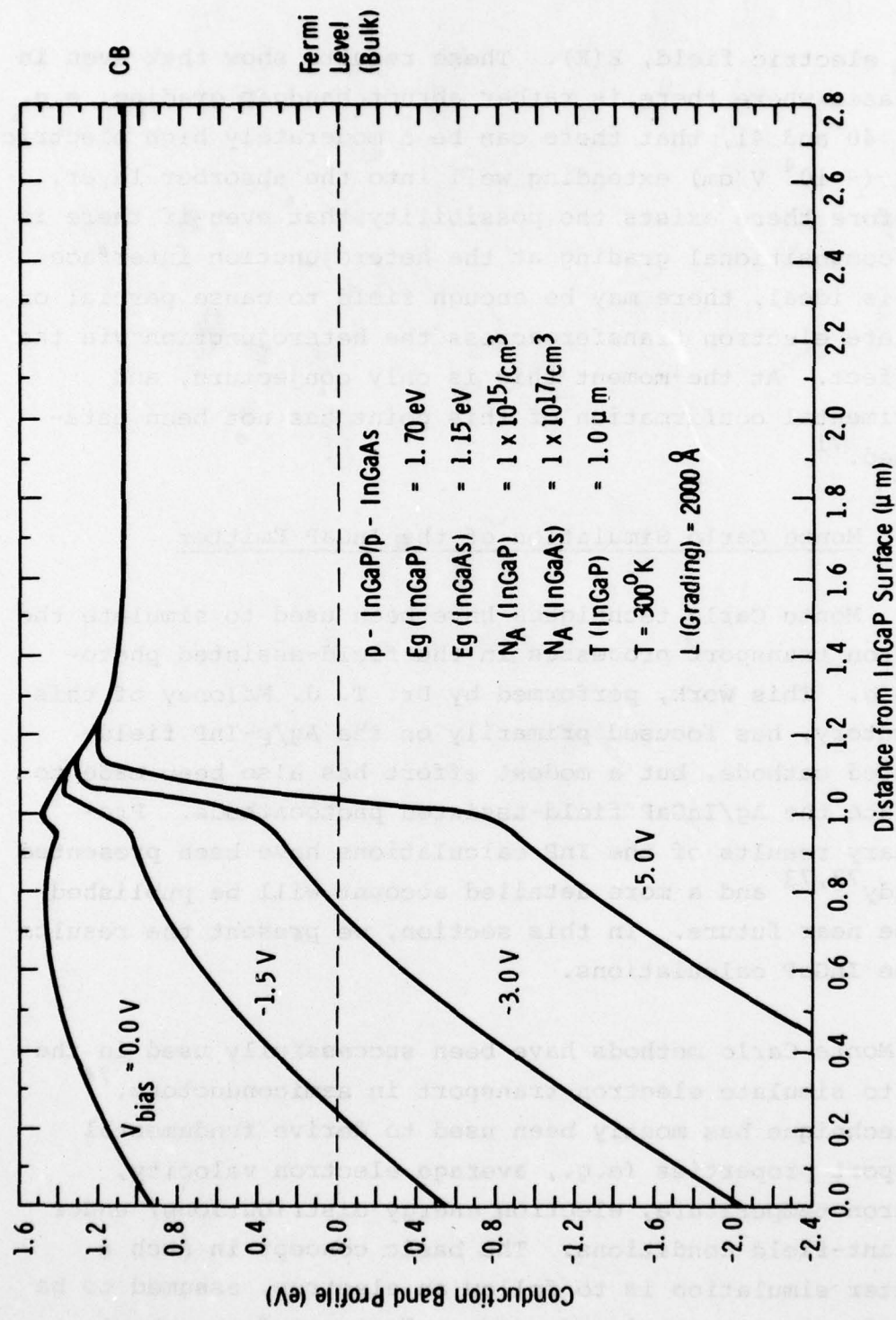


Fig. 45. Calculated conduction band profile for an InGaP/InGaAs heterojunction TE cathode.

local electric field, $E(X)$. These results show that even in the cases where there is rather abrupt bandgap grading, e.g. Figs. 40 and 41, that there can be a moderately high electric field ($\sim 10^4$ V/cm) extending well into the absorber layer. Therefore there exists the possibility that even if there is less compositional grading at the heterojunction interface than is ideal, there may be enough field to cause partial or complete electron transfer across the heterojunction via the TE effect. At the moment this is only conjecture, and experimental confirmation of this point has not been established.⁷¹

3.4.2 Monte Carlo Simulation of the InGaP Emitter

Monte Carlo techniques have been used to simulate the electron transport processes in the field-assisted photocathode. This work, performed by Dr. T. J. Maloney of this laboratory, has focused primarily on the Ag/p-InP field-assisted cathode, but a modest effort has also been made to simulate the Ag/InGaP field-assisted photocathode. Preliminary results of the InP calculations have been presented already^{72,73} and a more detailed account will be published in the near future. In this section, we present the results of the InGaP calculations.

Monte Carlo methods have been successfully used in the past to simulate electron transport in semiconductors.⁷⁴ The technique has mostly been used to derive fundamental transport properties (e.g., average electron velocity, electron temperature, electron energy distributions) under constant-field conditions. The basic concept in such a computer simulation is to follow an electron, assumed to be typical, for a long time (or many electrons for a short time) in the solid, allowing it to be accelerated by the

electric field, scattered by impurities and by the various phonons, transferred among the conduction valleys, and so on. Random numbers are used to select the time of flight between scattering events, the scattering process for a particular event, and the final state of the electron after the event, so that the behavior of a typical electron is simulated. By averaging the appropriate quantities over the total flight time one can derive such things as average velocity, energy and k -space histograms, electron temperature, and the startup transient (velocity vs time or distance) of electrons in a suddenly-applied field.

Although most Monte Carlo work on electron transport has been for simple constant-field conditions, it is in principle possible to use the technique to simulate a real electronic device complete with nonuniform fields and even, if necessary, time dependence. Such efforts are likely to be frustrating and expensive if the device is, say, a field effect transistor with time dependent electric fields influenced by internal space charge.⁷⁵ However, the field-assisted photocathode lends itself particularly well to Monte Carlo simulation because time dependence is negligible and because the electron charge densities (set up by low light levels) are too low to influence the linearly graded electric field produced by the reverse bias on the Schottky-barrier. In the Monte Carlo model for the photocathode, electrons are generated in the bulk with a spatial distribution appropriate to the optical absorption coefficient for the chosen photon energy. The latter also determines the initial energy of the electron. When the electrons reach the semiconductor surface, the program takes note of the electron's energy, k -vector, and conduction band, then records this information before generating another electron in the bulk. The Monte Carlo simulation produces a profile of the electrons reaching the surface that helps predict the performance of a photocathode.

AD-A073 224

VARIAN ASSOCIATES INC PALO ALTO CA
1.06-MICRON III-V PHOTOCATHODE DEVELOPMENT. (U)

MAY 79 J S ESCHER, P E GREGORY, S B HYDER

F/6 9/1

F33615-76-C-1351

NL

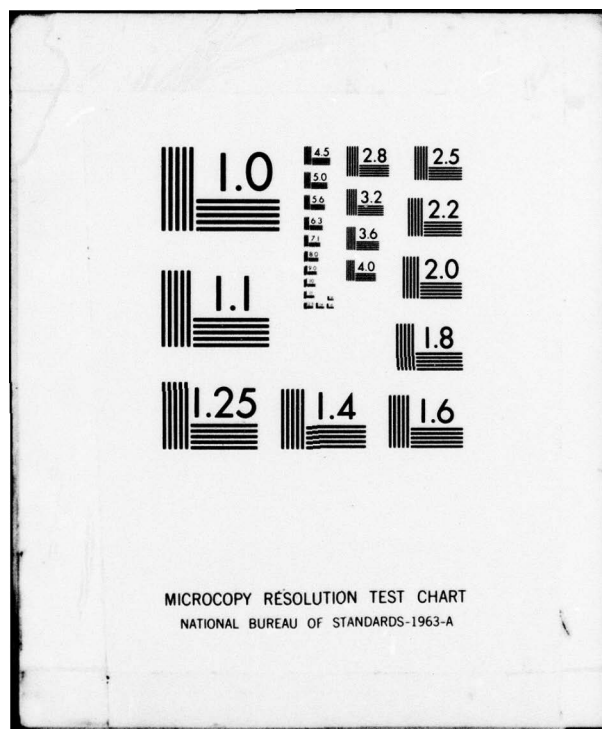
UNCLASSIFIED

AFAL-TR-79-1039

2 OF 2
AD
A073224



END
DATE
FILMED
9-79
DDC



The emphasis in the calculations has been on studying the effects of applied bias and emitter doping on the energy distribution of photogenerated electrons. Figure 46 shows the average electron energy in the T, X, and L bands of an InGaP emitter vs InGaP doping for a 5-volt bias, an InGaP bandgap of 1.7 eV, and a photon energy of 1.8 eV. Note that the energies are plotted versus the zero of energy in each band. The band profile assumed for the InGaP emitter is shown in Fig. 47. For the 1.7 eV bandgap, 1.1 eV work function, and 0.7 eV Schottky-barrier height shown in Fig. 47, the Γ minimum is 0.1 eV below the vacuum level. Thus any Γ electrons with energy >0.1 eV can escape. Referring to Fig. 46, we see that even for dopings of 10^{15} cm^{-3} the average Γ electron has enough energy to escape for the assumed 5-volt bias. For higher dopings the average electron energy increases in all three bands, as would be expected since the electric field increases with doping.

Although we have not yet attempted to measure the energy distribution of electrons emitted from a field-assisted photocathode, one experimental observation strongly suggests that some of the emitted electrons are quite hot. For many cathodes, with InP, InGaP, or InGaAsP emitters, field-assisted photoemission is often seen with a Cs-only activation, although not with as high a quantum efficiency as with Cs + O activations. The work function of the Ag is usually ~ 1.6 -1.7 eV for a Cs-only activation, and 1.0-1.2 eV for a Cs+O activation. Thus some electrons have at least ~ 0.5 eV more energy than they need to escape the Cs+O activated surface.

If the emitted electrons are indeed fairly hot, this fact would have important implications for stability of the field-assisted photocathodes. The NEA 1.06-micron photocathode, in its present state of development, requires cooling for

$\phi = 0.70 \text{ eV}$, $a = 1.3/\mu\text{m}$, $E_g \approx 1.7 \text{ eV}$
 $\Gamma \cdot L = 0.43 \text{ eV}$ $\hbar\nu = 1.8 \text{ eV}$
 $\Gamma \cdot X = 0.46 \text{ eV}$

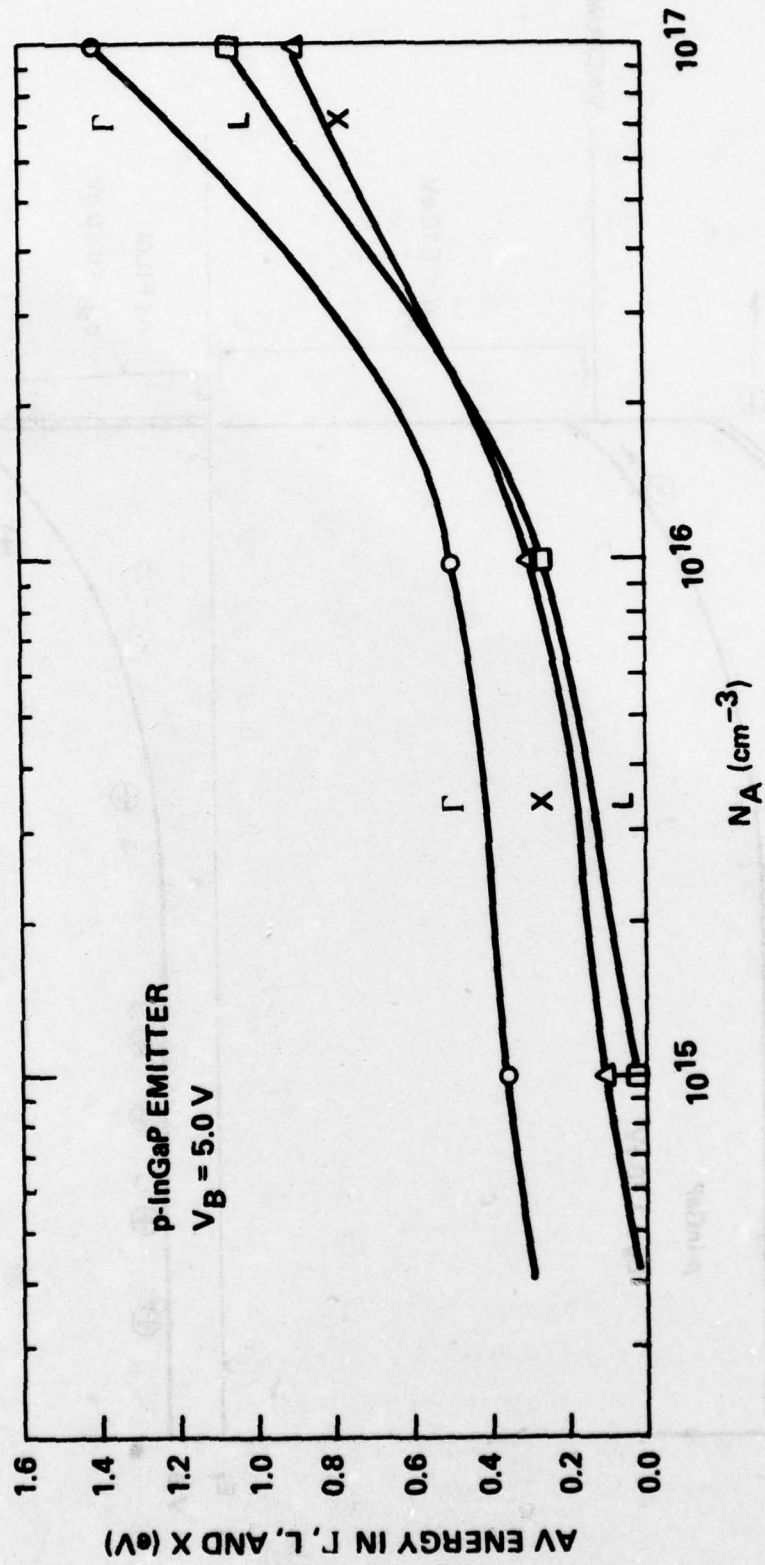


Fig. 46. Average electron energy in conduction bands of InGaP emitter as a function of InGaP doping, as calculated from Monte Carlo simulation.

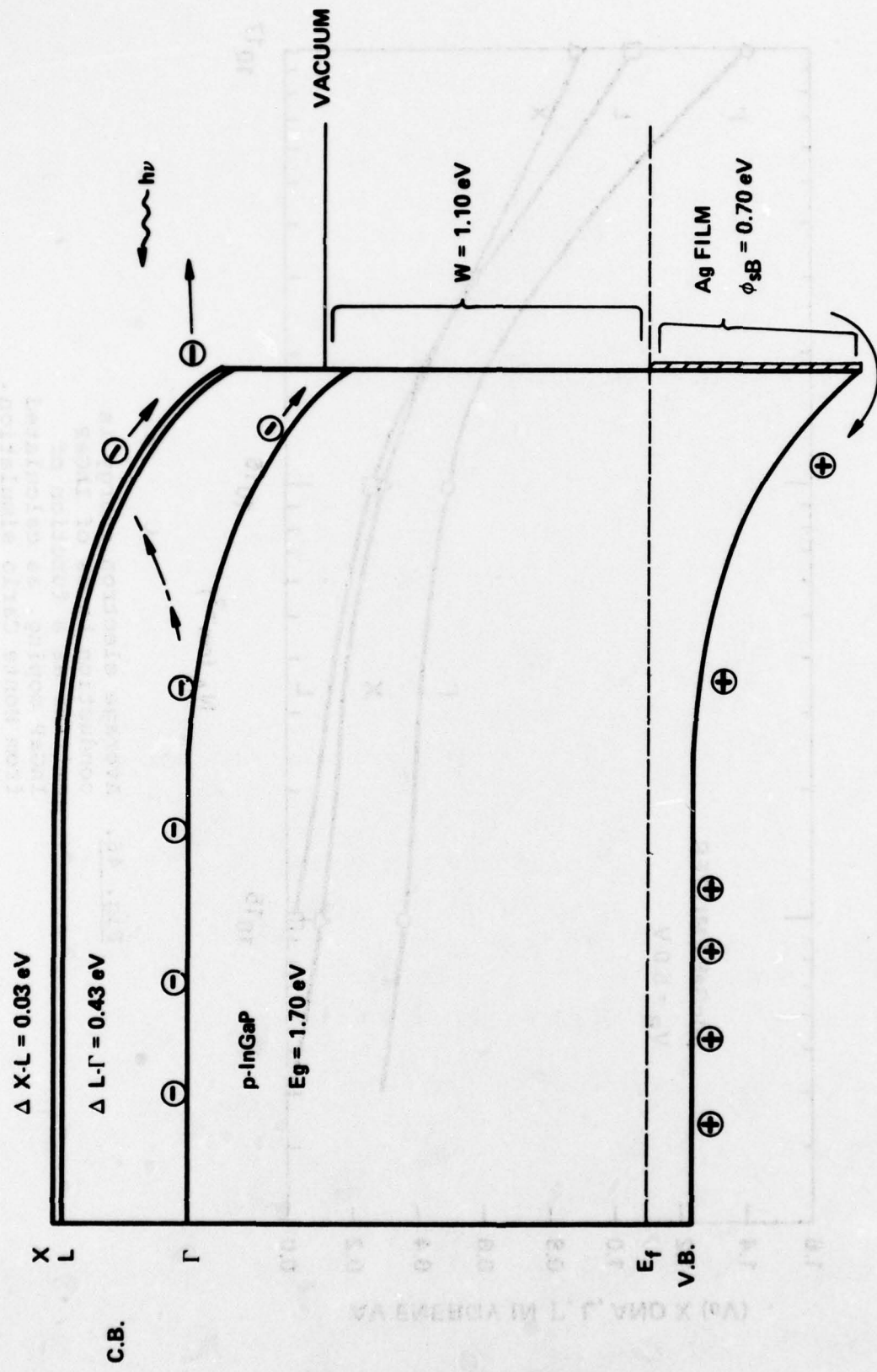


Fig. 47. InGaP band spacings and profile assumed for the Monte Carlo simulation.

long-term stability.^{76,77} Apparently the emitted electrons have just barely enough energy to surmount the energy barrier at the surface of the NEA 1.06-micron photocathode; any small change in the Cs+0 activating layer which increases the energy barrier drastically reduces the number of electrons which can escape from the cathode. On the other hand, if the electrons escaping the field-assisted photocathode are fairly hot, small increases in the Ag work function would have only a small effect on the number of electrons able to escape. Thus the field-assisted photocathode would be expected to have less of a long-term stability problem than that of the 1.06-micron NEA cathode.

Figure 48 shows the percent of electrons in each conduction band as a function of doping, for the same conditions as for Fig. 46. As is expected, more electrons transfer to the higher bands with higher doping, again because of the higher electric field.

The Monte Carlo simulation gives electron energy distributions at the InGaP/Ag interface; to complete a model of the photocathode it would be necessary to include transport through the Ag film and escape into the vacuum. These additional features represent very difficult theoretical problems that are beyond the scope of the work under this contract. Thus no attempt has been made to include these additional features in the Monte Carlo model. Even without considering electron escape, the Monte Carlo model results are useful in understanding the operation of the field-assisted photocathode.

3.5 Direct Emitter Photoemission Results from p-InGaAsP

Before discussing the vacuum photoemission results a few comments should be made in regard to cathode preparation,

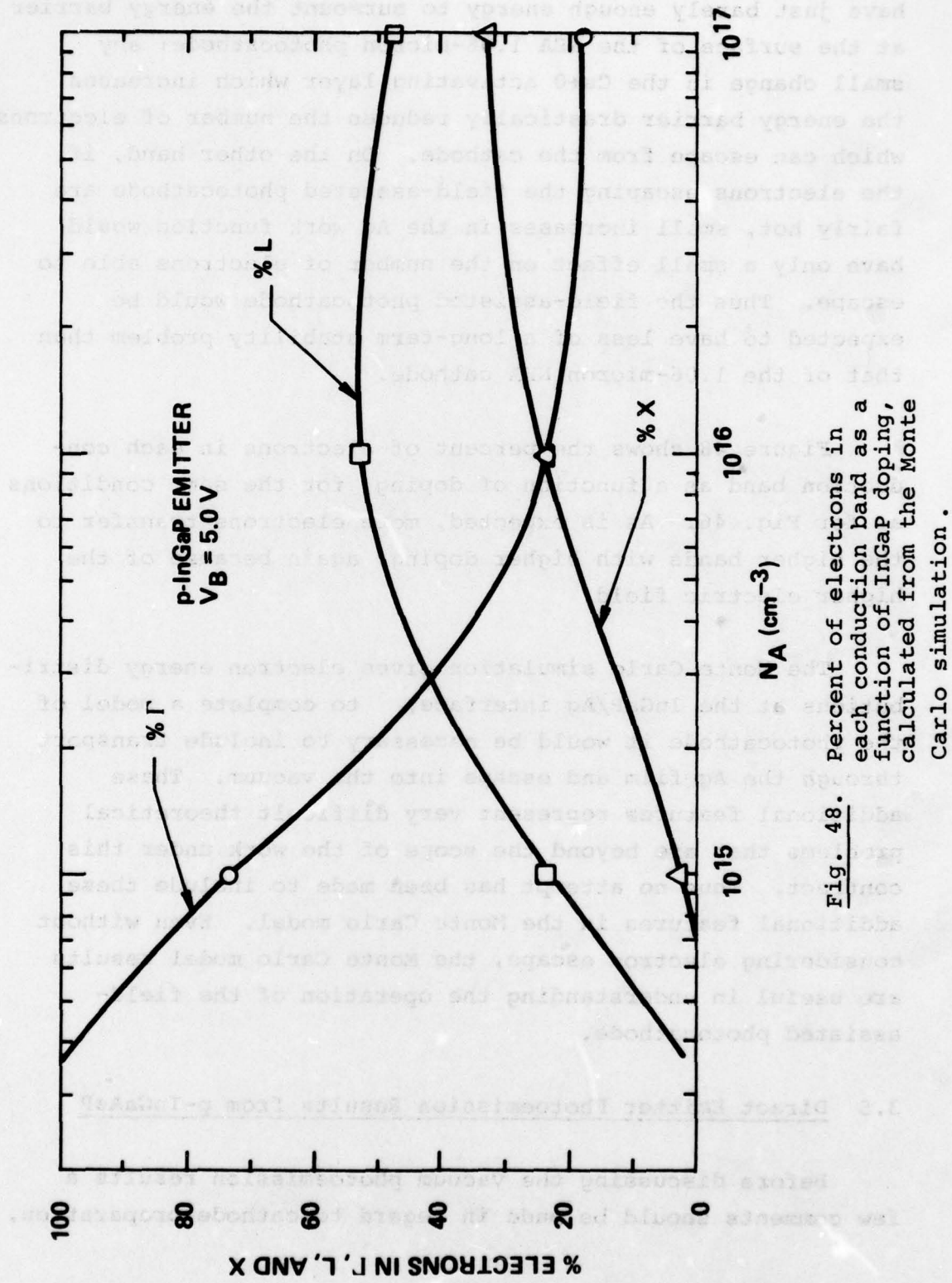


Fig. 48. Percent of electrons in each conduction band as a function of InGaP doping, calculated from the Monte Carlo simulation.

vacuum processing, Schottky-barrier evaporation, and Cs-0 activation procedure. It is well known that surface carbon contamination is a serious obstacle to achieving high performance NEA (and presumably TE) cathodes. Once the cathode is removed from the growth system the emitting surface is exposed to various atmospheric gases and pollutants until the time comes for it to be vacuum processed. The ideal situation is for the cathode to be grown and immediately transferred into the vacuum system without delay. The hybrid cathode discussed in detail in Sec. 3.6 was handled in this fashion. The next best interim procedure would probably be storage in UHV. For longer-term storage, a week or more, a nitrogen dry box is used. Just prior to transfer into vacuum the cathode is given a chemical cleaning procedure consisting of hot solvent baths, 4:1:1 (sulfuric acid, hydrogen peroxide, and water), and dilute bromine methanol etches. An alternative chemical cleaning procedure is to use the hot solvents, and then to immerse the cathode in hot (nearly boiling) de-ionized H_2O for 5-10 minutes, followed by blowing it dry with dry N_2 gas. Based on Auger measurements of the surface cleanliness of the cathode, the technique using H_2O seems to work as well as the technique using 4:1:1 and bromine methanol. The chemical cleaning procedure helps remove the surface contaminants built up during storage in the dry box. The direct emitter cathodes discussed in this section and several of the InGaP emitter cathodes were stored in a N_2 dry box from a few days to several weeks prior to chemical cleaning and vacuum testing.

After chemical cleaning and immediate transfer into the vacuum system the cathode surface is further cleaned. The procedure used for all the cathodes discussed in this report consisted of heat cleaning in vacuum to near the cathode surface decomposition temperature and then cooling to room temperature. No sputtering techniques were used. Ion

sputtering is a common technique for surface cleaning, especially for carbon contaminated surfaces. However it has not been demonstrated to be a superior technique to simple vacuum heat cleaning for the NEA III-V photocathodes, provided that the cathode was not badly contaminated prior to the vacuum cleaning procedure. An Auger electron spectrometer was found to be essential in setting up and monitoring from time to time the entire cathode surface cleaning procedure.

So far the procedure discussed above is identical to that for handling and surface cleaning a NEA photocathode. At this point, after vacuum heat cleaning, the TE cathode requires a Schottky-barrier contact to be evaporated onto the active emitter surface. A simple tungsten filament source with 5-9's pure Ag wire wrapped about the filament is used for this purpose. A Sloan digital film thickness monitor is employed to monitor the evaporation process. The Sloan monitor is calibrated by evaporating a relatively thick Ag film and measuring its thickness using a Varian model 980-4000- \AA scope interferometer. An evaporation rate of approximately 1 to 3 $\text{\AA}/\text{sec}$ is used and the Ag film thickness is on the order of 100 to 300 \AA . The Cs-O activation procedure is essentially that used for NEA cathodes, i.e. Cs-only and then Cs+O to a photoemission peak. Sometimes TE photoemission can be detected at the Cs-only point in which case the Cs+O activation procedure is monitored with a bias potential on the cathode. However whether the activation is monitored with no bias on the cathode (i.e. just a white-light monitor) or with a bias seems to give about equally good TE photoemission results. The bias is physically applied in the vacuum system by means of a point contact probe that is allowed to just touch the evaporated Ag film. The cathode holder, which is electrically isolated from the vacuum system walls, provides the other side of the biasing circuit contact. A battery-operated, regulated voltage

supply is used for the external biasing source. The electron current leaving the cathode or the collector current is used for photoemission and dark current measurements. In the earlier part of this contract period a mirror at the back of the vacuum system was positioned such that light from a monochromator source could be focussed onto the back of the cathode for semitransparent (i.e. transmission-mode) photoemission measurements. One vacuum system was later modified to have windows on both front and back so that transmission measurements can be made without a emitter. Photoemission results from three direct emitter cathodes are presented.

Since feasibility of the general approach had already been demonstrated (e.g. Fig. 6), the primary new task was one of optimizing the direct emitter cathode for 1.06-micron detection. From a materials standpoint this implies growing high quality p-InGaAsP on InP of the correct composition (≈ 1.15 eV bandgap) and doping concentration ($\sim 10^{15}/\text{cm}^3$). From a device processing standpoint this implies careful cathode surface cleaning procedures, Schottky-barrier evaporation, and Cs-O activation. Figure 49 shows reflection-mode yield from a direct emitter cathode (#PQ22-2) which has nearly an optimal bandgap and achieved approximately 1.0% yield at 1.06 microns. Figure 50 shows the field-assisted 1.06-micron yield vs applied bias. Note the Ag film and optical beam sizes. The cathode itself is 150 x 400 mils. The yield vs bias voltage curve shown in Fig. 50 is quite similar to that from a TE p-InP emitter. Dark current vs applied bias is shown in Fig. 51. The general shape of the dark current vs bias curve shown here is typical of those observed from p-InP emitters. However the magnitude of the dark current characteristics can be quite variable from cathode to cathode and even from the same cathode. As an example of this point consider the TE photoemission results from direct emitter cathode #PQ22-5 shown in Fig. 52. The

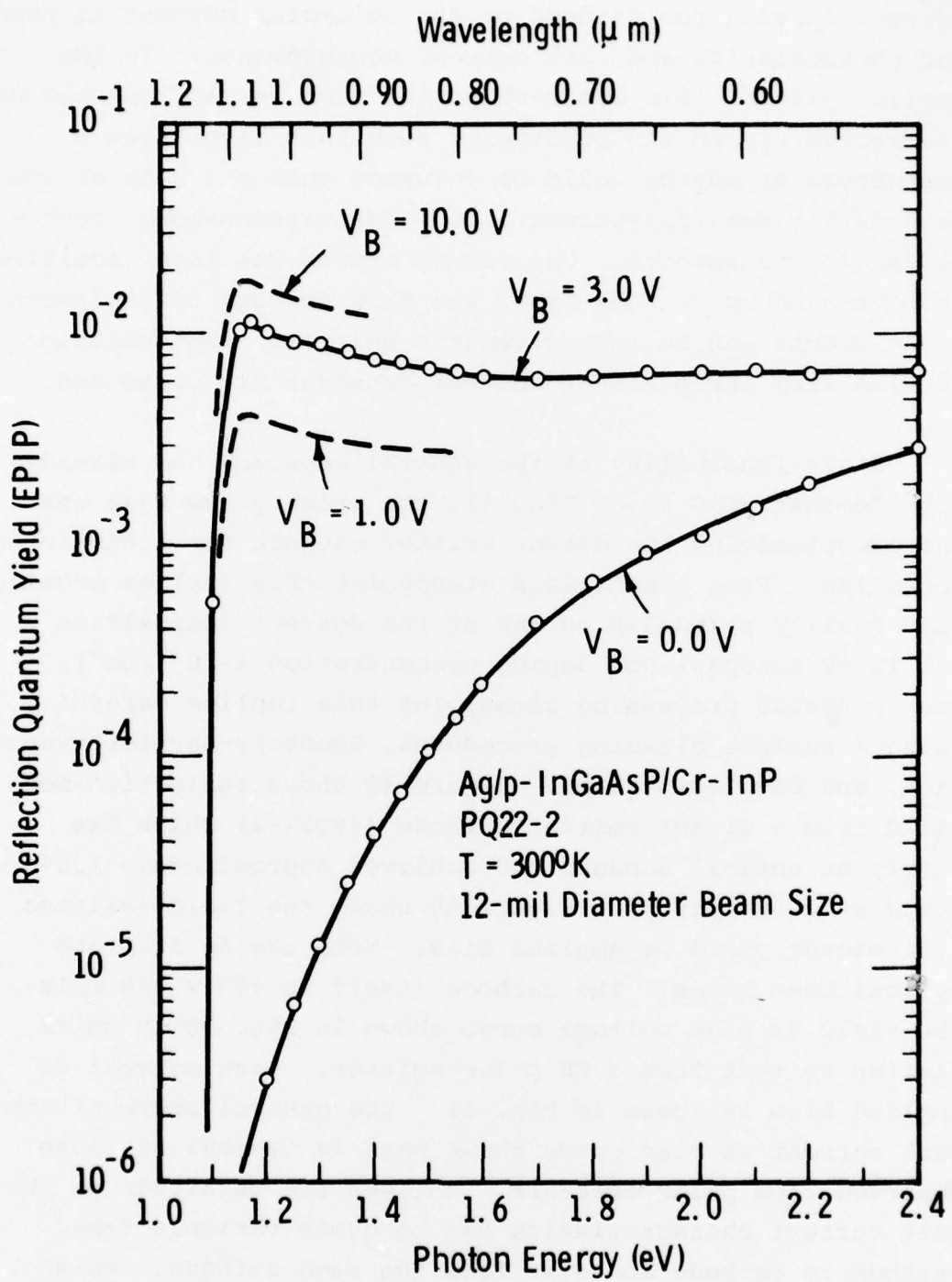


Fig. 49. Reflection-mode quantum yield from a direct emitter p-InGaAsP/InP TE cathode.

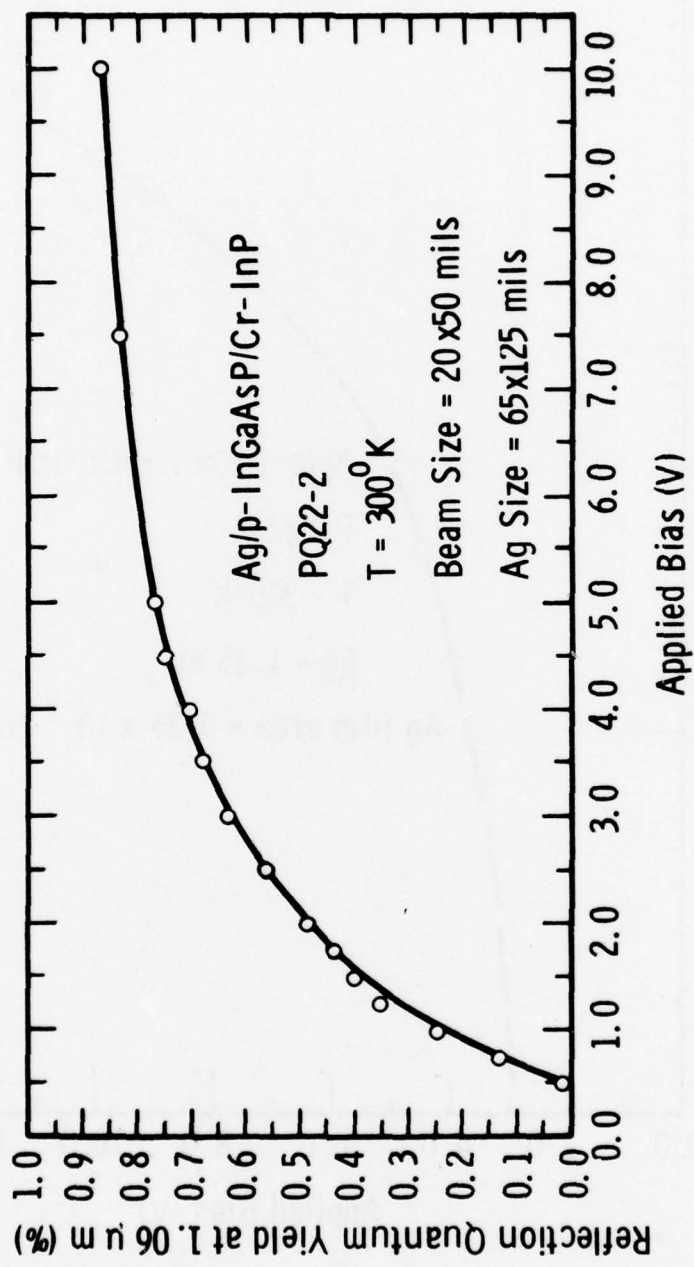


Fig. 50. Reflection-mode quantum yield at 1.06 microns vs applied bias from a p-InGaAsP direct emitter cathode.

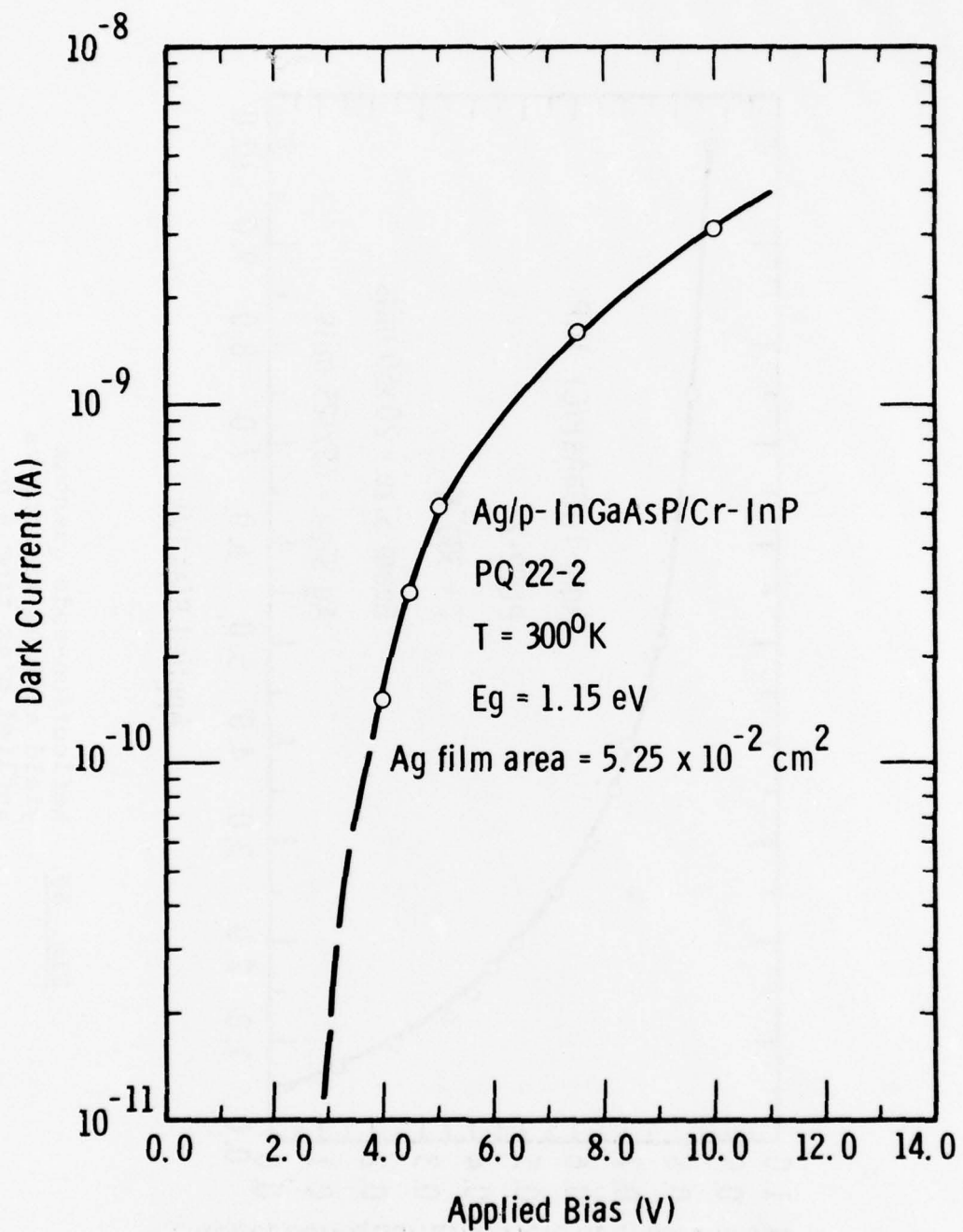


Fig. 51. Dark current emission vs applied bias from a p-InGaAsP direct emitter cathode at 300°K .

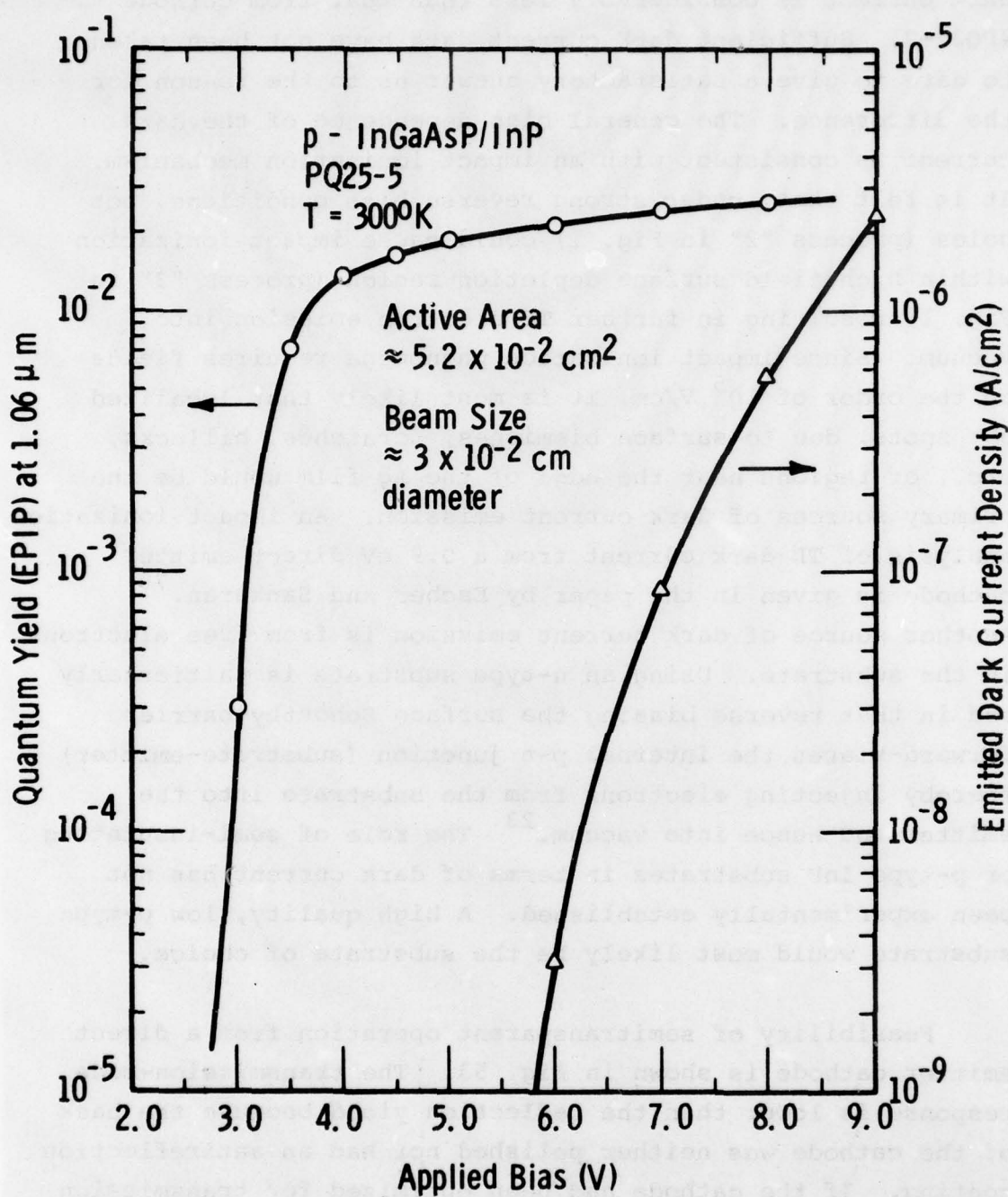


Fig. 52. Reflection-mode quantum yield at 1.06 microns and dark current density vs applied bias from a p-InGaAsP direct emitter.

field-assisted yield at 1.06 micron is above 1.0%, yet the dark current is considerably less than that from cathode #PQ22-2. Sufficient dark current data have not been taken to date to give a satisfactory answer as to the reason for the difference. The general bias dependence of the dark current is consistent with an impact ionization mechanism. It is felt that, under strong reverse bias conditions, hot holes (process "2" in Fig. 1) could cause impact ionization within high field surface depletion region (process "3" in Fig. 1) resulting in further TE electron emission into vacuum. Since impact ionization phenomena requires fields on the order of 10^5 V/cm, it is most likely that localized hot spots, due to surface blemishes, scratches, hillocks, etc., or regions near the edge of the Ag film would be the primary sources of dark current emission. An impact ionization analysis of TE dark current from a 0.9 eV direct emitter cathode is given in the paper by Escher and Sankaran.⁷⁸ Another source of dark current emission is from free electrons in the substrate. Using an n-type substrate is particularly bad in that reverse biasing the surface Schottky-barrier forward-biases the internal p-n junction (substrate-emitter) thereby injecting electrons from the substrate into the emitter and hence into vacuum.²³ The role of semi-insulating or p-type InP substrates in terms of dark current has not been experimentally established. A high quality, low p-type substrate would most likely be the substrate of choice.

Feasibility of semitransparent operation from a direct emitter cathode is shown in Fig. 53. The transmission-mode response is lower than the reflection yield because the back of the cathode was neither polished nor had an antireflection coating. If the cathode had been optimized for transmission response, the semitransparent yield at 1.06 microns could well have been 20% or so higher than the front-surface yield. The short wavelength cut-off at approximately 9300 Å

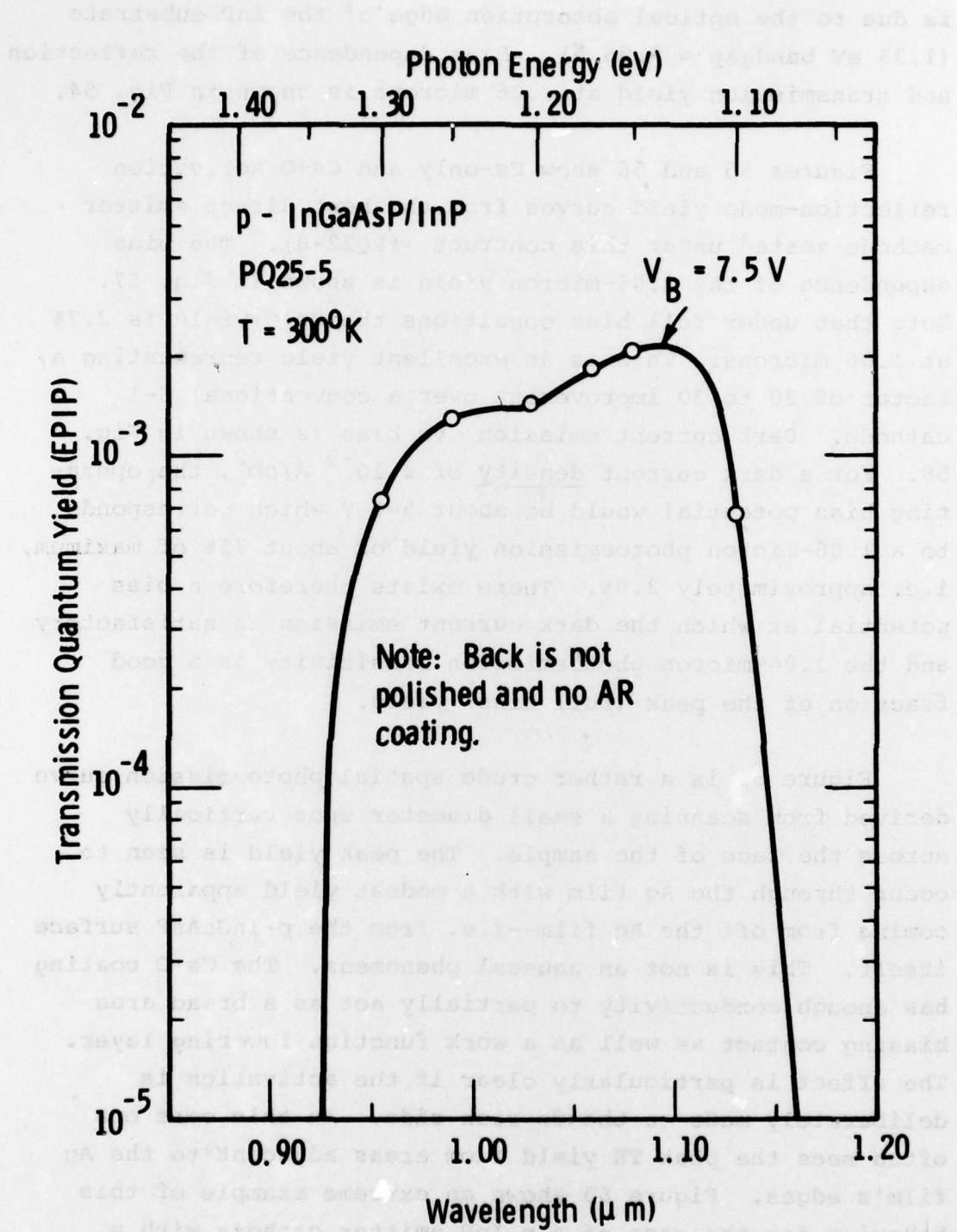


Fig. 53. Transmission-mode quantum yield from a p-InGaAsP direct emitter cathode.

is due to the optical absorption edge of the InP substrate (1.35 eV bandgap = 9.85 Å). Bias dependence of the reflection and transmission yield at 1.06 microns is shown in Fig. 54.

Figures 55 and 56 show Cs-only and Cs+O activation reflection-mode yield curves from the best direct emitter cathode tested under this contract (#PQ22-8). The bias dependence of the 1.06-micron yield is shown in Fig. 57. Note that under full bias conditions the Cs+O yield is 2.7% at 1.06 microns. This is an excellent yield representing a factor of 20 to 30 improvement over a conventional S-1 cathode. Dark current emission vs bias is shown in Fig. 58. For a dark current density of $\leq 10^{-9}$ A/cm², the operating bias potential would be about 5-6 V which corresponds to a 1.06-micron photoemission yield of about 75% of maximum, i.e. approximately 2.0%. There exists therefore a bias potential at which the dark current emission is satisfactory and the 1.06-micron photoemission sensitivity is a good fraction of the peak (full bias) yield.

Figure 59 is a rather crude spatial photoemission curve derived from scanning a small diameter spot vertically across the face of the sample. The peak yield is seen to occur through the Ag film with a modest yield apparently coming from off the Ag film--i.e. from the p-InGaAsP surface itself. This is not an unusual phenomena. The Cs-O coating has enough conductivity to partially act as a broad area biasing contact as well as a work function lowering layer. The effect is particularly clear if the activation is deliberately made on the Cs-rich side. In this case one often sees the peak TE yield from areas adjacent to the Ag film's edges. Figure 60 shows an extreme example of this behavior for the case of a p-InP emitter cathode with a rather thick (600Å) Ag film. An interesting related phenomena often observed in those cases where there is significant

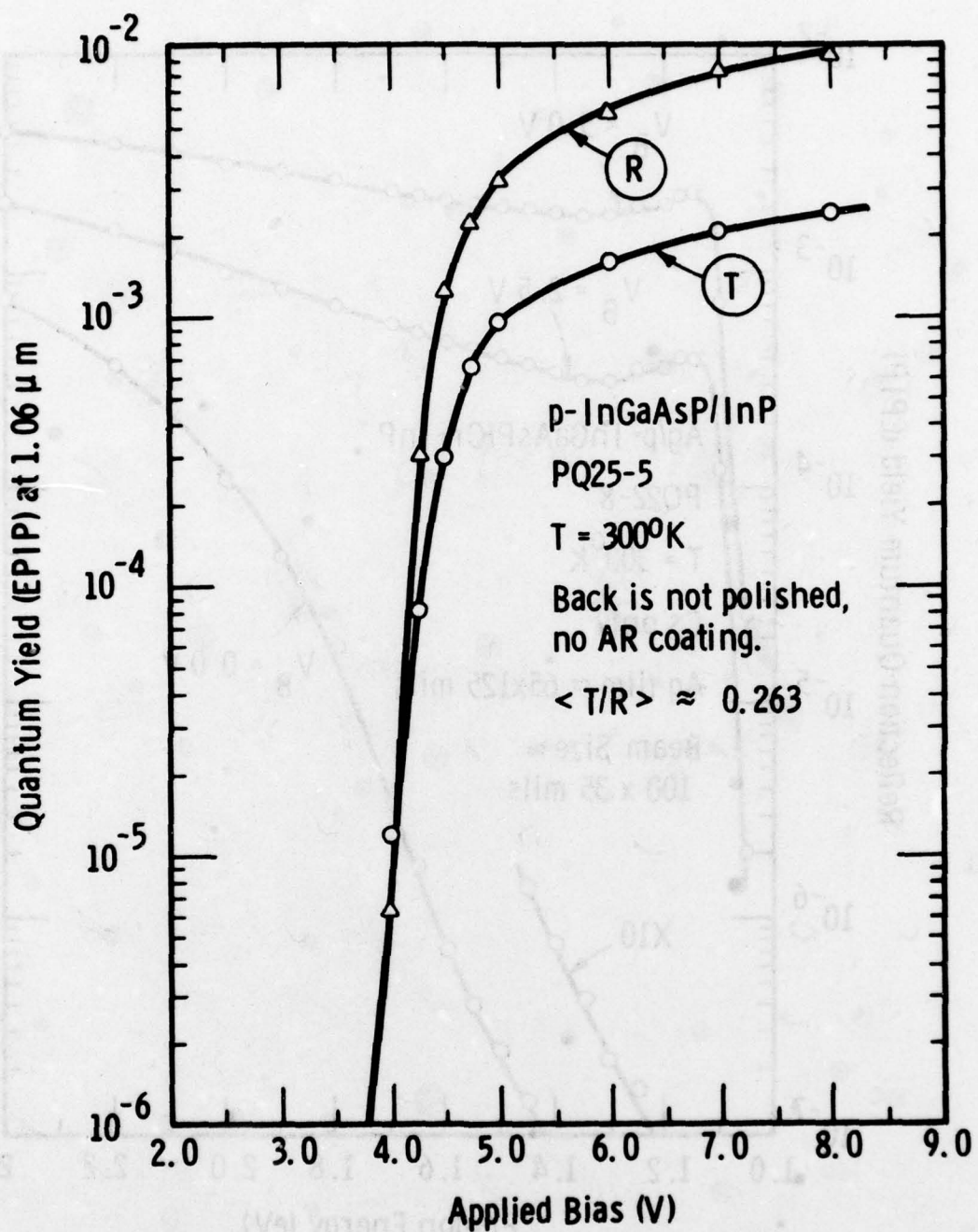


Fig. 54. Reflection-mode (R) and transmission-mode (T) yield at 1.06 microns vs applied bias from a p-InGaAsP direct emitter cathode.

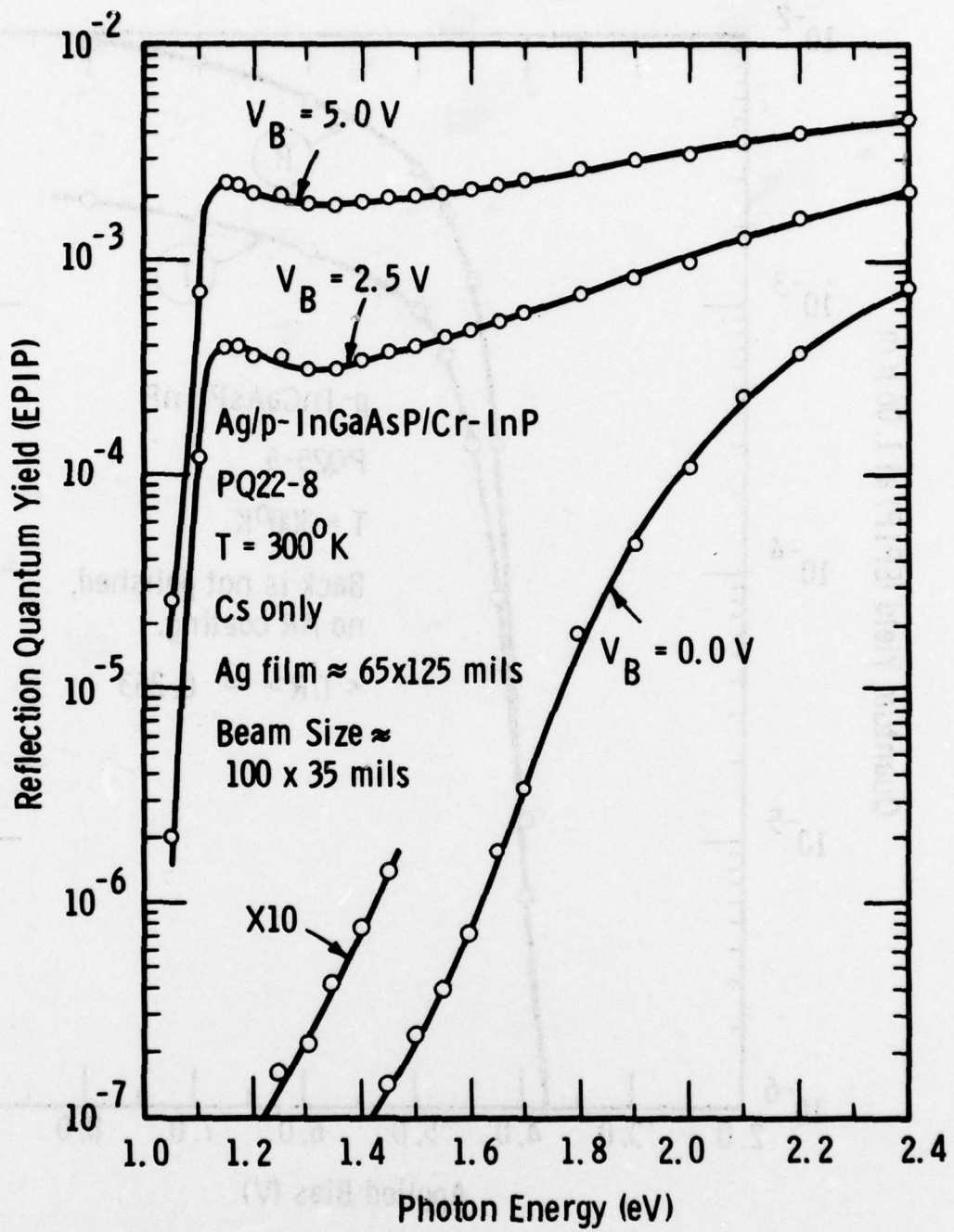


Fig. 55. Reflection-mode quantum yield, Cs-only, from a p-InGaAsP direct emitter cathode.

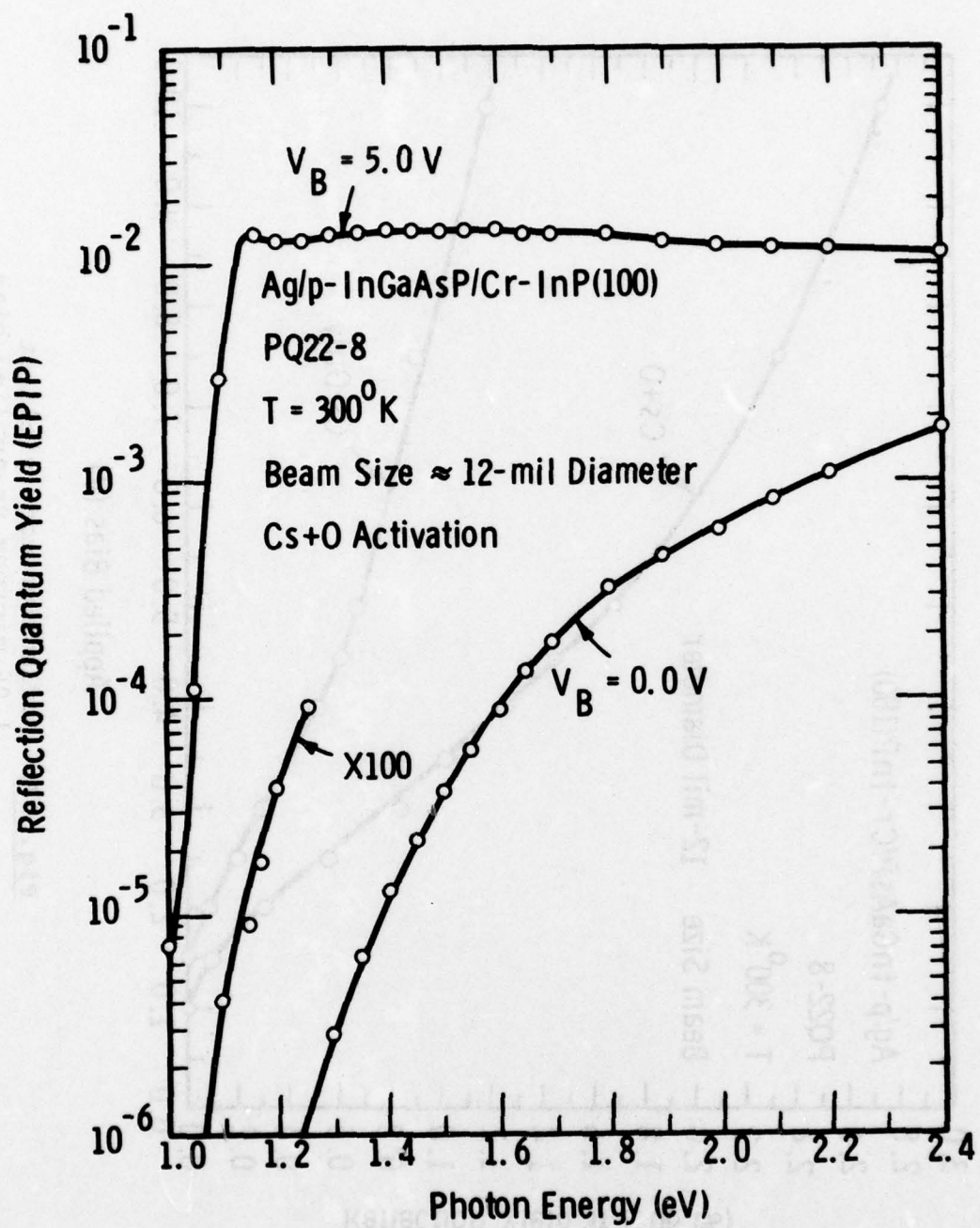


Fig. 56. Reflection-mode quantum yield, Cs+O activation, from a p-InGaAsP direct emitter cathode.

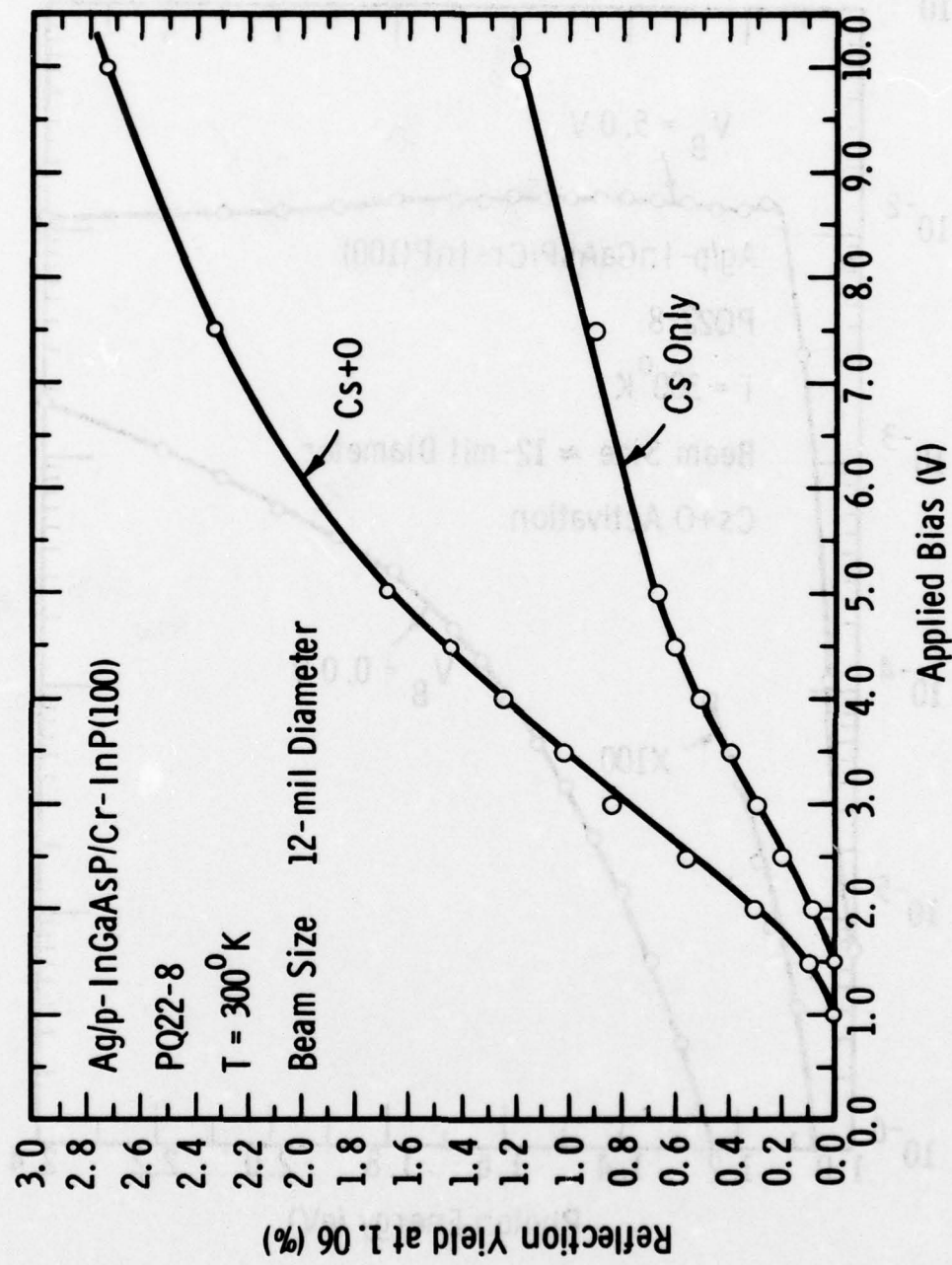


Fig. 57. Reflection-mode yield at 1.06 microns vs applied bias from a p-InGaAsP direct emitter cathode.

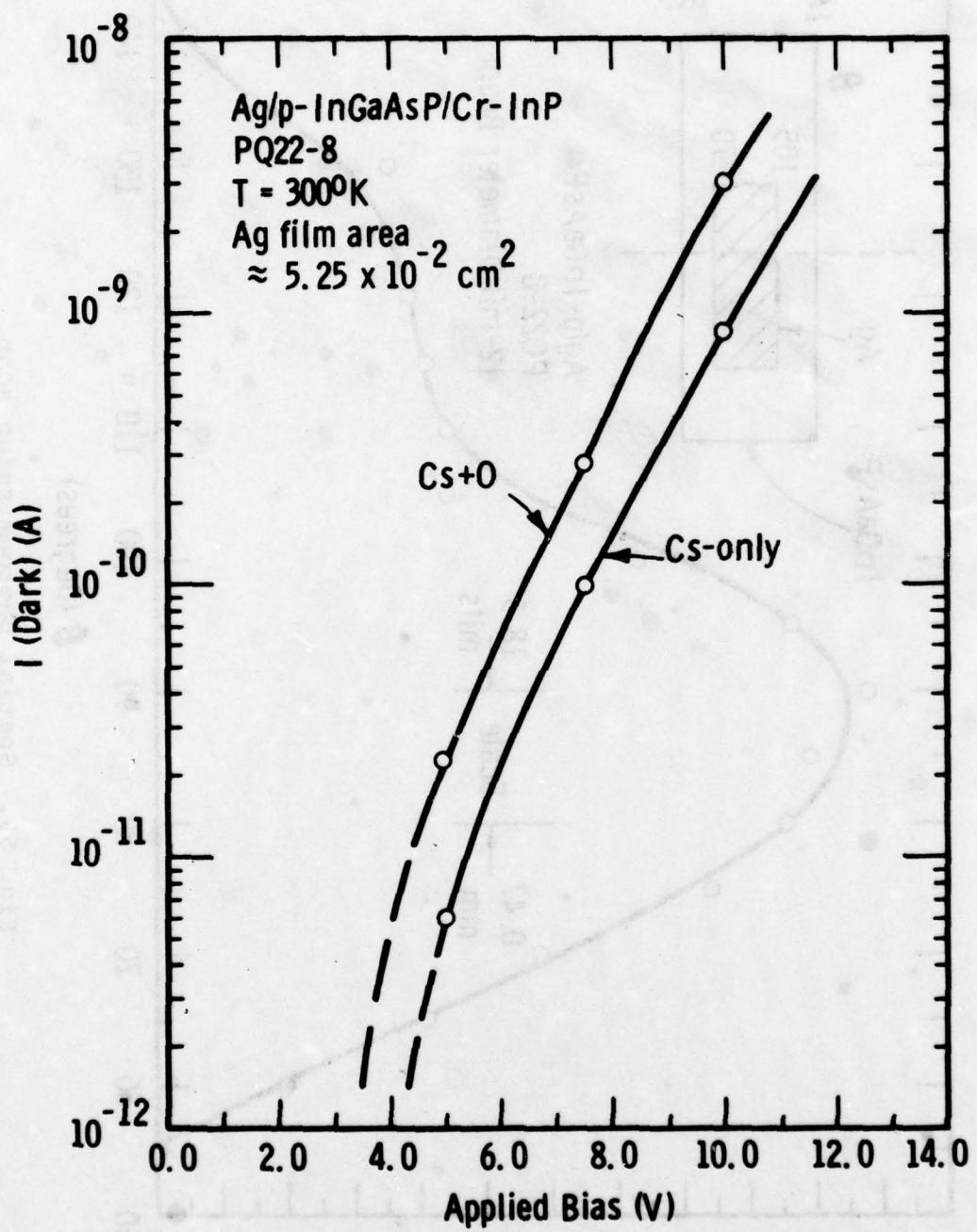


Fig. 58. Dark current emission from a direct emitter cathode at 300°K.

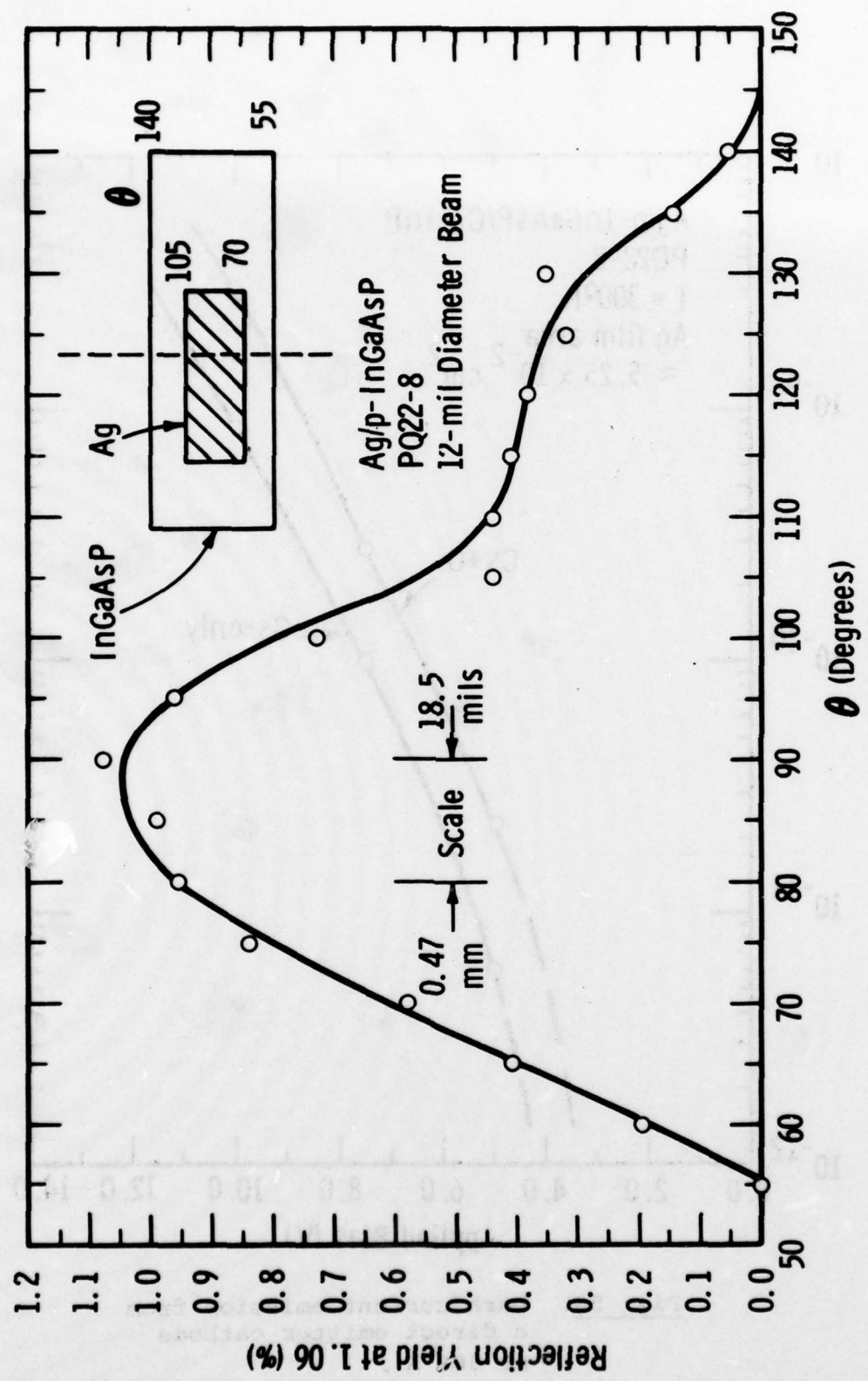


Fig. 59. Spatial Photoemission scan at 1.06 microns across the face of a p-InGaAsP direct emitter cathode.

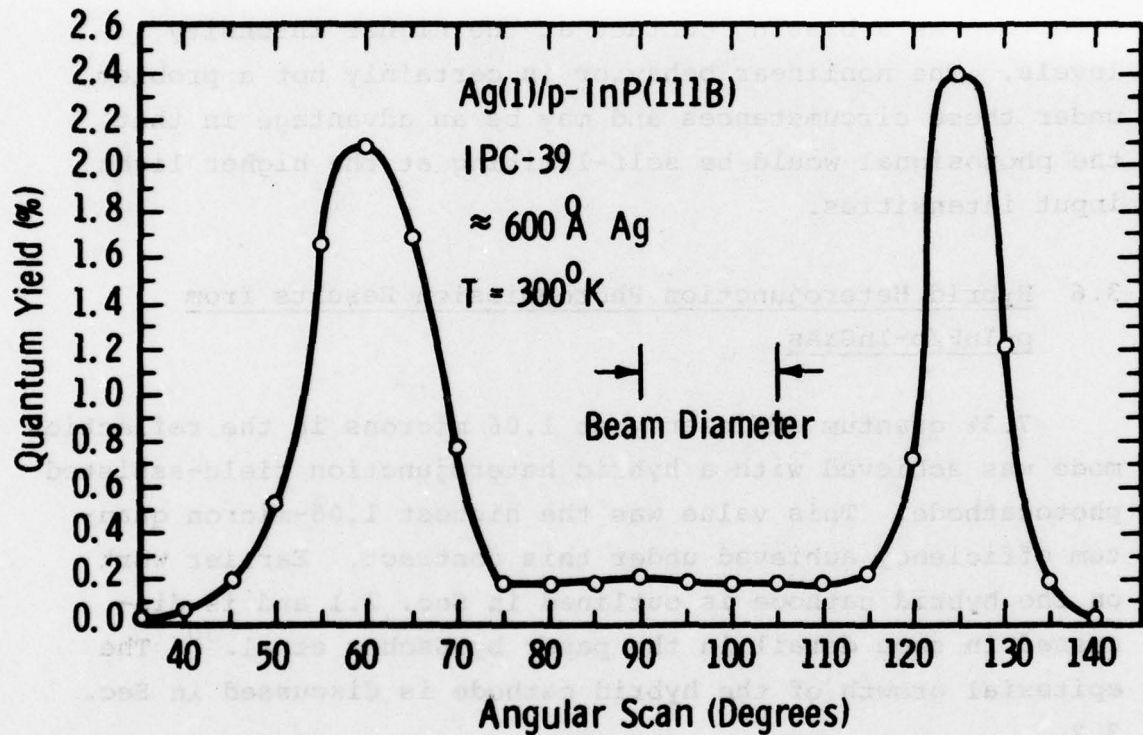


Fig. 60. Spatial photoemission scan across the face of a p-

InP TE photocathode.

TE yield from off the Ag film is a pronounced nonlinear behavior in the photoemission signal vs light intensity. Typical incident photon irradiance power densities on the order of 1×10^{-4} W/cm² are employed for most yield curve data taking.⁷⁹ However a linear photoemission signal vs light intensity behavior often does not occur for power densities a factor of 30-100 times lower. Presumably the reason for this is that the Cs-O activation layer is less effective as a biasing contact at the higher intensity levels. The nonlinear behavior is certainly not a problem under these circumstances and may be an advantage in that the photosignal would be self-limiting at the higher light input intensities.

3.6 Hybrid Heterojunction Photoemission Results from p-InP/p-InGaAs

7.3% quantum efficiency at 1.06 microns in the reflection mode was achieved with a hybrid heterojunction field-assisted photocathode. This value was the highest 1.06-micron quantum efficiency achieved under this contract. Earlier work on the hybrid cathode is outlined in Sec. 2.1 and is discussed in some detail in the paper by Escher et al.³⁰ The epitaxial growth of the hybrid cathode is discussed in Sec. 3.2.

Figure 61 shows the reflection mode quantum yield from hybrid cathode #8-17, and compares it to that from a conventional Si photocathode. The yield from cathode #8-17 was 7.3% at 1.06 microns in the reflection mode, with 4 volts bias. As Fig. 61 shows, at 4 volts bias the yield is nearly flat from 0.8 to 1.06 microns. Photons with energy above the InP bandgap of 1.35 eV (0.92 micron) are absorbed in the InP, while photons with energy below the InP bandgap are absorbed in the InGaAsP absorber layer. Thus the flat yield

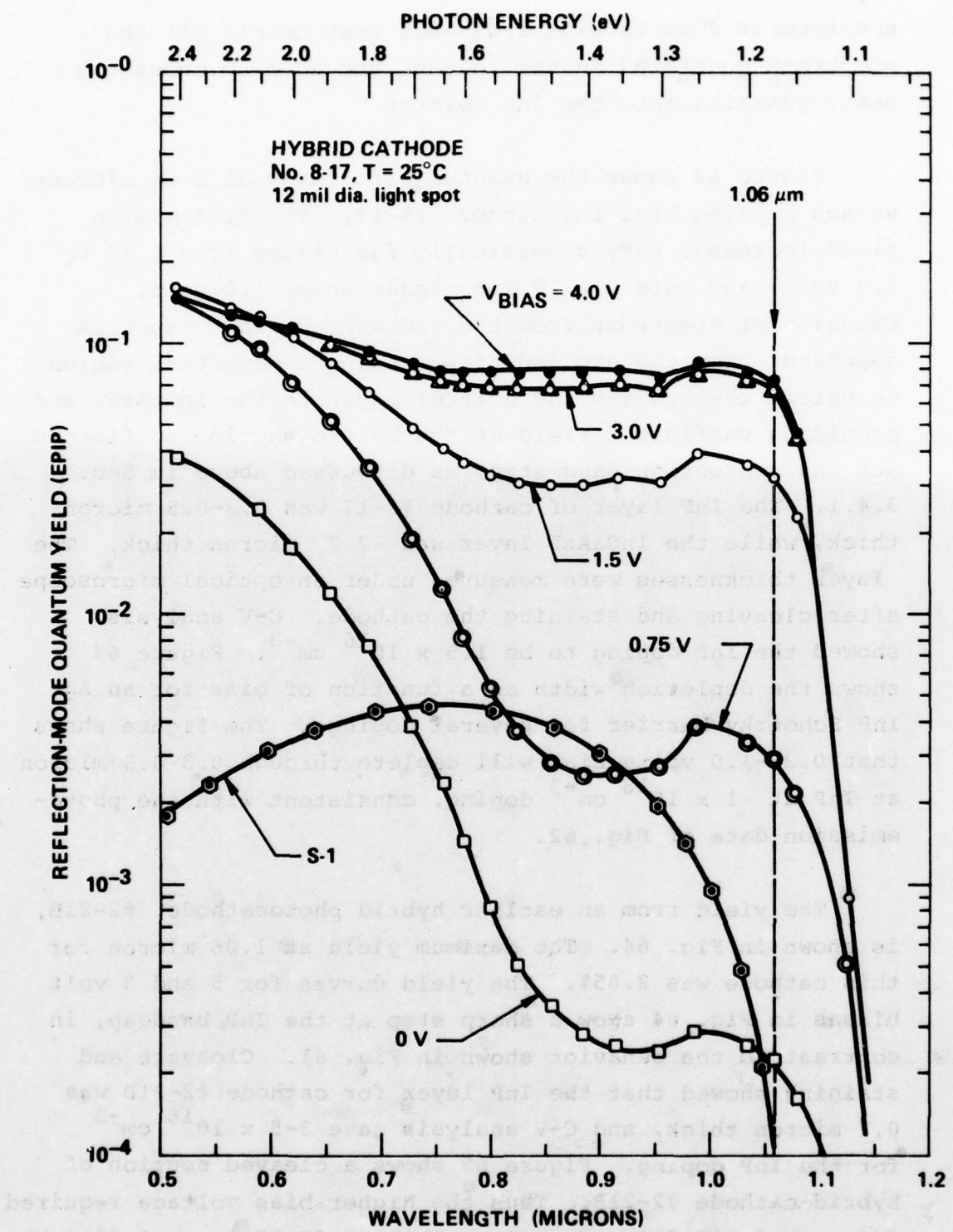


Fig. 61. Reflection mode quantum yield from InP/InGaAs hybrid cathode #8-17.

spectrum at 4 volts bias indicates that nearly all the electrons generated in the InGaAsP are able to cross the heterojunction into the InP emitter.

Figure 62 shows the quantum efficiency at 1.06 microns versus applied bias for cathode #8-17. The 1.06-micron yield increases very dramatically for biases from 0.25 to 1.0 volt, and more slowly for biases above 1.0 volt. Emission of electrons from the InGaAsP absorber layer is dependent upon the applied bias causing a depletion region to extend through the InP emitter layer to the InGaAsP, and providing sufficient field at the heterojunction to flatten out the conduction band step, as discussed above in Sec. 3.4.1. The InP layer of cathode #8-17 was 0.3-0.5 micron thick, while the InGaAsP layer was ~2.2 micron thick. The layer thicknesses were measured under an optical microscope after cleaving and staining the cathode. C-V analysis showed the InP doping to be $1.5 \times 10^{16} \text{ cm}^{-3}$. Figure 63 shows the depletion width as a function of bias for an Ag-InP Schottky barrier for several dopings. The figure shows that 0.25-1.0 volts bias will deplete through 0.3-0.5 micron at InP at $\sim 1 \times 10^{16} \text{ cm}^{-3}$ doping, consistent with the photo-emission data of Fig. 62.

The yield from an earlier hybrid photocathode, #2-21B, is shown in Fig. 64. The maximum yield at 1.06 micron for this cathode was 2.85%. The yield curves for 5 and 3 volt biases in Fig. 64 show a sharp step at the InP bandgap, in contrast to the behavior shown in Fig. 61. Cleavage and staining showed that the InP layer for cathode #2-21B was 0.7 micron thick, and C-V analysis gave $3-5 \times 10^{16} \text{ cm}^{-3}$ for the InP doping. Figure 65 shows a cleaved section of hybrid cathode #2-21B. Thus the higher bias voltage required for cathode #2-21B compared to cathode #8-17 is explained by

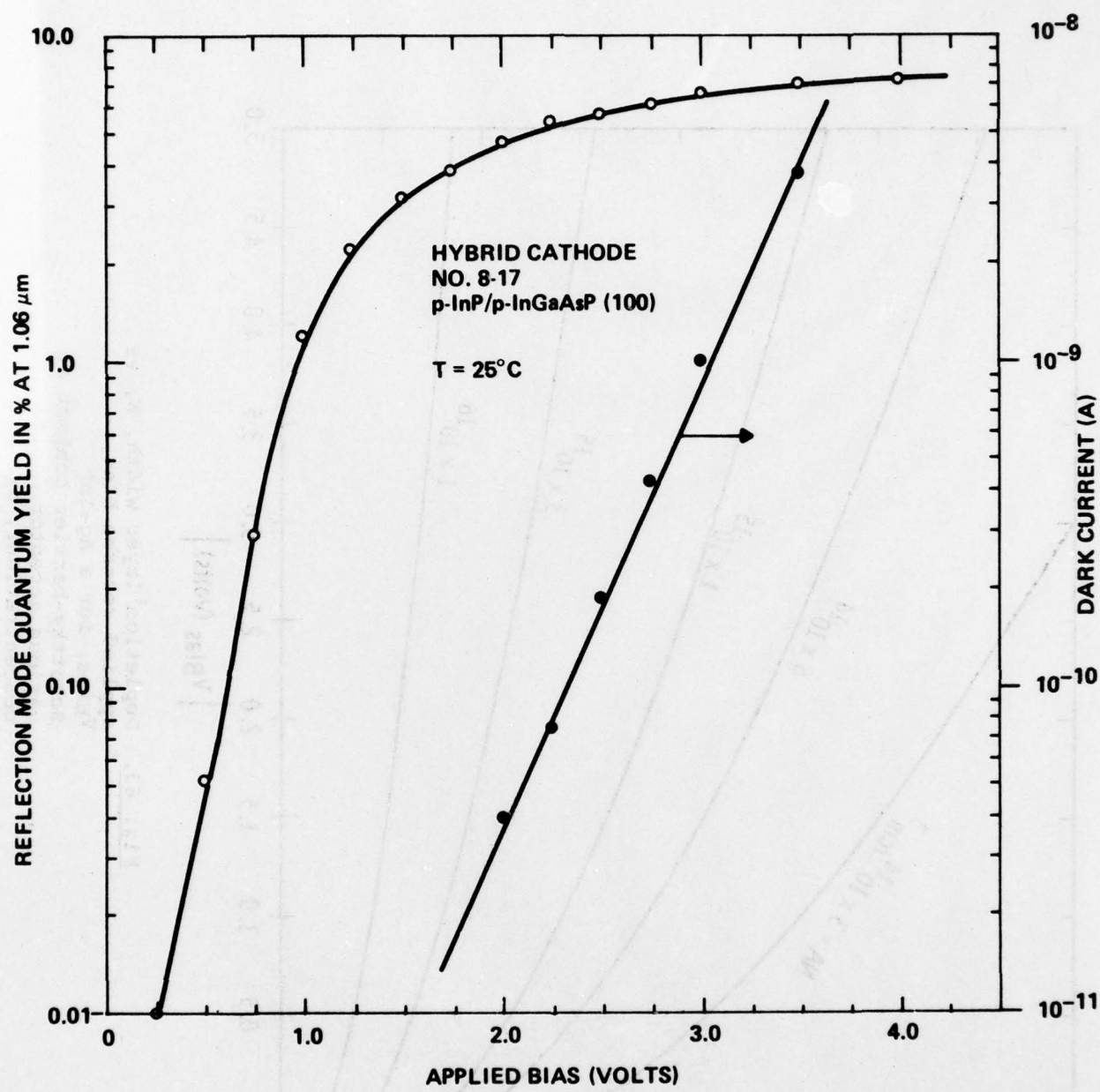


Fig. 62. Reflection-mode quantum yield at 1.06 microns, and emitted dark current, as a function of bias for InP/InGaAs hybrid cathode #8-17.

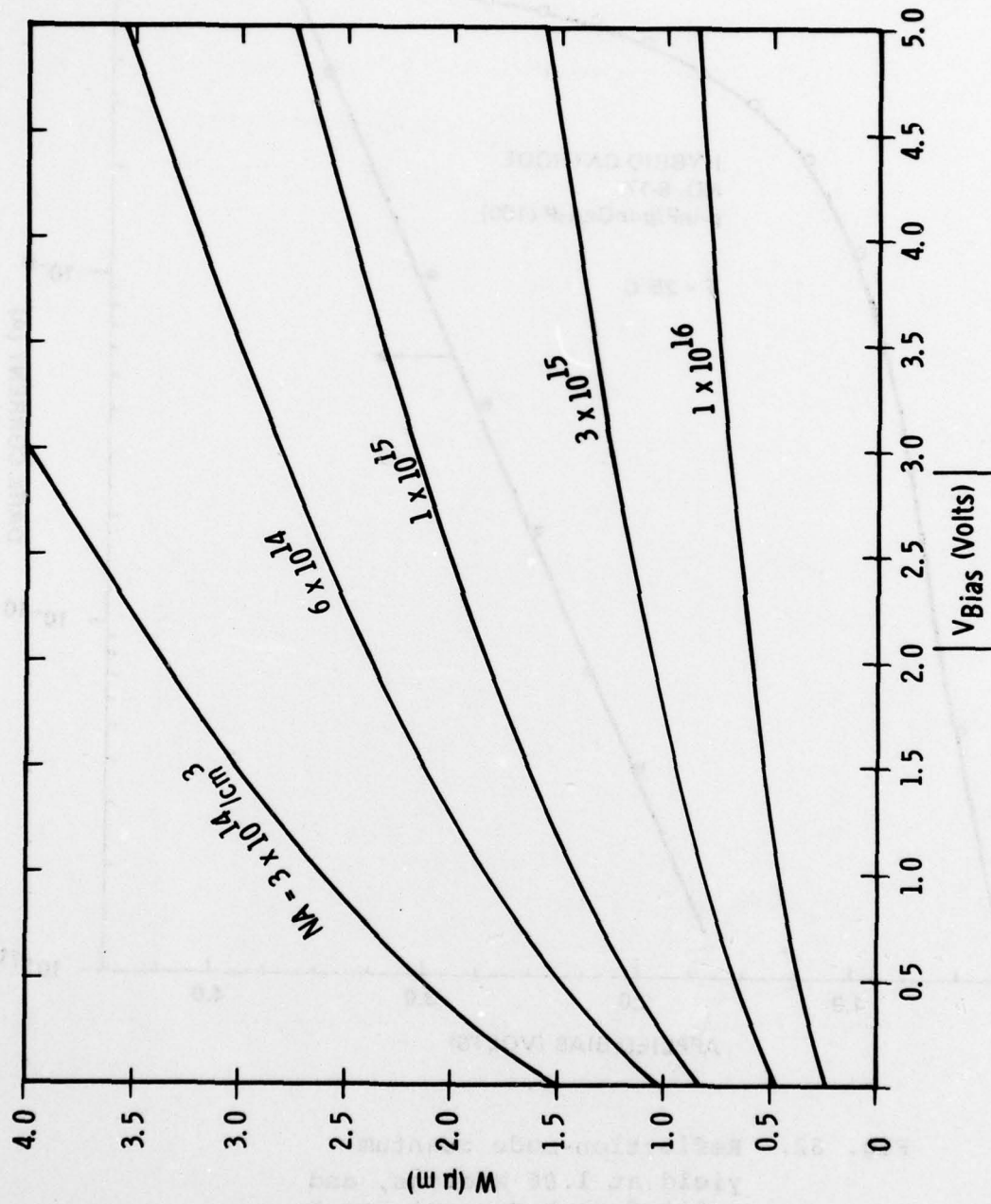


Fig. 63. Depletion layer width, W , vs applied reverse bias, V_{bias} , for a Ag-InP Schottky-barrier contact at various acceptor doping concentrations, N_A .

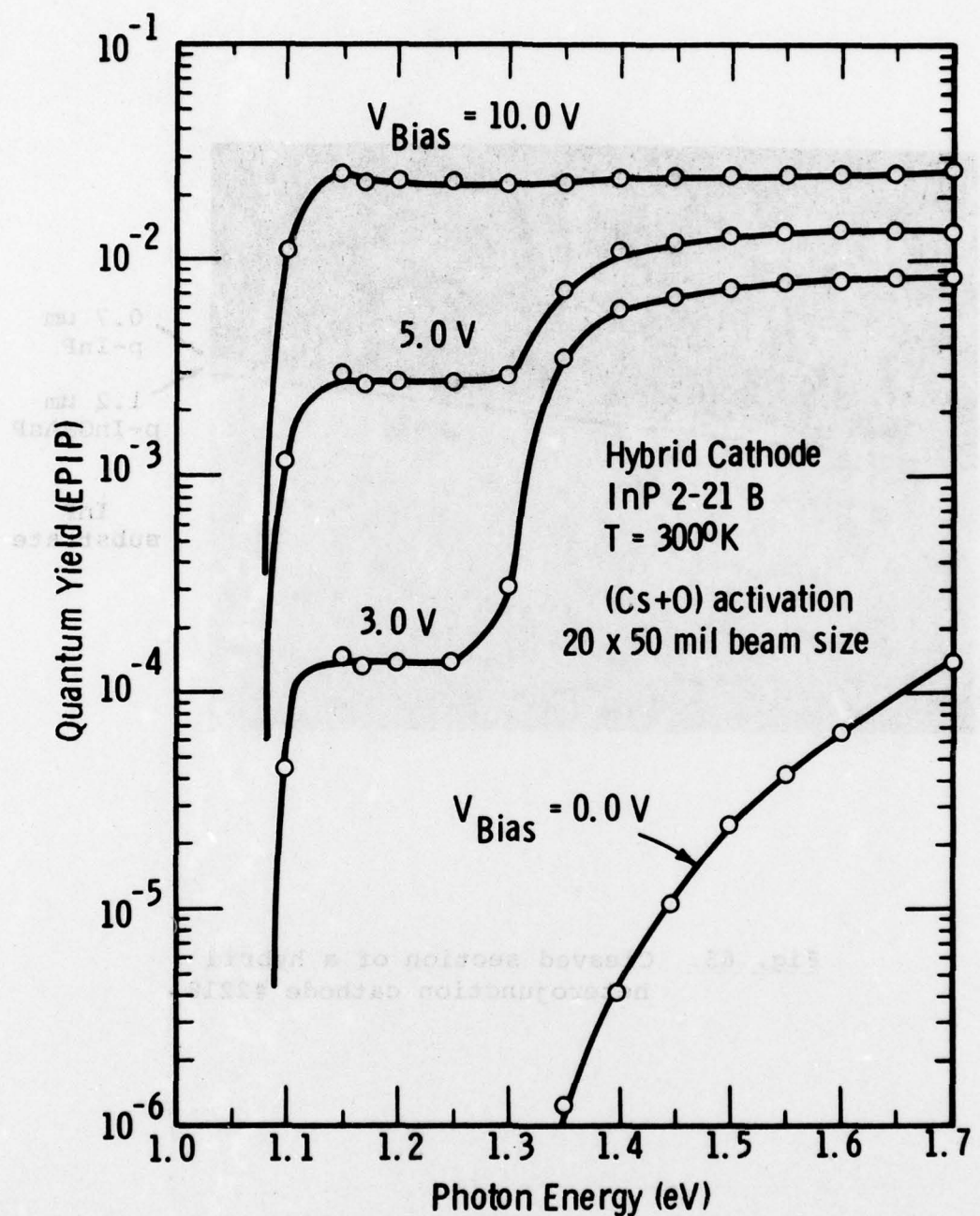


Fig. 64. Reflection-mode quantum yield from a p-InP/p-InGaAsP hybrid heterojunction TE cathode.

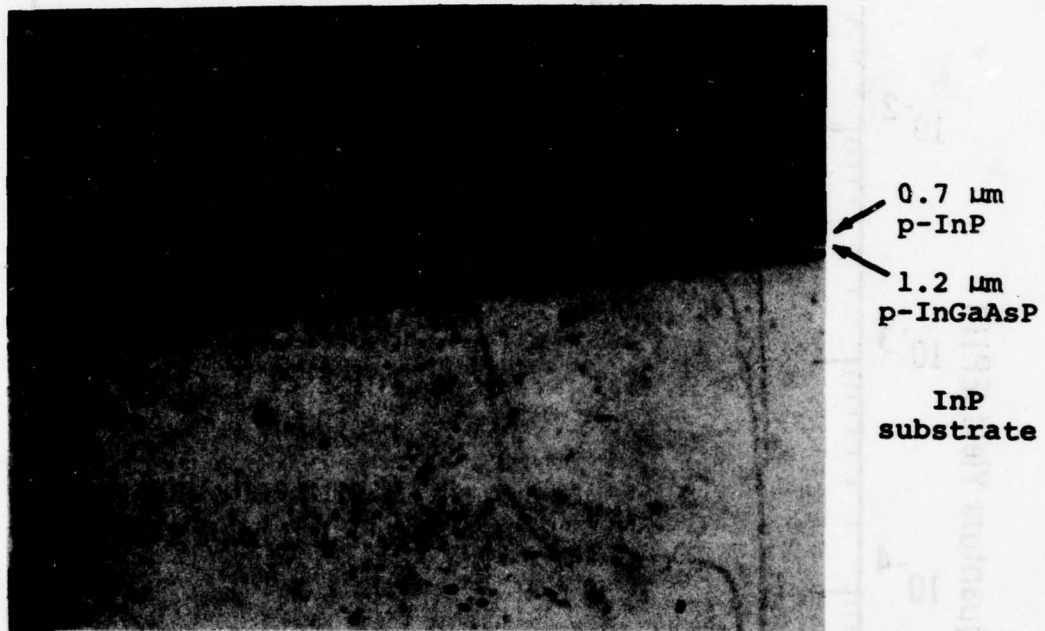


Fig. 65. Cleaved section of a hybrid heterojunction cathode #2218.

cathode #2-21B having a thicker emitter layer that is more heavily doped than the emitter layer of cathode #8-17.

Figure 66 shows the yield versus bias for $h\nu = 1.4$ and 1.17 eV for cathode #2-21B. (The yield data for Fig. 66 was measured from a different spot on the cathode than was the data of Fig. 64, which is why the yield values are not the same in the two figures.) Figure 67 shows the approximate heterojunction transfer efficiency versus bias, obtained by dividing the yield values for $h\nu = 1.17$ eV by those for $h\nu = 1.4$ eV, using the same data as is shown in Fig. 66.

Figure 68 shows the dark current versus bias for cathode #2-21B. A comparison of this dark current data with that shown in Fig. 62 for cathode #8-17 shows that for the bias which gives the best 1.06-micron response in each cathode, the dark current of cathode #2-21B is much higher than that of #8-17. If the primary source of dark current is impact ionization by hot holes,⁷⁸ then the dark current is expected to increase strongly with doping. This dependence of dark current on doping has not yet been well established experimentally, but the behavior of the dark current of these two cathodes is at least in the expected direction.

Auger spectra of the Ag film on the cathodes usually shows an In peak in addition to the Ag peaks. Figure 69 shows an Auger spectrum for a relatively thick Ag film on InP. Figure 70⁸⁰ shows an Auger sputter profile through the Ag film. The profile shows that In is present throughout the Ag, with some In segregation at the surface. The fact that P does not extend through the Ag demonstrates that the In is intermixed with the Ag rather than just showing through pinholes in the Ag. The intermixing of the Ag with the InP seems to be an unavoidable side effect of the evaporation process. Such intermixing has been seen in other semiconductor/metal systems also.⁸¹⁻⁸³

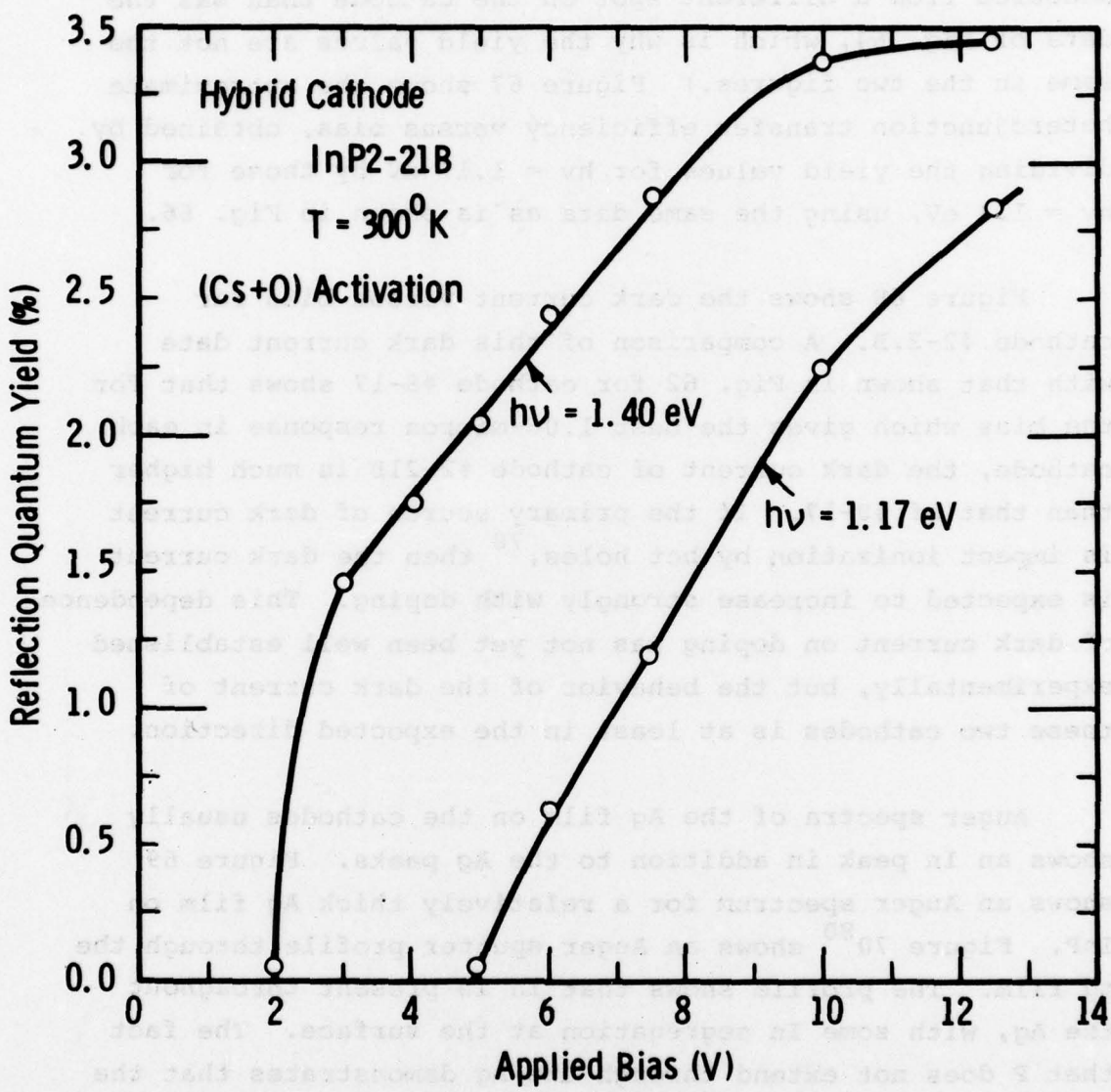


Fig. 66. Reflection-mode yield at 1.40 and 1.17 eV photon energy vs applied bias from a hybrid heterojunction cathode.

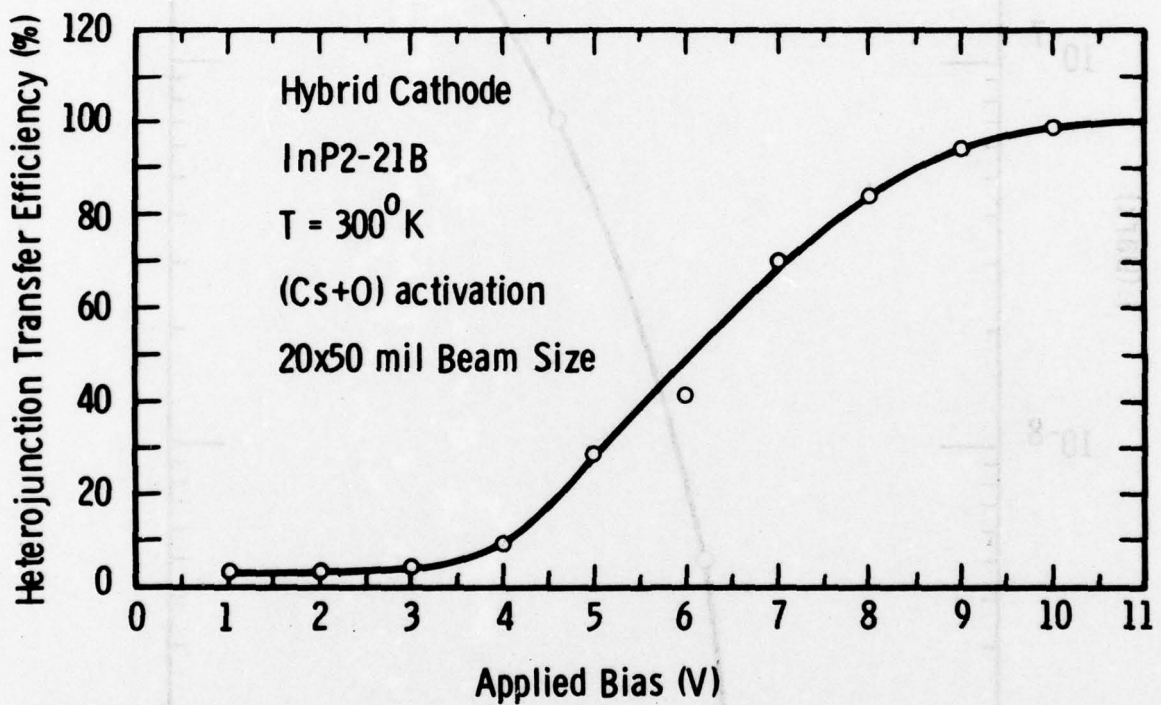


Fig. 67. Heterojunction transfer efficiency vs applied bias from a hybrid heterojunction cathode .

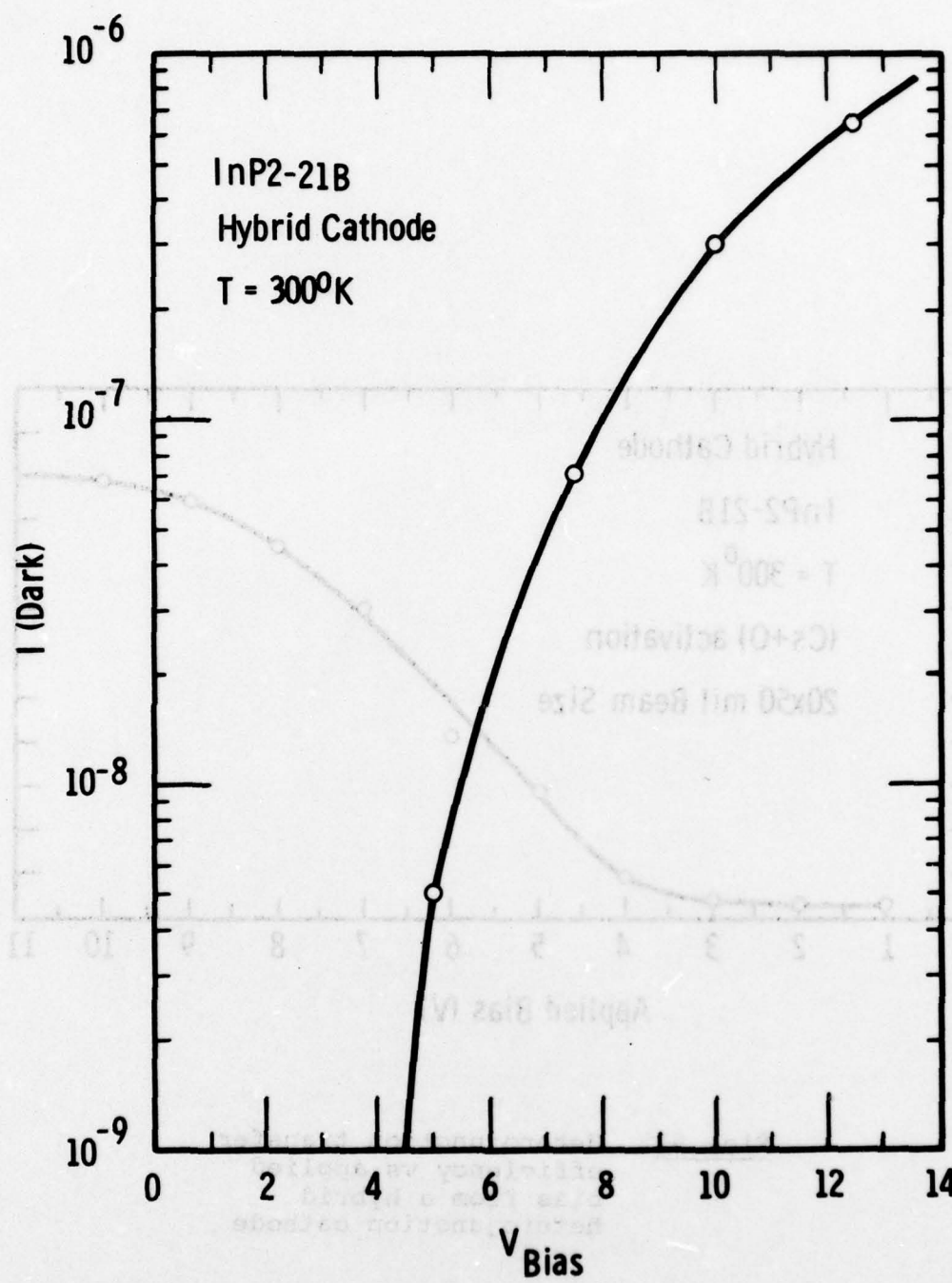


Fig. 68. Dark current emission vs
 applied bias from a
 hybrid heterojunction
 cathode at 300°K.

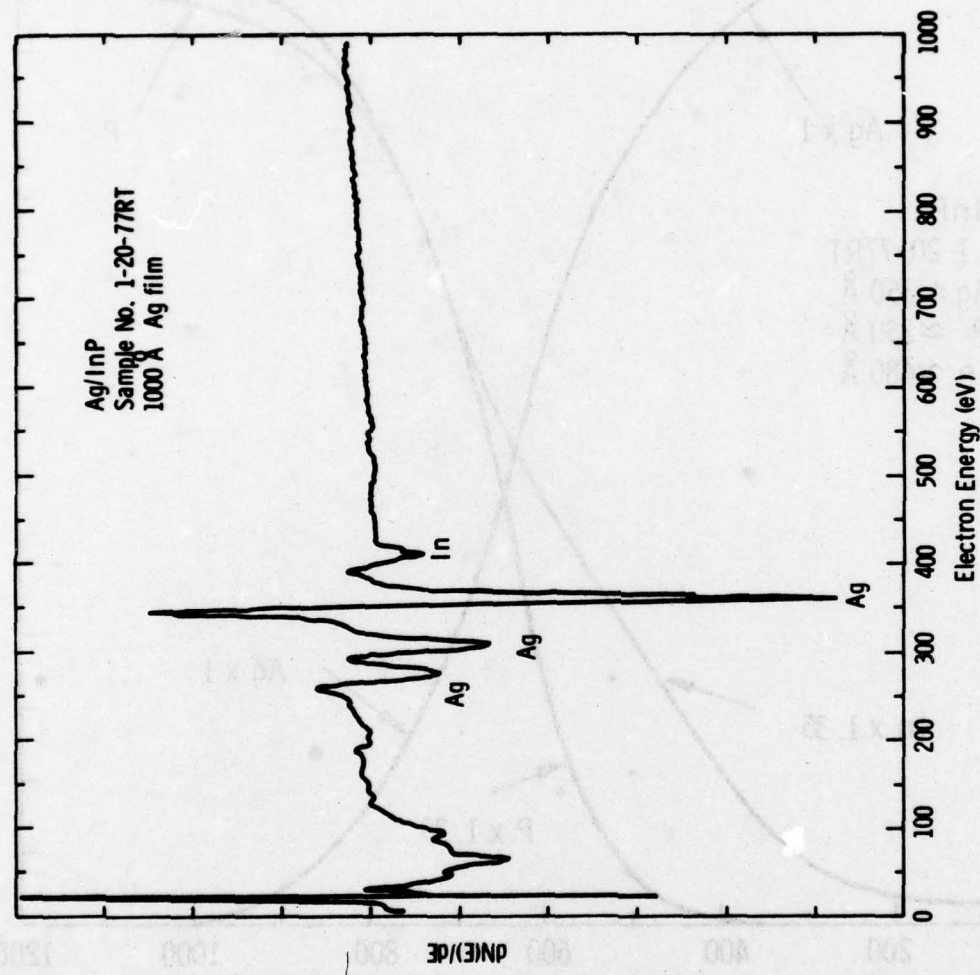


Fig. 69. Auger spectrum from the surface of an Ag/InP cathode showing In on the Ag film surface.

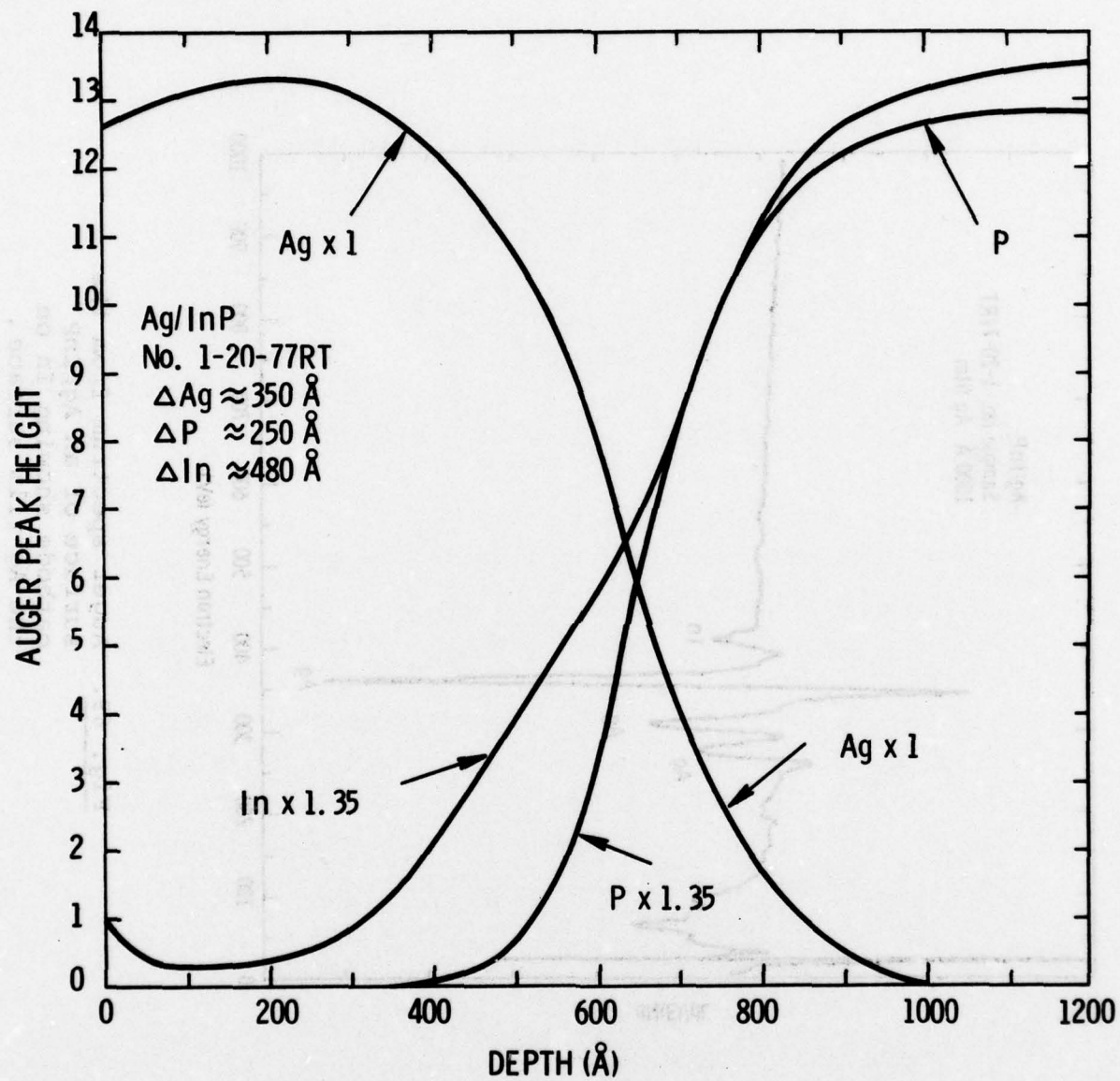


Fig. 70. Auger depth profile through a Ag/InP interface.

It is not known to what extent the intermixing of In with the Ag effects the operation of these cathodes. It has been noted, however, that the work function (measured by a Fowler plot of the yield threshold) is higher on surfaces with greater In content, after Cs+O activation. Figure 71 shows photoelectric threshold versus In/Ag peak height ratios.

In an effort to limit the amount of In intermixing, hybrid cathode #2-21B was given only a low heat clean - 500°C (oven temperature) rather than the 610° heat clean.

The assumption was that the lower heat clean temperature would leave a trace of oxygen on the InP surface, and this oxygen would inhibit the interdiffusion. No data is available on the interdiffusion, but Fig. 72 shows that the yield threshold of #2-21B was ~1.34 eV, which is quite high. A more typical threshold is 1.0-1.2 eV (see, for example, Fig. 49). Thus the lower heat clean temperature was not successful in lowering work function

Despite any effects caused by In interdiffusion, hybrid cathode #8-17 achieved 7.3% quantum efficiency at 1.06-micron wavelength. Furthermore, it is reasonable to expect that further optimization of the InP emitter layer and of the activation process would allow quantum efficiencies of ~10% to be achieved at 1.06 micron.

3.7 Photoemission Studies of InGaP/InGaAs/GaAs Cathodes

3.7.1 InGaP Emitter-Only Cathodes

The first stage in the development of the growth of the VPE InGaP/InGaAs/GaAs cathode was to establish the conditions for the VPE growth of InGaP on GaAs. The second

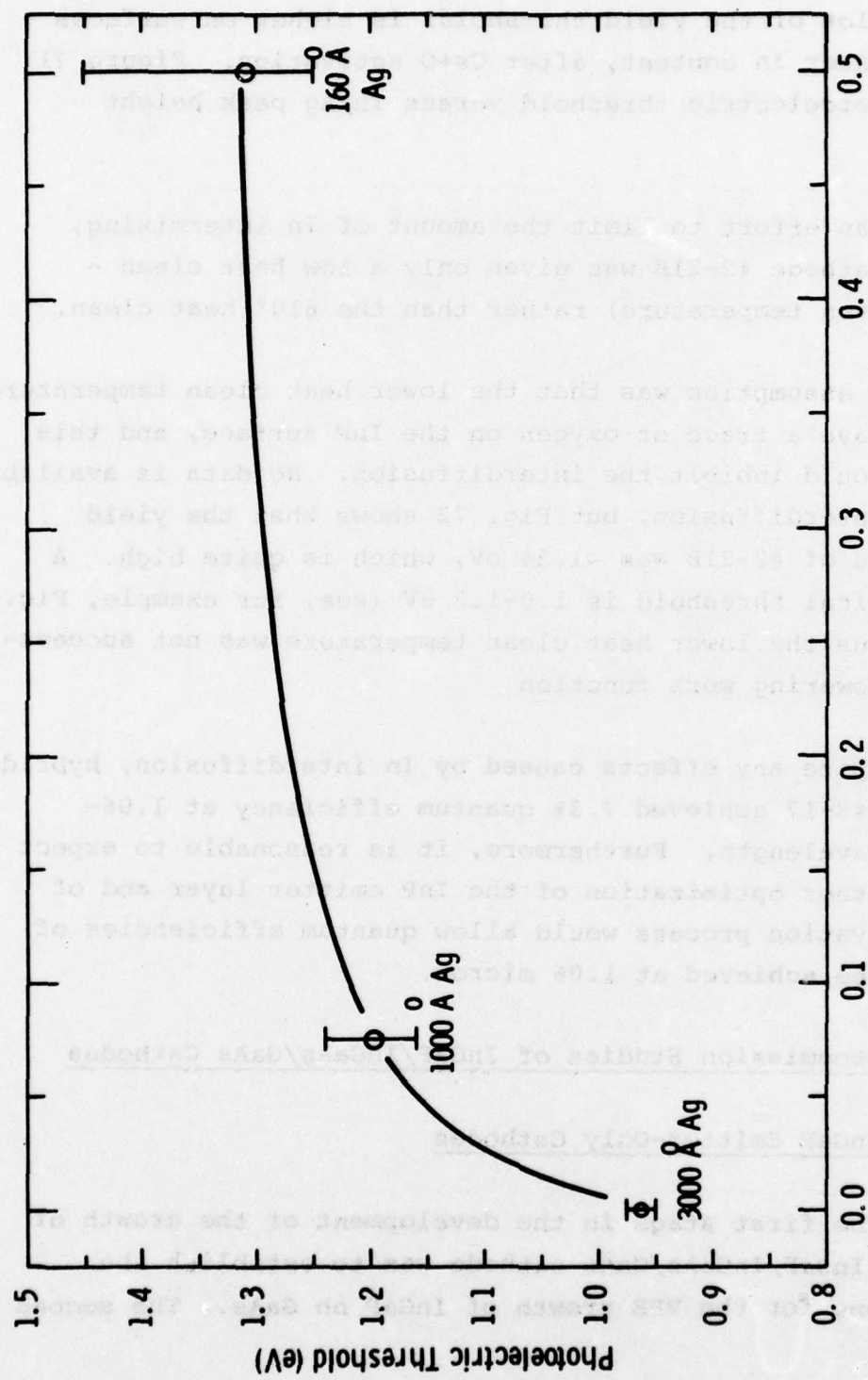


Fig. 71. In/Ag Auger peak height ratio vs photoelectric threshold for 3000, 1000, and 160 Å Ag films on InP.

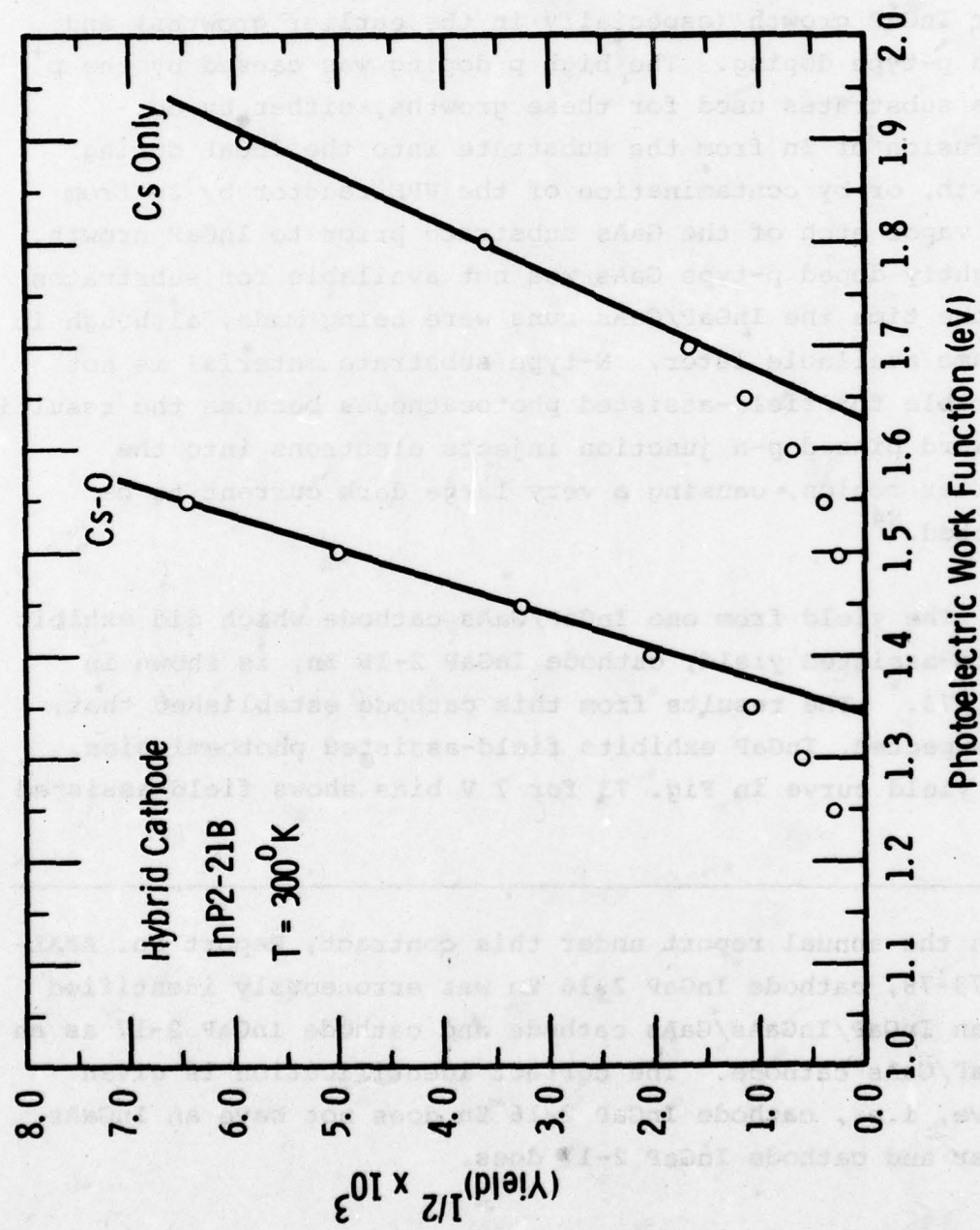


Fig. 72. Fowler photoemission plot for Cs-only and Cs+0 activations on a hybrid heterojunction cathode (Ag/InP surface).

stage was to grow the complete InGaP/InGaAs/GaAs structure. Several InGaP/GaAs structures were vacuum tested to establish that InGaP could be used as a field-assisted photoemitter.

Most of the InGaP/GaAs cathodes which were tested did not exhibit field-assisted photoemission. The lack of field-assisted photoemission was caused by a combination of poor InGaP growth (especially in the earlier growths) and high p-type doping. The high p doping was caused by the p⁺ GaAs substrates used for these growths, either by out-diffusion of Zn from the substrate into the InGaP during growth, or by contamination of the VPE reactor by Zn from the vapor etch of the GaAs substrate prior to InGaP growth. Lightly doped p-type GaAs was not available for substrates at the time the InGaP/GaAs runs were being made, although it became available later. N-type substrate material is not suitable for field-assisted photocathodes because the resulting forward biased p-n junction injects electrons into the emitter region, causing a very large dark current to be emitted.⁸⁴

The yield from one InGaP/GaAs cathode which did exhibit field-assisted yield, cathode InGaP 2-16 Zn, is shown in Fig. 73.* The results from this cathode established that, as expected, InGaP exhibits field-assisted photoemission. The yield curve in Fig. 73 for 7 V bias shows field assisted

* In the annual report under this contract, Report No. AFAL-TR-78-78, cathode InGaP 2-16 Zn was erroneously identified as an InGaP/InGaAs/GaAs cathode and cathode InGaP 2-17 as an InGaP/GaAs cathode. The correct identification is given above, i.e., cathode InGaP 2-16 Zn does not have an InGaAs layer and cathode InGaP 2-17 does.

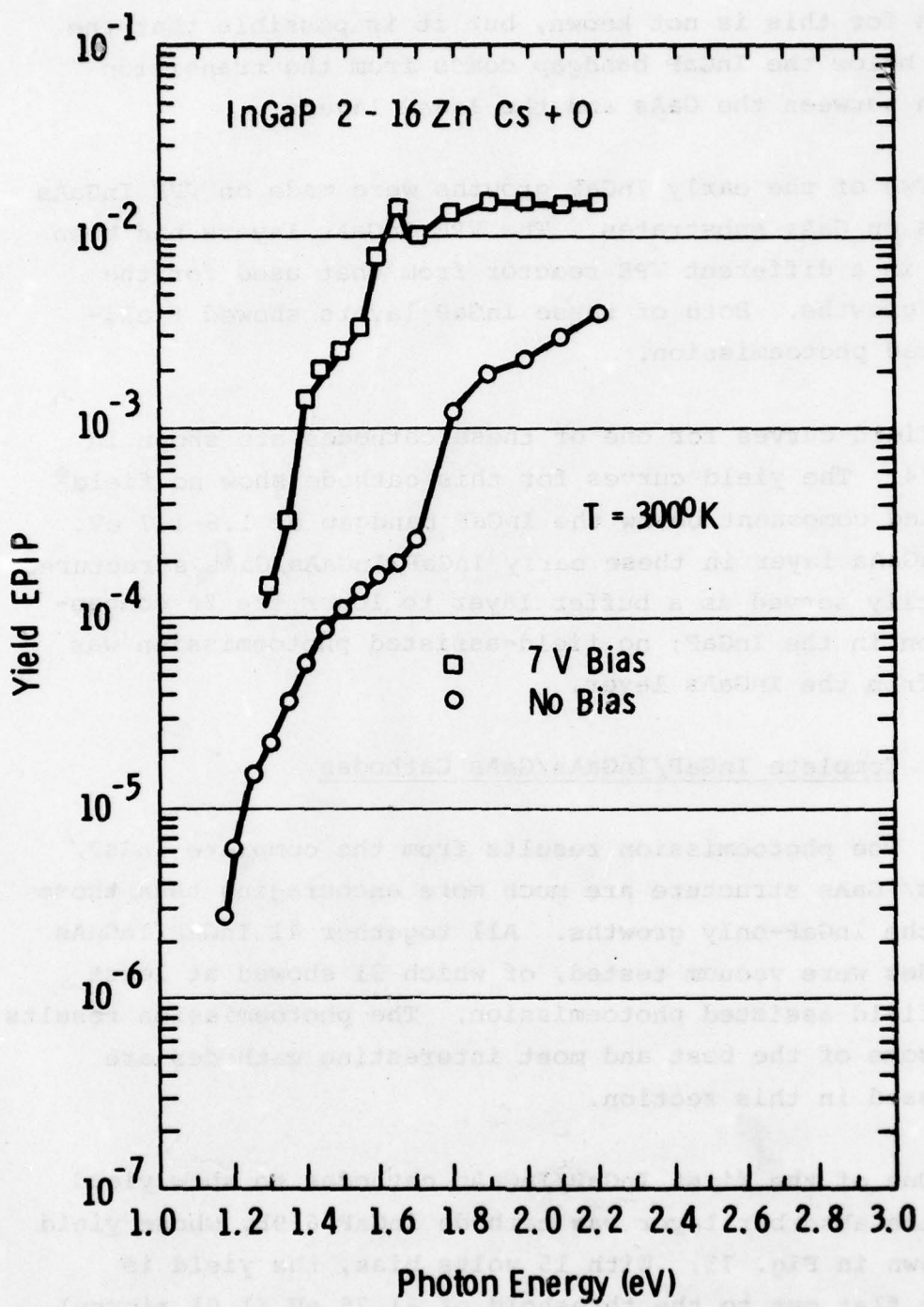


Fig. 73. Reflection-mode quantum yield from a p-InGaP/GaAs cathode for CS+O activation.

yield below the InGaP bandgap, extending to ~1.4 eV. The reason for this is not known, but it is possible that the yield below the InGaP bandgap comes from the transition region between the GaAs and the InGaP layers.

Two of the early InGaP growths were made on VPE InGaAs layers on GaAs substrates. The VPE InGaAs layers had been grown in a different VPE reactor from that used for the InGaP growths. Both of these InGaP layers showed field-assisted photoemission.

Yield curves for one of these cathodes are shown in Fig. 74. The yield curves for this cathode show no field-assisted component below the InGaP bandgap of 1.6-1.7 eV. The InGaAs layer in these early InGaP/InGaAs/GaAs structures primarily served as a buffer layer to lower the Zn concentration in the InGaP; no field-assisted photoemission was seen from the InGaAs layer.

3.7.2 Complete InGaP/InGaAs/GaAs Cathodes

The photoemission results from the complete InGaP/InGaAs/GaAs structure are much more encouraging than those from the InGaP-only growths. All together 41 InGaP/InGaAs cathodes were vacuum tested, of which 31 showed at least some field-assisted photoemission. The photoemission results from some of the best and most interesting cathodes are discussed in this section.

One of the first InGaP/InGaAs cathodes to show yield from the absorber layer was cathode InGaP 6-9B, whose yield is shown in Fig. 75. With 15 volts bias, the yield is nearly flat out to the threshold of ~1.25 eV (1.01 micron). The InGaAs absorber bandgap was too high to give yield out to 1.06 micron for this cathode. The peak yield at $h\nu = 1.4$

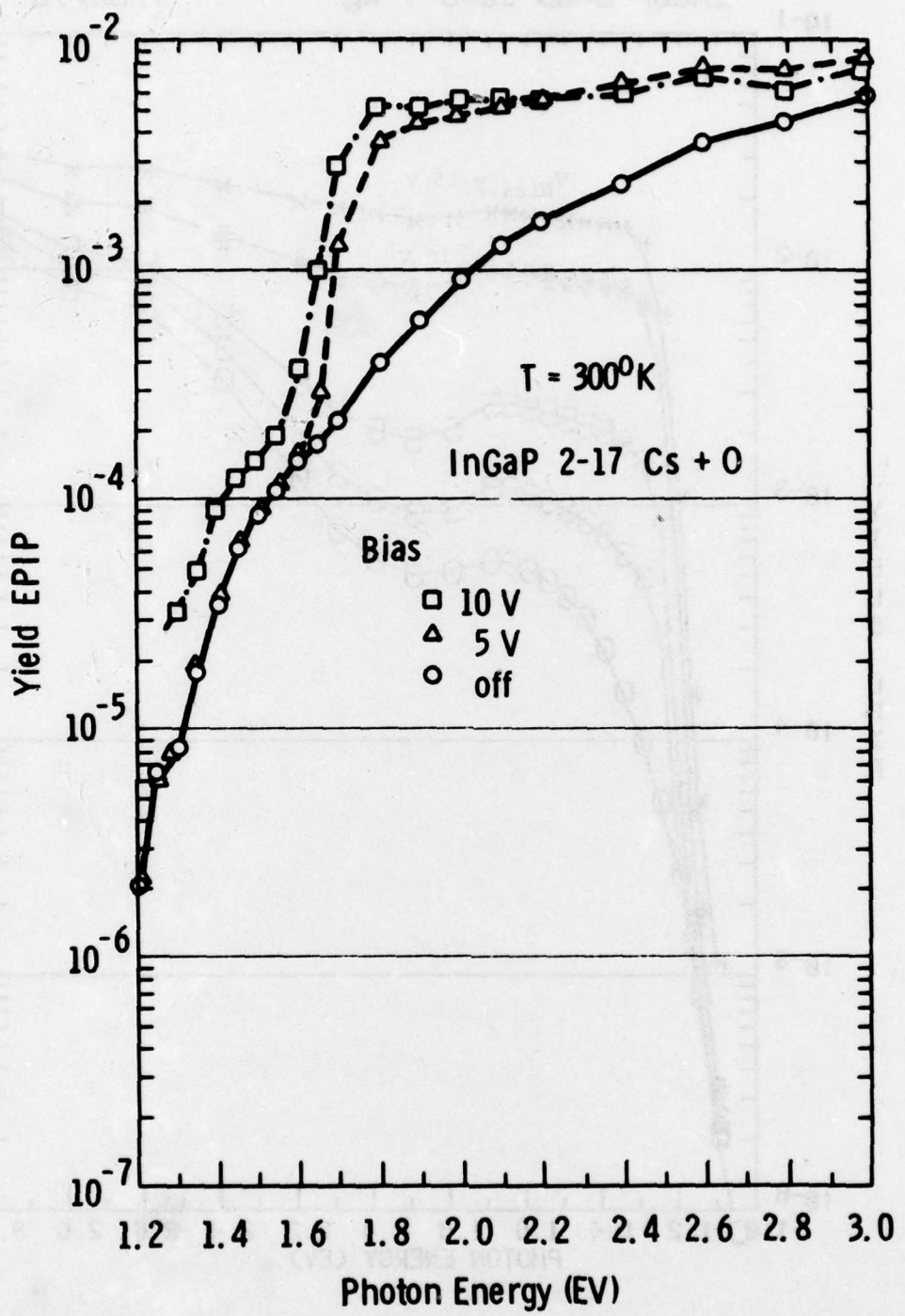


Fig. 74. Reflection-mode quantum yield from a p-InGaP/InGaAs/GaAs direct emitter cathode for Cs+O activation.

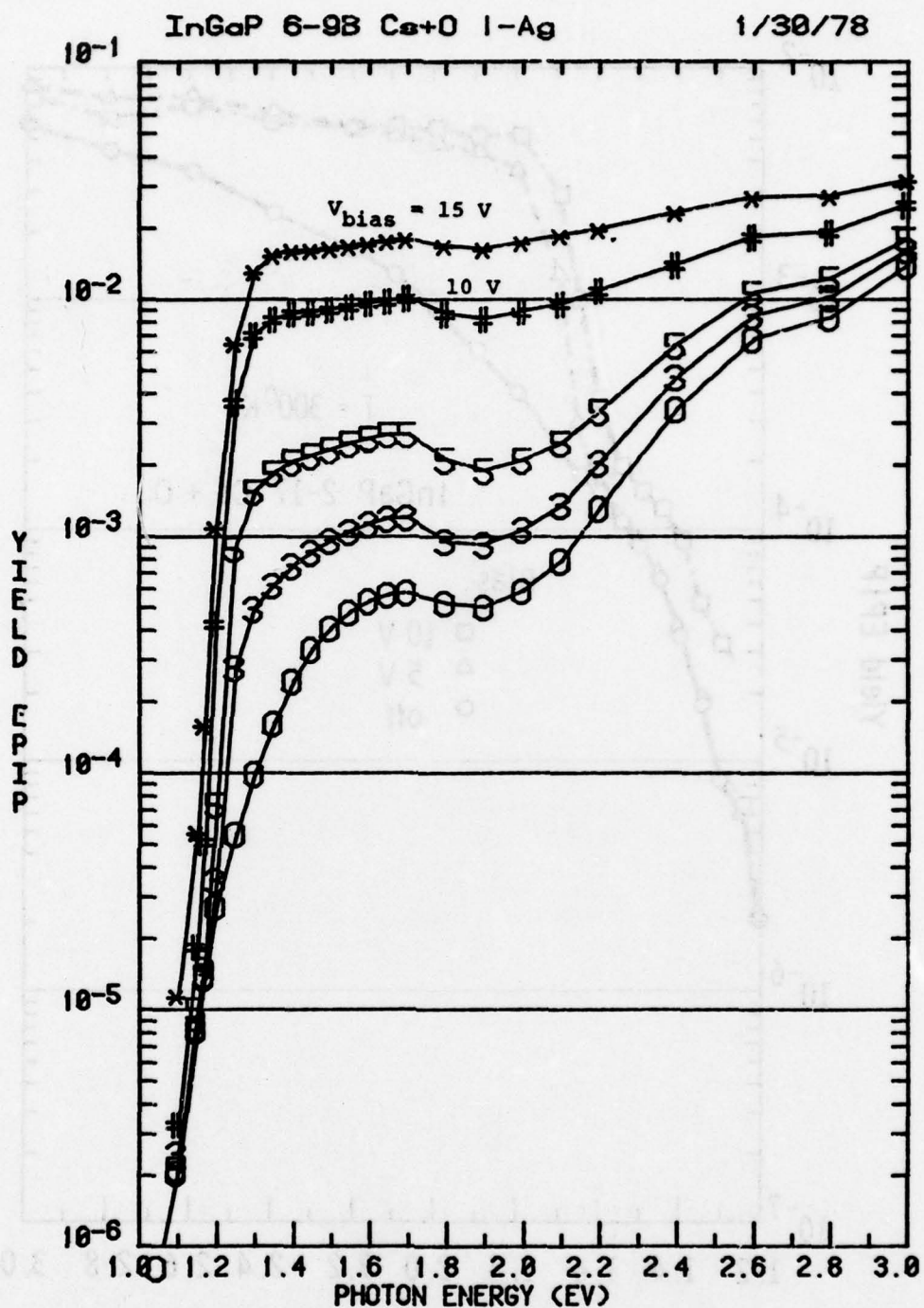


Figure 75. Reflection mode yield for InGaP/InGaAs/GaAs cathode #6-9B, Cs+O activation.

eV was 1.6%. The yield curves do not show a clear break at the InGaP bandgap, but both Auger electron spectra and photoluminescence verified that InGaP was present on the surface. The fact that a 15-volt bias was needed to maximize the yield indicates that the InGaP doping was lower than optimum since lower doping gives lower fields in the InGaP.

The yield from cathode SR 3-13, which did show field-assisted yield at 1.06 micron, is shown in Fig. 76. With 5 volts bias the yield is 0.7% at 1.06 micron. The step in the curves for bias \geq 2 volts at $h\nu = 1.7$ eV is the break between the yield from the InGaP and that from the InGaAs. For 1.1 eV $< h\nu < 1.7$ eV, the electrons are generated in the InGaAs and transferred across the heterojunction to the InGaP before being emitted. The yield just below $h\nu = 1.7$ eV relative to that just above $h\nu = 1.7$ eV is a measure of the transfer efficiency across the heterojunction. Figure 76 shows that with 5 volts bias the transfer across the heterojunction is less than 100%.

Figure 77, which shows the yield at 1.8 eV and 0.17 eV versus applied bias, also shows that the heterojunction transfer efficiency is less than 100% for biases up to 7 volts. Cleaving cathode SR 3-13 showed that the InGaP layer thickness was $1.5 \pm 0.2 \mu\text{m}$, and C-V measurements showed the InGaP doping to be $\sim 2 \times 10^{15} \text{ cm}^{-3}$. A calculation of the voltage required to give a depletion region of $1.5 \pm 0.2 \mu\text{m}$ for $2 \times 10^{15} \text{ cm}^{-3}$ doped InGaP gives 1.8-3.6 volts. Figure 77 shows that the yield from the InGaAs for SR 3-13 rises sharply for biases between 1 and 3 volts, in agreement with the depletion width calculation. The fact that the heterojunction transfer efficiency never reaches 100% indicates that the InGaP layer is too thick for the doping level to allow enough field at the InGaP/InGaAs interface to flatten out the conduction band step, as discussed above in Sec.

3.4.1.

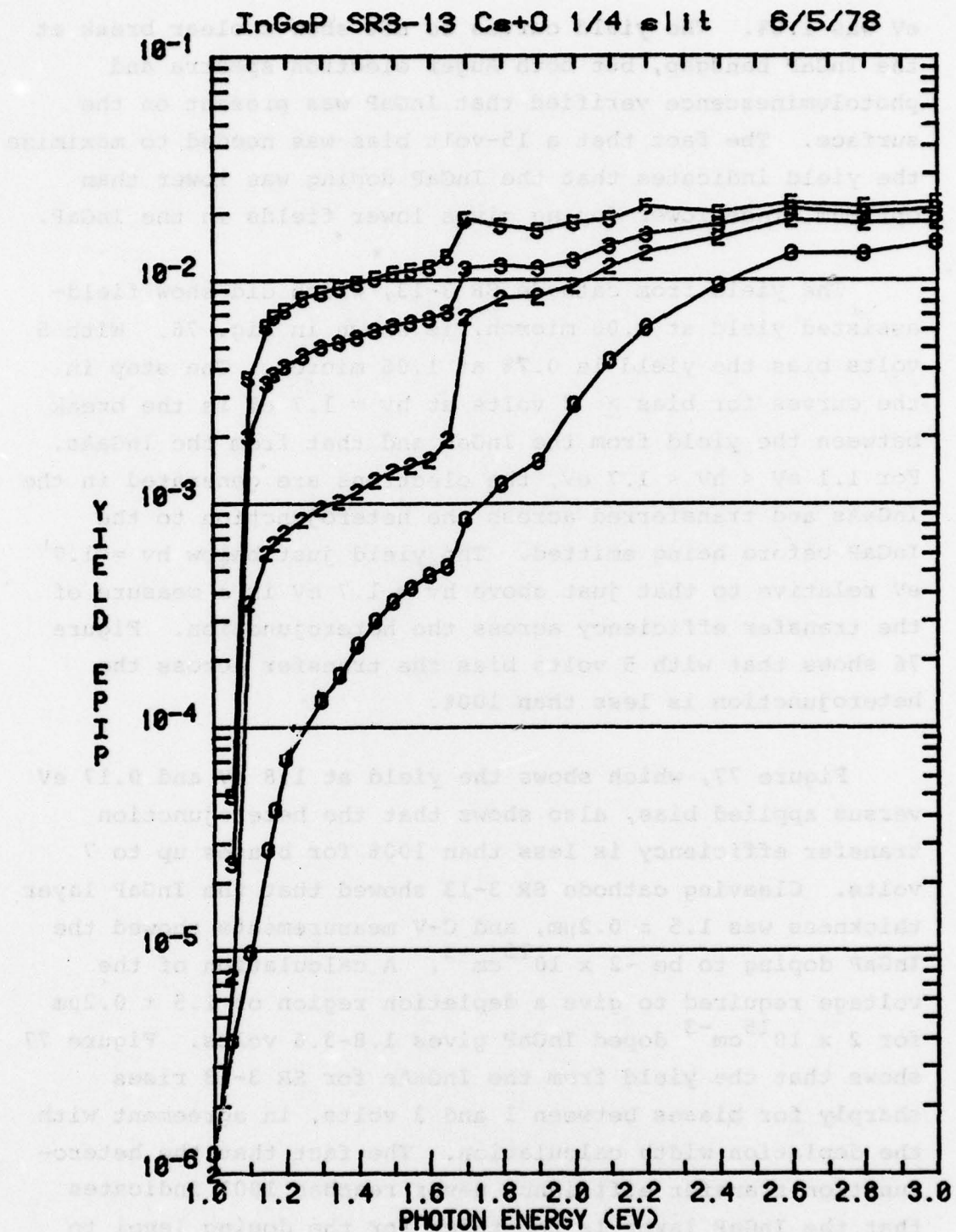


Figure 76. Reflection mode yield for InGaP/InGaAs/GaAs cathode #SR 3-13, Cs+O activation.

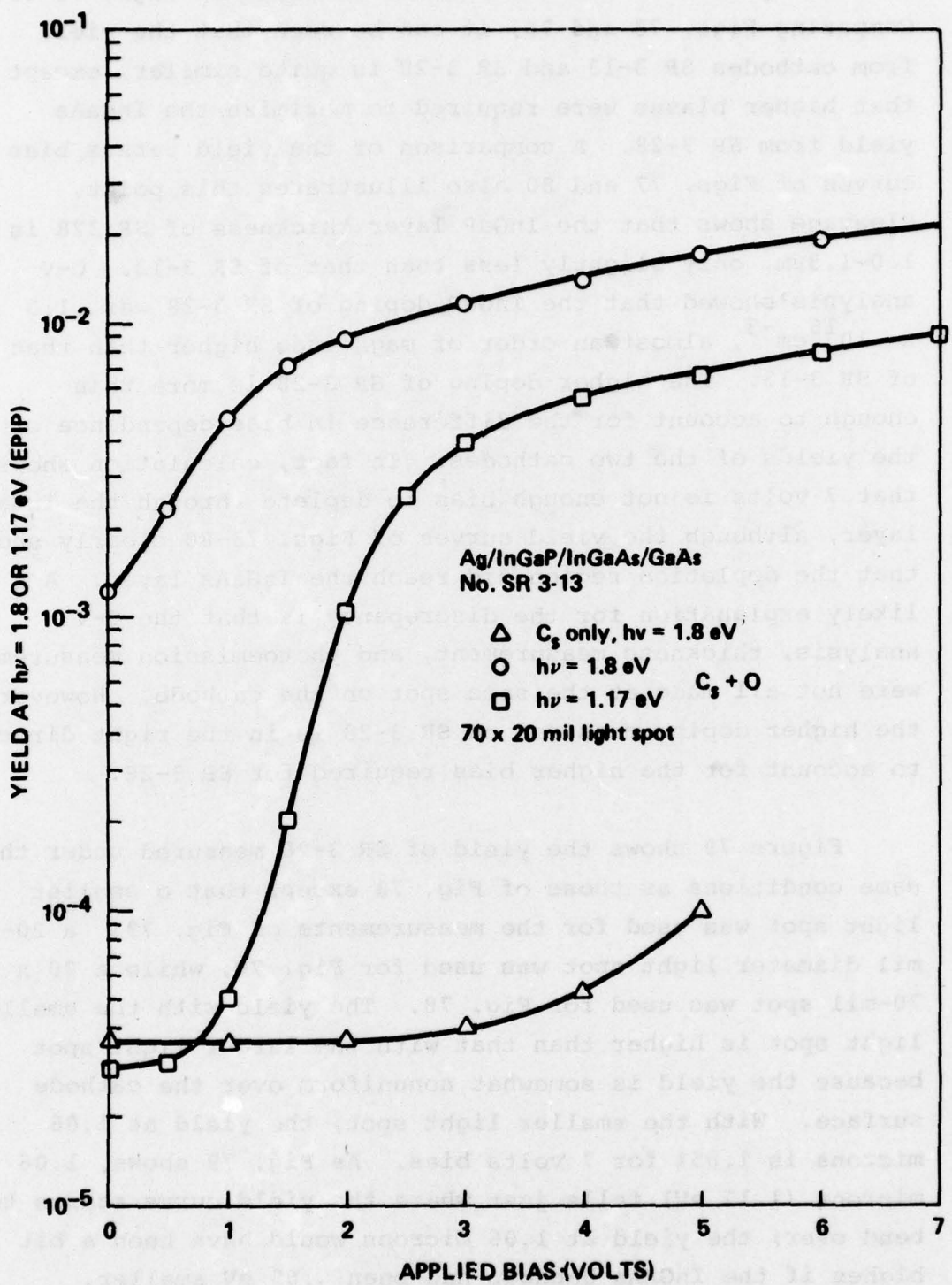


Fig. 77. Reflection-mode yield at $h\nu = 1.8$ and 1.17 eV as a function of bias for InGaP/InGaAs/GaAs cathode #SR3-13.

The yield for cathode SR 3-28 is shown in Figs. 78-80. Comparing Figs. 78 and 76, it can be seen that the yield from cathodes SR 3-13 and SR 3-28 is quite similar, except that higher biases were required to maximize the InGaAs yield from SR 3-28. A comparison of the yield versus bias curves of Figs. 77 and 80 also illustrates this point. Cleavage shows that the InGaP layer thickness of SR 328 is $1.0-1.3\mu\text{m}$, only slightly less than that of SR 3-13. C-V analysis showed that the InGaP doping of SR 3-28 was $\sim 1.5 \times 10^{16} \text{ cm}^{-3}$, almost an order of magnitude higher than that of SR 3-13. The higher doping of SR 3-28 is more than enough to account for the difference in bias dependence of the yields of the two cathodes. In fact, calculation shows that 7 volts is not enough bias to deplete through the InGaP layer, although the yield curves of Figs. 78-80 clearly show that the depletion region did reach the InGaAs layer. A likely explanation for the discrepancy is that the C-V analysis, thickness measurement, and photoemission measurements were not all made at the same spot on the cathode. However, the higher doping measured on SR 3-28 is in the right direction to account for the higher bias required for SR 3-28.

Figure 79 shows the yield of SR 3-28 measured under the same conditions as those of Fig. 78 except that a smaller light spot was used for the measurements of Fig. 79: a 20-mil diameter light spot was used for Fig. 79, while a 20 x 70-mil spot was used for Fig. 78. The yield with the smaller light spot is higher than that with the larger light spot because the yield is somewhat nonuniform over the cathode surface. With the smaller light spot, the yield at 1.06 microns is 1.05% for 7 volts bias. As Fig. 79 shows, 1.06 microns (1.17 eV) falls just where the yield curve starts to bend over; the yield at 1.06 microns would have been a bit higher if the InGaAs bandgap had been $\sim .05$ eV smaller.

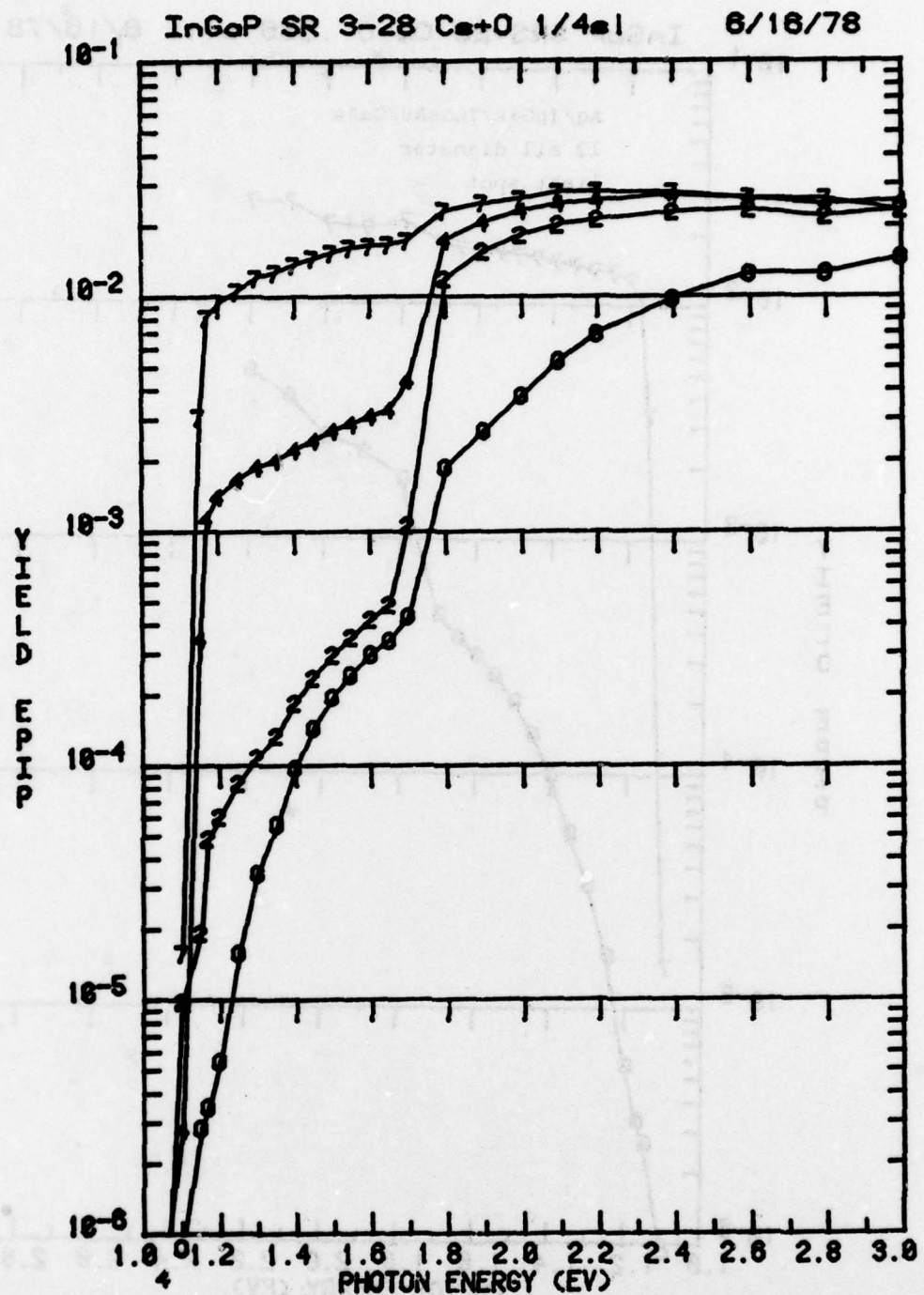


Figure 78. Reflection mode yield for InGaP/InGaAs/GaAs cathode #SR 3-28, measured with a 20 x 70 mil² light spot, Cs+O activation.

InGaP SR3-28 Cs+O .036 slit 6/16/78

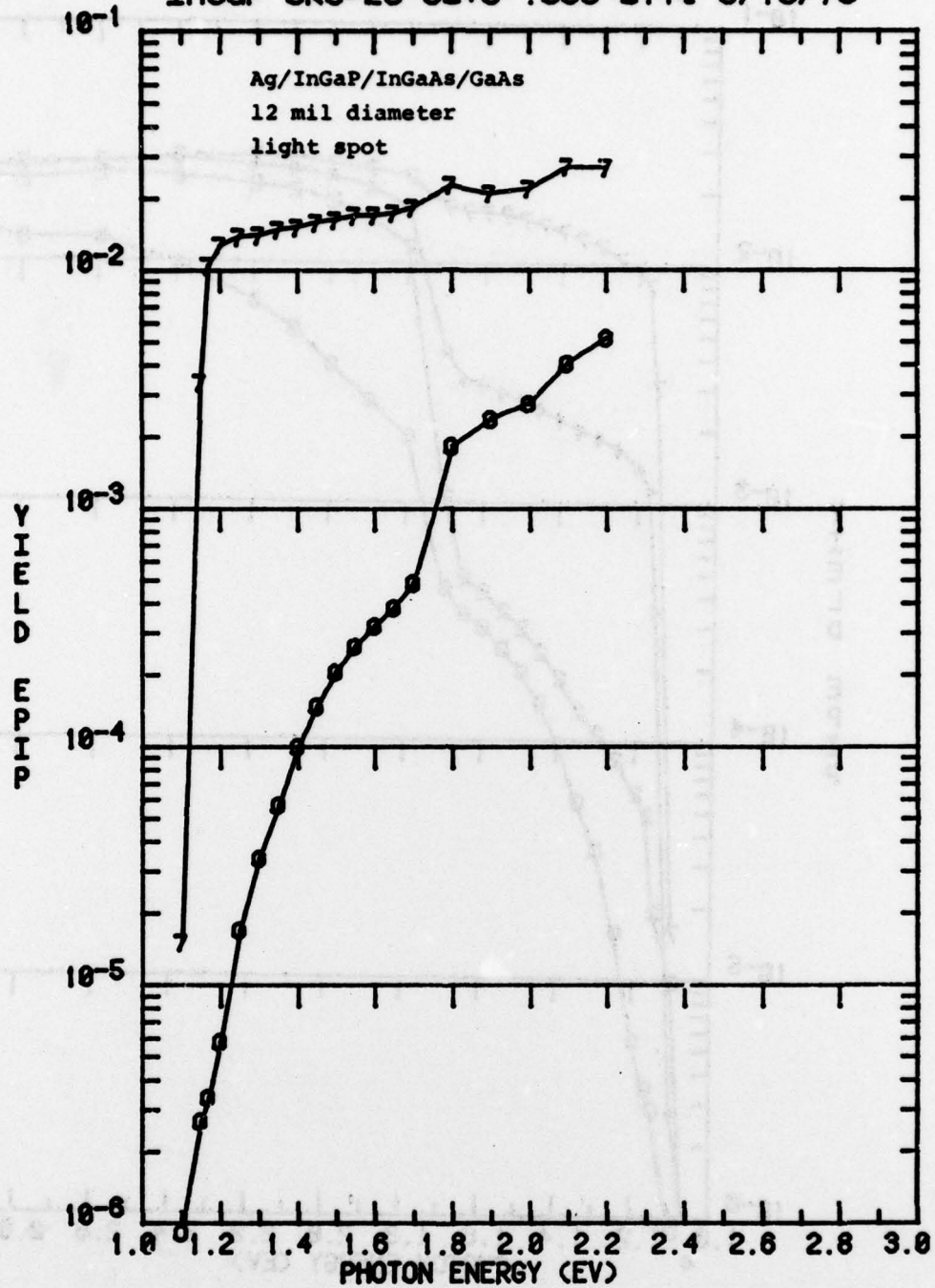


Figure 79. Reflection mode yield for InGaP/InGaAs/GaAs cathode #SR 3-28, measured with a 12 mil diameter light spot, Cs+O activation.

at 1.8 eV in mode at bias 0.2-0.8 volt.

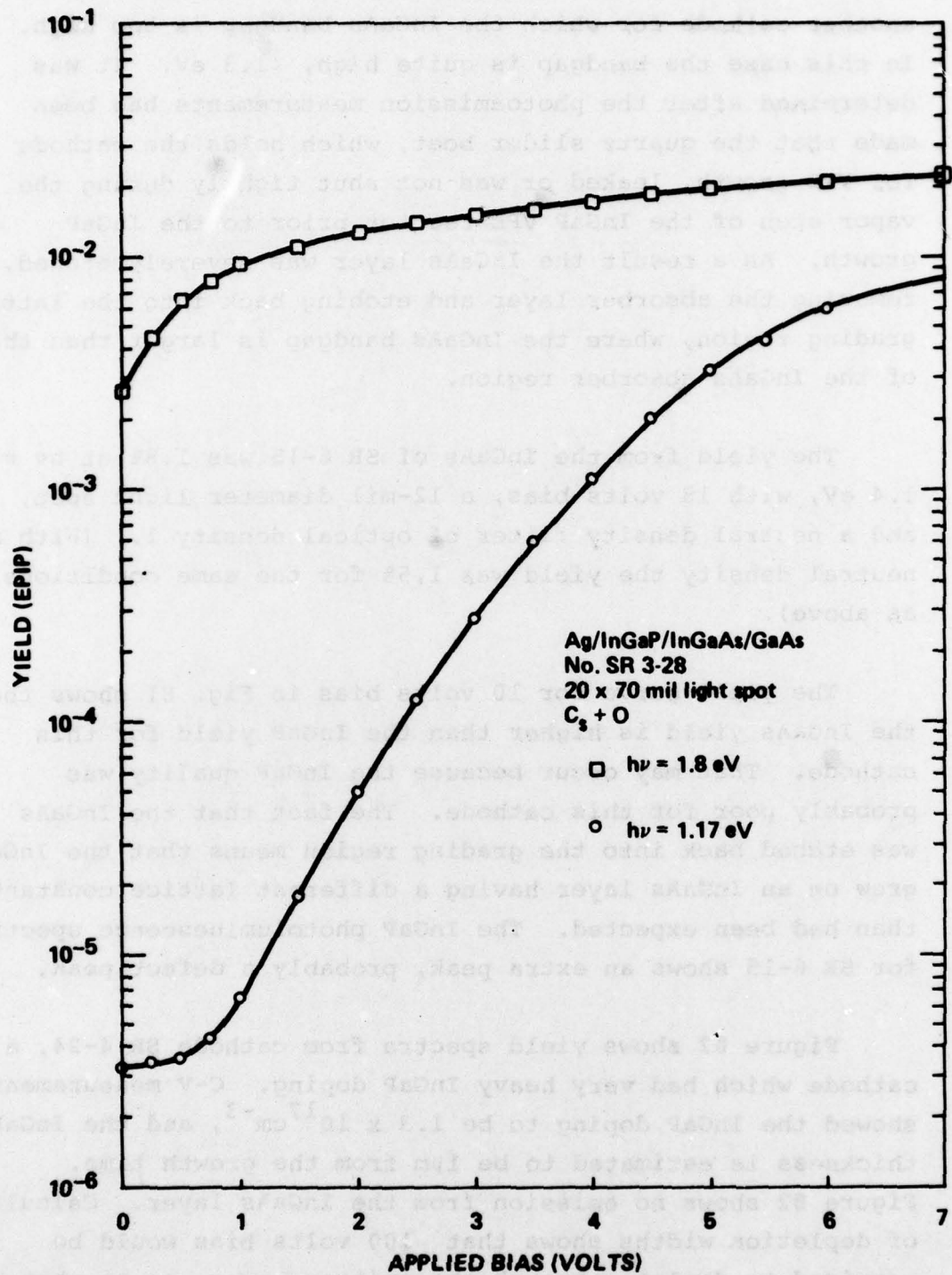


Fig. 80. Reflection-mode yield
at $h\nu = 1.8$ and 1.17 eV
as a function of bias for
InGaP/InGaAs/GaAs
cathode #SR3-28.

Cathode SR 6-15, whose yield is shown in Fig. 81, is another cathode for which the InGaAs bandgap is too high. In this case the bandgap is quite high, ~1.3 eV. It was determined after the photoemission measurements had been made that the quartz slider boat, which holds the cathode for VPE growth, leaked or was not shut tightly during the vapor etch of the InGaP VPE reactor prior to the InGaP growth. As a result the InGaAs layer was severely etched, removing the absorber layer and etching back into the lattice grading region, where the InGaAs bandgap is larger than that of the InGaAs absorber region.

The yield from the InGaAs of SR 6-15 was 1.8% at $h\nu = 1.4$ eV, with 18 volts bias, a 12-mil diameter light spot, and a neutral density filter of optical density 1. (With no neutral density the yield was 1.5% for the same conditions as above).

The yield curve for 10 volts bias in Fig. 81 shows that the InGaAs yield is higher than the InGaP yield for this cathode. That may occur because the InGaP quality was probably poor for this cathode. The fact that the InGaAs was etched back into the grading region means that the InGaP grew on an InGaAs layer having a different lattice constant than had been expected. The InGaP photoluminescence spectrum for SR 6-15 shows an extra peak, probably a defect peak.

Figure 82 shows yield spectra from cathode SR 4-24, a cathode which had very heavy InGaP doping. C-V measurements showed the InGaP doping to be $1.3 \times 10^{17} \text{ cm}^{-3}$, and the InGaP thickness is estimated to be 1 μm from the growth time. Figure 82 shows no emission from the InGaAs layer. Calculation of depletion widths shows that ~100 volts bias would be required to deplete through the emitter layer, so no photo-emission would be expected from the InGaAs layer.

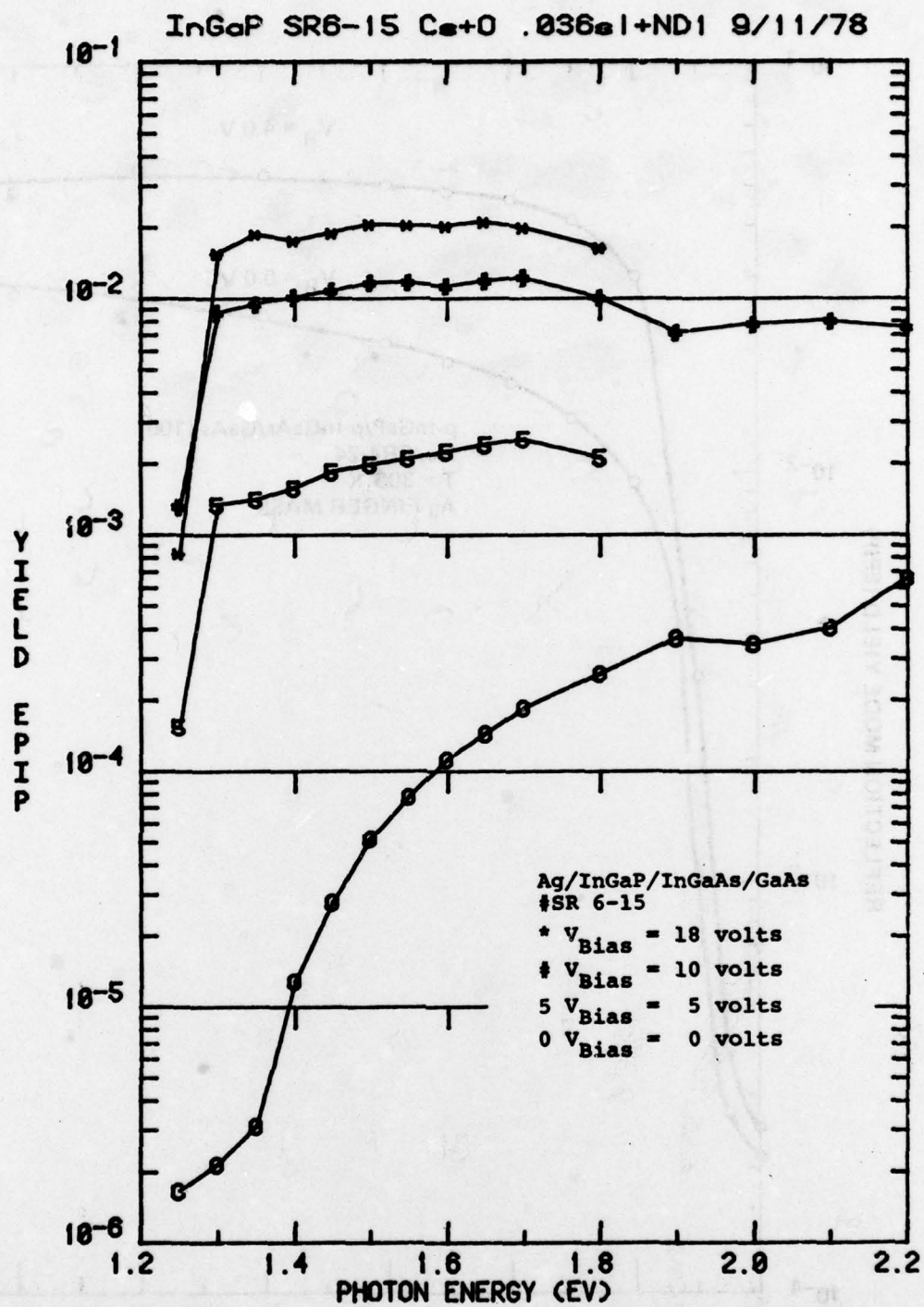


Figure 81. Reflection mode yield for InGaP/InGaAs/GaAs cathode #SR6-15, measured with a 12 mil dia light spot and an optical density 1 neutral density filter, Cs+O activation.

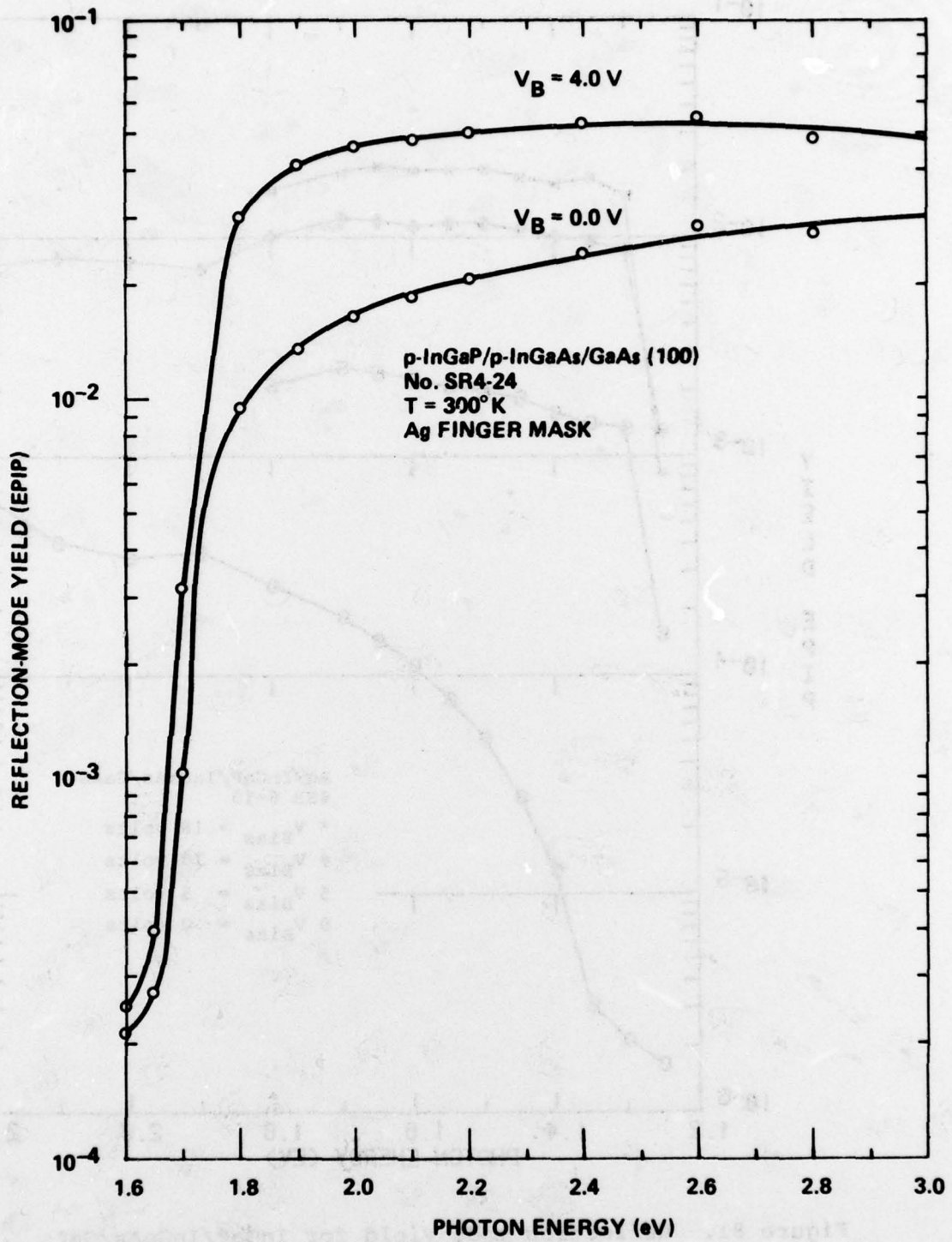


Fig. 82. Reflection-mode yield for
 InGaP/InGaAs/GaAs
 cathode #SR4-24, Cs+0
 activation.

The yield from the InGaP of SR 4-24 is quite high, ~5% at 4 volts bias. But it is already 2-3% at zero bias. The high zero bias yield is a feature common to both the InP and InGaP cathodes doped $>10^{17} \text{ cm}^{-3}$ that we have tested. For doping this high, the InGaP or InP approaches an NEA condition, giving rise to the high zero bias yield.

The InGaP/InGaAs/GaAs cathode results are encouraging in that ~1% quantum efficiency at 1.06 microns was obtained with InGaP layers that were not optimized for thickness and doping. Optimization of the InGaP layer should improve the quantum efficiency, though it is not clear at this point whether improvement of the InGaP would bring the 1.06-micron quantum efficiency up to the desired 20%.

Unfortunately, it was not possible to achieve sufficient reproducability in the InGaP growth to permit a systematic optimization of the InGaP emitter layer. VPE InGaP growth is quite difficult, and more time than was available under this contract would be required to develop the VPE InGaP growth to the point where doping and thickness could be precisely controlled.

4.0 Conclusions and Recommendations

Three different types of field-assisted 1.06-micron photocathodes were investigated under this contract. With a relatively small materials effort, the InGaAsP direct-emitter cathode demonstrated 2.7% reflection-mode yield at 1.06 micron, and the InP/InGaAs hybrid cathode demonstrated 7.3% yield, in an experimental ultrahigh vacuum system.

It is reasonable to expect that ~10% yield at 1.06 micron could be achieved from the InP/InGaAs hybrid cathode.

Additional work in optimizing the InP emitter layer doping and thickness would probably result in some improvement in the yield. The effect of Zn out diffusion from the InGaAsP absorber layer into the InP emitter is undoubtedly important, but little work has been done in this area. Additional work on the vacuum processing of the cathode is also needed. Included in this area are heat cleaning, sputter cleaning, the use of different Schottky-barrier metals, and different activation techniques.

By far the bulk of the materials effort under this contract was on the vapor phase epitaxial growth of the InGaP/InGaAs/GaAs cathode. Good looking growths were achieved, and field-assisted photoemission was achieved from several InGaP/InGaAs/GaAs cathodes, with a yield of 1.05% achieved at 1.06 micron. The VPE growth of the InGaP layer has proven to be quite difficult, however, with a large variation in InGaP quality from run to run. This lack of control over the InGaP parameters made it impossible to systematically optimize the InGaP/InGaAs/GaAs cathode.

A great improvement over the yield thus far demonstrated from the InGaP/InGaAs/GaAs cathode could be reasonably expected if sufficient effort were directed towards improving the growth of the cathode, particularly of the InGaP layer. However, improvement of this cathode to the point that its yield at 1.06 micron exceeds that of the InP/InGaAs hybrid cathode would require a fairly substantial effort, perhaps involving new technologies for the growth of InGaP. For example, it would be useful to explore the possibility of InGaP growth by Molecular Beam Epitaxy (MBE) or by organometallic vapor phase epitaxy, to see if either of these techniques provides better control over the InGaP growth than that achieved with the chloride vapor phase epitaxial growth system used for this contract.

REFERENCES

1. See, for example, A. H. Sommer, Photoemissive Materials, John Wiley & Sons, Inc. New York, 1968.
2. R. E. Simon and W. E. Spicer, Phys. Rev. 119, 621 (1960).
3. R. E. Simon and W. E. Spicer, J. Appl. Phys. 31, 1505 (1960).
4. P. R. Thornton and D. C. Northrup, Solid State Electron. 8, 437 (1965).
5. I. G. Daview and P. R. Thornton, Appl. Phys. Lett. 10, 249 (1967).
6. S. A. Ward, T. E. Fischer, and W. B. Nowak, CBS Laboratories, Technical Report AFAL-TR-69-161, June 1969, on Contract AF33 (615)-3638.
7. R. L. Bell, Negative Electron Affinity Devices, Clarendon Press, Oxford, 1973.
8. J. S. Escher, RCA Laboratories, Final Report, December 1973, Contract DAAK02-72-C-0412.
9. F. G. Allen, J. Schwank, I. Shahriary, and K. Venkateswaran, University of California, Los Angeles, Final Report, June 1976, Contract DAAK02-72-C-0410.
10. H. G. White and R. A. Logan, J. Appl. Phys. 34, 1990 (1963).
11. T. Itoh, I. Matsuda, and K. Hasegawa, J. Appl. Phys. 38, 3395 (1967). See also, J. Appl. Phys. 41, 1945 (1970).
12. A. L. Musatov and L. N. Shulepov, Sov. Phys. Solid State 12, 2711 (1971).
13. I. J. D'Haenens, J. A. Roth, and C. L. Anderson, Hughes Research Laboratories, Final Technical Report on Contract DAAK02-72-C-0442. See also, Final Technical Report on Contract DAAK02-72-C-0147.
14. N. A. Foss, J. Appl. Phys. 42, 3762 (1971).
15. A. G. Milnes, D. I. Feucht, and P. K. Govil, Carnegie-Mellon Institute, Final Report, June 1974, on Contract DAAK02-72-C-0206. See also Appl. Phys. Lett. 19, 383 (1971).

REFERENCES (Cont.)

16. R. Sahai, J. S. Harris, R. C. Eden, L. O. Bubulac, and J. C. Chu, *Crit. Rev. Solid State Sci.* 5, 565 (1975). See also, contract reports under ARPA Contract DAAK02-73-C-0231.
17. D. K. Schroder, R. N. Thomas, J. Vine, and H. C. Nathanson, *IEEE Trans. Electron Devices*, ED-21, 785 (1974).
18. P. R. Thornton, Stanford Research Institute, Final Report, December 1973, Contract DAAK02-72-C-0149.
19. I. J. D'Haenens, J. A. Roth, and C. L. Anderson, Hughes Research Laboratories, Final Report on Contract DAAK02-72-C-0442 (1975). See also, Final Report on Contract DAAK02-72-C-0147.
20. See, for example, J. J. Uebbing and L. W. James, *J. Appl. Phys.* 41, 4505 (1970).
21. See, for example, C. R. Crowell and S. M Sze, in *Physics of Thin Films* (Academic Press, New York, 1967), Vol. 4, p. 325.
22. See, for example, R. L. Bell, L. W. James, G. A. Antypas, J. Edgecumbe, and R. L. Moon, *Appl. Phys. Lett.* 19, 513 (1971); also D. G. Fisher, R. E. Enstrom, J. S. Escher, and B. F. Williams, *J. Appl. Phys.* 43, 3815 (1972).
23. R. L. Bell, L. W. James, and R. L. Moon, *Appl. Phys. Letters*, 25, 645 (1974).
24. L. W. James, J. P. Van Dyke, F. Herman, and D. M. Chang, *Physical Review B*, 1, 3998 (1970).
25. R. H. Fowler, *Physical Review*, 38, 45 (1931).
26. R. L. Bell and J. J. Uebbing, *Appl. Phys. Letters*, 12, 76 (1968).
27. G. A. Antypas, R. L. Moon, L. W. James, L. J. Edgecumbe, and R. L. Bell, in Gallium Arsenide and Related Compounds, 1972, (Conf. Series #17, IPPS, London, 1973), p. 48.
28. R. Sankaran, G. A. Antypas, R. L. Moon, J. S. Escher, and L. W. James, *J. Vac. Sci. Technol.*, 13, 932 (1976).

REFERENCES (Cont.)

29. G. A. Antypas and L. Y. Shen, in Gallium Arsenide and Related Compounds, 1976, (Inst. Phys. Conf. Ser. #33b, London, 1977), p. 96.
30. J. S. Escher, R. D. Fairman, G. A. Antypas, R. Sankaran, L. W. James, and R. L. Bell, CRC Rev. Solid State Sci. 5, 577 (1975).
31. Work toward a passive night vision imaging device sensitive in the 1-2 micron range is under current investigation in this laboratory. This work is funded by ARPA and is monitored by NVL: Contract No. DAAK02-74-C-0132. The heterojunction cathode is the primary emphasis under this contract.
32. M. T. Pakhomov, A. YE. Melamid, and YA. B. Gerchikov, Radio Eng. and Electron Phys. 20, 147 (1975).
33. Varian LSE, 601 California Avenue, Palo Alto, CA 94304.
34. J. S. Escher, G. A. Antypas, and J. Edgecumbe, Appl. Phys. Letters 29, 153 (1976).
35. J. S. Escher and G. A. Antypas, Appl. Phys. Letters 30, 314 (1977).
36. R. E. Enstrom, D. Richman, M. S. Abrahams, J. R. Alpert, D. G. Fisher, A. H. Sommer, and F. F. Williams, Proceedings of the Third International Symposium on Gallium Arsenide and Related Compounds, IPPS, London (1970).
37. S. B. Hyder, J. Electrochem. Soc. 123, 1503 (1976).
38. J. O. McCaldin, T. C. McGill, and C. A. Mead, Phys. Rev. Lett. 36, 56 (1976).
39. C. A. Mead, Solid-State Electron. 9, 1023 (1966).
40. J. S. Escher, L. W. James, R. Sankaran, G. A. Antypas, R. L. Moon, and R. L. Bell, J. Vac. Sci Technol. 13, 874 (1976).
41. G. A. Antypas and J. Edgecumbe, J. Crystal Growth 34, 132 (1976).
42. Note that 1.21 eV at 77°K corresponds to 1.16 eV at 300°K which is nearly ideal for 1.06-micron detection.

REFERENCES (Cont.)

43. G. B. Stringfellow, P. F. Lindquist, and R. A. Burmeister, *J. Electronic Materials* 1, 437 (1972).
44. C. J. Nuese, D. Richman, and R. B. Clough, *Met Trans.* 2, 789 (1971).
45. H. Kressel, *J. of Electronic Materials*, 4, 1081 (1975).
46. C. J. Nuese, G. H. Olsen, M. Ettenberg, J. J. Gannon, and T. J. Zamerowski, *Appl. Phys. Lett.* 29, 807 (1976).
47. C. J. Nuese and G. H. Olsen, *Appl. Phys. Lett.* 26, 528 (1975).
48. V. S. Ban and M. J. Ettenberg, *J. Phys. Chem. Solids* 34, 1119 (1973).
49. A. G. Sigai, C. J. Nuese, R. E. Enstrom, and T. Zameroweski, *J. Electrochem. Soc.* 120, 947 (1973).
50. R. E. Enstrom, C. J. Nuese, V. S. Ban, and J. R. Appert, *Proc. 4th Symposium on GaAs, 1972*, (Institute of Physics, London) p. 37.
51. H. Kressel, C. J. Nuese, and I. Ladany, *J. Appl. Phys.* 44, 3266 (1973).
52. H. Seki and S. Minegawa, *Japanese J. Of Phys.* 11, 850 (1972).
53. L. A. Volkov, F. P. Kesamarly, V. F. Kovalenko, I. E. Maronchuk, and L. G. Shepel, *Sov. Phys. Semicond.* 11, 732 (1977).
54. V. S. Ban and M. Ettenberg in "Chemical Vapor Deposition, Fourth International Conference," G. F. Wakefield and J. M. Blocher, Jr., Editors, p. 31, The Electrochemical Society Softbound Symposium Series, Princeton, New Jersey (1973).
55. M. Ettenberg, G. H. Olsen, and C. J. Nuese, *Appl. Phys. Lett.* 29, 141 (1976).
56. G. H. Olsen, M. S. Abrahams, and T. J. Zamerowski, *J. Electrochem. Soc.* 121, 1650 (1974).
57. C. J. Nuese, A. G. Sigai, J. J. Gannon, and T. J. Zamerowski, *J. Electronic Mat.* 3, 51 (1974).

REFERENCES (Cont.)

58. O. N. Ermakov, R. S. Igratkina, V. P. Sushkov, and M. V. Chukichev, Sov. Phys. Semicond. 11, 651 (1977).
59. T. Kato, T. Matsumoto, and T. Ishida, Japan J. Appl. Phys., 15, 2265 (1976).
60. This Auger depth profile was measured for us by C. Y. Su of Stanford University.
61. R. L. Anderson, Solid State Electron. 5, 341 (1962).
62. A. G. Milnes and D. L. Feucht, Heterojunction and Metal-Semiconductor Junctions, (Academic Press, New York, 1972).
63. B. L. Sharma and R. K. Purohit, Semiconductor Heterojunctions, (Pergamon Press, New York, 1974).
64. See, for example, W. R. Frensley and H. Kroemer, J. Vac. Sci. Technol. 13, 810 (1976). W. A. Harrison, J. Vac. Sci. Technol. 14, 1016 (1977). W. R. Frensley, and H. K. Kroemer, Phys. Rev. B 16, 2642 (1977).
65. P. E. Gregory, J. S. Escher, S. B. Hyder, Y. M. Houng, and G. A. Antypas, J. Vac. Sci. Technol. 15, 1483 (1978).
66. W. G. Oldham and A. G. Milnes, Solid State Electron. 6, 121 (1963).
67. D. T. Cheung, S. W. Chiang, and G. L. Pearson, Solid State Electron. 18, 263 (1975).
68. R. Dingle, A. C. Gossard, and W. Wiegmann, Phys. Rev. Lett. 34, 1327 (1975).
69. E. A. Rozek, N. Holonyak, B. A. Vojak, G. E. Stillman, J. A. Rose, D. L. Keune, and J. D. Fairing, Appl. Phys. Lett. 31, 288 (1977).
70. S. M. Sze, Physics of Semiconductor Devices, (John Wiley & Sons, New York, 1969), p. 370.
71. The idea of a "double-transfer" heterojunction TE cathode was discussed in Sec. 3.3.1, Varian Technical Proposal No. 2274, August 1976.

REFERENCES (Cont.)

72. J. S. Escher, T. J. Maloney, P. E. Gregory, S. B. Hyder, and Y. M. Hwang, "Photoemission to 1.7 Microns from a InP/InGaAs Transferred-Electron Photocathode," paper presented at the 1978 Device Research Conference, UC Santa Barbara, June 1978. Also an informal talk given by T. J. Maloney entitled "Electron Transport in Field-Assisted Photoemitters," presented at the Workshop on Hot-Electron Phenomena in Semiconductors, Cornell University, Ithaca, N.Y., August 1978.
73. Semi-Annual Technical Report No. 7 under Contract DAAK02-74-C-0132 and Final Report under Contract DAAG-76-C-0002.
74. T. J. Maloney and J. Frey, *J. Appl. Phys.* 48, 781 (1977) and references therein.
75. R. W. Hockney et al, *Electron. Lett.* 10, 484 (1974).
76. W. E. Spicer, *Appl. Phys.* 12, 115 (1977).
77. A. H. Sommer, *RCA Review* 34, 95 (1973).
78. J. S. Escher and R. Sankaran, *Appl. Phys. Lett.* 29, 87 (1976). Also see Appendix B, Varian Technical Proposal No. 2274, August 1976.
79. An incident photon irradiance of $\sim 1 \times 10^{-4} \text{ W/cm}^2$ generates only $\sim 10^{-10}$ excess carriers/cm³. See Ref. 30.
80. Figures 69 and 71 are taken from Semi-Annual Tech. Report No. 5, April 1977, and Figure 70 from Quarterly Tech. Report 7, July 1977, under Contract DAAK02-74-C-0132. See Ref. 31.
81. A. Hiraki, K. Shuto, S. Kim, W. Kammura, and M. Iwami, *Appl. Phys. Lett.* 31, 611 (1977).
82. P. W. Chye, I. Lindau, P. Pianetta, C. M. Garner, and W. E. Spicer, *Phys. Rev. B* 17, 2682 (1978).
83. P. W. Chye, I. Lindau, P. Pianetta, C. M. Garner, and C. Y. Su, and W. E. Spicer, *Phys. Rev. B* (to be published).
84. Quarterly Technical Report No. 1 under Contract DAAK02-74-C-0132, p. 20-24.